Neural mechanisms underlying mechanosensation through rodent olfactory system

A thesis

submitted in partial fulfillment of the requirements

for the degree of

Doctor of Philosophy

by

Sarang Mahajan

20163440

INDIAN INSTITUTE OF SCIENCE, EDUCATION AND RESEARCH, PUNE

2022

Dedicated to

“Papa, Mummy, and Shubhi”

Declaration

I declare that this written submission represents my ideas in my own words. Wherever contributions of others are involved, effort has been made to indicate it clearly, with due reference to the literature and original sources. I also declare that I have followed principles of academic honesty and integrity and have not misinterpreted, fabricated, or falsified any thought, data, fact or source in my submission. I understand that the failure to comply with the above will result in disciplinary action by the Institute, and can also evoke penal action from the sources that have not been properly cited or from whom proper permission has not been taken when needed.

Date: 02-11-2022

Sarang Mahajan

20163440

Certificate

This is to certify that the work incorporated in the thesis entitled '**Neural Mechanisms underlying mechanosensation through rodent olfactory system'**, submitted by **Sarang Mahajan** was carried out by the candidate, under my supervision. This work presented here or any part of it has not been included in any other thesis submitted previously for the award of any degree or diploma from any other University or Institute.

Date: 02-11-2022

Dr. Nixon M. Abraham

Acknowledgements

I would like to express my gratitude towards Dr. Nixon M. Abraham, an outstanding mentor and supervisor, for providing me with a dynamic lab environment, invaluable insights, and the opportunity to grow during the course of my PhD at IISER Pune. I am thankful to be mentored by someone who taught me to set high goals, work hard and consistently to meet them, develop ideas, try them out, embrace failures, take a step back to think again, and keep on trying until I succeed. He provided me with a lot of encouragement and inspired me to strive for perfection, which helped me develop both personally and professionally. I am also grateful to Nixon for providing me an opportunity to assist me in the setup of the lab. It was an exciting experience to be one of the lab's inaugural students and witness it evolve.

I am also indebted to Dr. Raghav Rajan and Dr. Suhita Nadkarni, members of my research advisory committee for their valuable feedbacks and opinions during my annual presentations. They were promptly available, and they always engaged in extensive discussions, even if I approached them in a parking lot. I extend my gratitude to Prof. N.K. Subedhar, Dr. Aurnab Ghose, Dr. Collins Assisi, and Dr. Balaji Jayaprakash for their guidance, inputs and fruitful suggestions. My appreciation also goes out to Dr. Sunish Kumar Radhakrishnan, who supervised me during my master's. One of the things that made me eager to enrol in graduate school was his approach and love toward science.

Additionally, the warm and encouraging LNCB members offered a stimulating environment appropriate for progress. I feel privileged to be friends with these people. Every single person in the lab has consistently gone above and beyond to help me whenever I've had an issue with my work. The following people deserve my gratitude for making the lab an enjoyable place to work: Anindya, Meenakshi, Shruti, Priya, Susobhan, Sanyukta, Karishma, Rajdeep, Ananthi, Suhel, Kaushik, Felix, Arpan, Meher, Atharva, Avi, Deepshikha, Rishabh, and Siddharth. I considered Anindya, Sasank, and Meenakshi to be my closest friends, and I always believed us to be the Fantastic Four! I dearly miss Sasank who was one of the intelligent persons I ever met. I spent a lot of time working with Anindya, and I gained a great deal of insight from him. Meenakshi and I are like Tom and Jerry, who often bicker but stand by one another when needed. I'd like to thank them both for making my experience here so enriching. I am grateful to Shruti, Priya, Susobhan, and Sanyukta who have been great friends apart from being extremely helpful labmates. I would also like to thank Niyoti for her support and assistance. I had the honour of serving as a mentor for Suhel, Felix, Deepshikha, Siddarth,

Rishabh, and Ganesh during their master's theses. All of them have been really motivated and quick learners, and I wish them luck in their future pursuits.

I had a great time with my PhD batchmates. Special thanks to Bhavin, Rohan, Alakananda, Vibhishan, Abhinaya, and Manish with whom I did not just attend classes, but also, had never ending discussions on science and life, went on trips, supported each other during tough times, and had impromptu dinners. I also want to express my gratitude to my other friends, who have always stood with me when things became tough. Special thanks to Deepak, Niyor, Nitesh, Rajat, Rachit, Amit, Devansh, Anu (Arun Sharma), and Saurabh Bhaia. I share a special bond with Deepak, Nitesh and Rajat who have been part of my everyday life for a long time.

I thank IISER Pune for providing me with an opportunity to do my PhD here and CSIR for funding during my tenure. I also thank the Biology Department at IISER Pune for all the facilities and support. I want to convey my sincere gratitude to the biology office colleagues Piyush, Kalpesh, Sandeep, Mahesh, Mrinalini, and Rupali who were always available to help me throughout my PhD journey. I would like to thank the animal house facility (NFGFHD), IISER Pune, without whom this thesis would not have been possible. Thank you Dr. Suraj and Dr. Krishnaveni for maintaining this wonderful facility. A special thanks to Vinay, and the other present and colleagues of the animal house for making sure I got quick access to my test animals. I cannot thank Chavan Kaka enough for his relentless efforts to keep the lab tidy and create a productive working atmosphere. I also appreciate Nilesh Dumbre's assistance with all the electronics-related tasks.

I'm also delighted to have a battalion of loving and encouraging cousins and relatives who gave me advice, motivated me, and enabled me to arrive here. I want to express my heartfelt gratitude to Eshesh, Hitesh, Gaurav, and Tanuj Bhaia for never losing faith in me and always being there. My uncles, P.R. Mahajan, and Tilak Raj Gupta, deserve my gratitude for being father figures to me and helping me through my setbacks. My research career would not have been possible without the support of my late uncle Ramesh Mahajan, who always inspired me to study and try new things and who I dearly miss. I couldn't avert the inevitable, but I know that his memories and teachings will stay with me.

Above all, without my family — my papa (Ved Prakash Mahajan), mummy (Meera Mahajan), my younger brother Shubham, and Himani — none of this would have been possible. My parents have always supported me in all of my life's decisions and acted as a

foundation of strength for me. Even though I lack the words to adequately describe my brother's contributions, I can certainly say that even though he was my younger sibling, he played the role of an elder one in my life. He was always there and did everything possible to help me whenever I was lost. Thanks a lot for everything, bhai 😊. I can't express how grateful I am to Himani for being my better half, who never lost faith in me and stuck by my side despite my struggles. I can't help but appreciate the effort she makes to make me smile when rough circumstances arise. I am fortunate to have her as a companion in this thrilling life adventure. This dissertation serves as a testament of my family's unwavering support, persistent inspiration, and unconditional love.

- Sarang

Table of Contents

List of Figures

List of Tables

Synopsis

Animals use their sensory systems to detect and discriminate cues with varying physical and chemical characteristics from their multisensory environment, facilitating the percept formation. In such a dynamic and complex sensory environment, the processing and integration of multisensory stimuli is essential for them to perform critical functions (1–9). Therefore, understanding how and why sensory stimuli with varying characteristics interact and influence decision-making is of significant importance in behavioural neuroscience. While, most of the sensory systems are known to use multiplexing to encode different aspects of a single sensory stimulus, such as frequency and amplitude (10,11), the rodent olfactory system can process sensory stimuli with completely distinct physico-chemical characteristics, such as mechanical and chemical information (12–18). This unique property of the olfactory system makes it an ideal model to study multimodal decision-making using a single sensory organ. Therefore, probing the 'multimodal' aspects of information processing through rodent olfactory system is fundamentally important.

In nature, chemical signals exist as odour plumes, which are associated with the airflows that allow the dispersion of odorant molecules in the environment. Animals sense the odorant molecules that are being carried by the mechanical force exerted by airflows and encode the relevant information in order to make decisions (19–25). Sniffing is the first step in odour perception and is an active sensory behaviour that involves collecting odour molecules through the nose. Rodents sniff with frequencies ranging from 4Hz to 12Hz to gather odorant information from the surroundings (26). Odorant molecules are delivered to the olfactory sensory neurons (OSNs) through the nasal cavity, which is facilitated by animals' sniffing behaviour. These molecules bind to the receptors (OR) on OSNs that are embedded in the turbinates of the main olfactory epithelium (MOE) (27). The majority of these ORs are G-protein coupled receptors (18,28). When odorant molecules bind to ORs, a series of events occurs that transforms the chemical information of odours into a sequence of action potentials (29–31). This electrical information is subsequently transmitted to the nerve endings of OSNs in the glomerulus, a neuropil-like structure in the olfactory bulb (OB). In the glomeruli, OSNs form synapses with Mitral/Tufted cells (M/T cells), which are the projection neurons of the OB. M/T cells receive inhibitory inputs from interneurons in the glomerular layer, as well as those in the external plexiform and granule cell layers (32–35), which are known to refine the activity of M/T cells in order to increase signal to noise ratio (36–38). These refined signals

are then transduced to olfactory cortical areas for further processing (39). Recent studies have shown that, in addition to processing odour information, the olfactory system can also aid processing of mechanical stimuli (12,13). Although the neural mechanisms underlying the processing of odour information are well studied, the behavioural relevance and pathways involved in processing the mechanical information remains largely elusive. Therefore, the primary goal of this thesis was to investigate the neural mechanisms underlying the processing of airflow information through the mouse olfactory system.

We explored the involvement of mouse olfactory system in airflow information processing using a custom-built olfactometer and training rodents to detect and discriminate airflows devoid of odour molecules. We found that mice could learn to differentiate a range of airflow rates even when their whiskers were absent, ruling out the role of whiskers, which were previously believed to be crucial for anemotaxis behaviour (40,41). Additionally, when the OSNs were ablated by intranasal zinc sulphate injection or intraperitoneal administration of methimazole, an olfacto-toxic drug, the animals lost their ability to discriminate between different airflows. Moreover, removal of olfactory bulb (OB) also led to deficit in airflow discrimination abilities, proving that olfactory system is critical for airflow detection and discrimination. While performing airflow-based discriminations, animals were seen to use their nose for sampling the stimulus, resulting in an increase in the sniff frequency of animals during the decision-making period. While changes in airflow rates had no effect on animals' sniffing behaviour, different sniffing strategies were observed for airflows and odours. In contrast to odours, where the sniffing peak coincided with the discrimination time window, airflows elicited broader sniffing responses and larger temporal differences between sniffing peak and discrimination time, suggesting that animals use distinct sampling strategies for these stimuli.

To further assess the OB specific mechanisms underlying airflow information processing, we investigated the neuronal activation patterns using c-Fos, a neural activity marker. The granule cell layer of the OB, which contains the majority of the inhibitory interneurons expressing GAD 65 (42), exhibited highest levels of c-Fos expression. This was further confirmed by using in vivo recordings of calcium dynamics from a population of GABAergic (GAD 65 expressing) interneurons. Micro-endoscopic calcium imaging from these inhibitory interneurons revealed that the GC population activity was dependent on the stimulus strength. With an enhancement in the airflow rates, the amplitude of calcium transients increased. In addition, a refinement in the overall population activity was also observed as animals learnt to discriminate different airflows. This finding prompted us to study the causal

link between the interneuronal activity and its contribution towards processing of mechanical stimuli. To achieve this, we used optogenetics to modulate this inhibitory circuit function in a bidirectional manner. Optogenetic modulations were carried out via light-activated proton pumps, allowing H^+ ion efflux (Archeoshodopsin - Arch) or cation channels, allowing cation influx (Channelrhodopsin - ChR2), expressed in GAD 65 interneurons. Since GAD 65 interneurons form inhibitory synapses with M/T cells, stimulation of these interneurons via activating ChR2 increases the inhibition on M/T cells. While increased inhibition (ChR2 activation) led to poorer airflow rate discrimination, decreased inhibition (Arch activation) resulted in better discrimination. However, as compared to airflow discriminations, the same optogenetic modulations during odour discriminations resulted in opposite behavioural phenotypes, indicating that optimal synaptic inhibition needed for refining olfactory and mechanosensory information are distinct. By altering both airflow and odorant components i.e. by applying combined stimuli of Flow1+odorant1 vs. Flow2+odorant2, the opposing effect of optogenetic modifications were nullified, thus confirming the association between mechanical and odorant information in olfactory perception. Hence, our findings provide novel insights into the pre-cortical mechanisms underlying airflow information processing through rodent olfactory system. Additional studies on 'multimodal' information processing in OB are required to further understand the behavioural relevance of mechanosensation through olfactory system.

Finally, the overall goal of this thesis work was to extend the knowledge of olfaction to study it in context of health and disease. Since anosmia, total loss of olfaction, and/or hyposmia, lowered sense of smell, are symptoms linked with many neurodegenerative diseases, such as Parkinson's and Alzheimer's (43–47), investigating olfactory fitness in healthy subjects and patients with brain dysfunctions are critical. In addition, olfactory dysfunctions are also observed in some upper respiratory tract infections (48). Since the outbreak of coronavirus 2019 (COVID-19), multiple studies have revealed that patients with COVID-19 infections show various olfactory deficits (48–52). Even after the recovery from COVID-19, the subjects exhibited persisted olfactory impairments (53–56). Therefore, probing olfactory dysfunctions is critical in post-COVID era.

Breathing is the initial action that permits sampling of odorant molecules for olfactory perception (57). However, information on how sniffing behaviour modulates olfactory perception remains largely elusive. Breathing, in addition to facilitating olfactory perception, also has multiple physiological roles such as regulation of homeostasis, metabolism, brain

activity, attention and memory (58–66). Therefore, the major goal of this study was to create a novel approach for the evaluation of breathing characteristics during olfaction-based cognitive tasks and extend this framework to assess breathing patterns under disease conditions. To achieve this, we combined an already-existing Olfactory Action Meter (OAM) with a thermocouple-based pressure sensor, allowing us to monitor the breathing patterns of individuals while they performed olfaction-based cognitive tasks with a high resolution (30 ms).

Measurement of breathing patterns while subjects performed odour-based cognitive tasks revealed that, in presence of the odour stimuli, subjects exhibited longer high-amplitude inhalations and shorter high-amplitude exhalations, which resulted in a concurrent increase in breathing frequency. Since COVID-19 recovered subjects have been demonstrated to have persistent olfactory impairments, we first employed this method to evaluate the breathing patterns of these individuals (53–56). Our study revealed that COVID-19 recovered participants displayed distinct sampling behaviours, i.e. exhibiting higher inhalation and exhalation amplitudes during the olfactory detection process, compared to control subjects. Therefore, this novel experimental approach provides us with a reliable method to evaluate the sampling behaviour of individuals with olfactory impairments, which is pertinent to a variety of disease conditions. Further, these results prompt us to investigate whether mechanosensation-driven modulation of olfactory perception prevails in humans.

CHAPTER 1

Introduction

Olfactory and whisker systems are the major sensory systems used by rodents to execute critical functions that include navigation, identification of conspecifics, finding a prospective mate, eluding a predator, locating food, and determining the texture of nesting materials (67–71). Rodents demonstrate active sensing behaviour by sniffing and whisking, two rhythmic and synchronous behaviours coupled by orofacial motor neurons, as they explore their natural habitat (72–74). Chemical cues that are associated with food or mate sources are transported to animals with the help of turbulent airflows that exists in nature (21,75,76). Considering the strong association between odour plumes and airflows, it is critical for animals to sense airflow fluctuations in order to form an efficient olfactory percept. Since whisker follicles are abundant in mechanoreceptors, they were considered as the primary sensory organ that collects information to facilitate animals' taxis behaviour towards airflows (40,41). Recent studies have revealed that olfactory sensory neurons (OSNs) can also process mechanical stimuli (12–14,77). Therefore, studying the functional relevance and the neural mechanisms underlying mechanosensation through olfactory system is essential for better understanding of olfactory perception.

1.1. Rodent olfactory system

Detection and discrimination of the chemical cues are crucial for organisms in order to perform functions important for their reproduction and survival. Ranging from a single cell bacterium to a multicellular organism, all organisms have developed apparatuses capable of sensing these chemical signals (78). Anatomically, the olfactory system can be subdivided into three major parts (29) 1. Nasal Cavity (Olfactory system periphery), 2. Olfactory Bulb (OB) and 3. Olfactory Cortex. The sensory apparatus of the olfactory system lies in the nasal cavity. The nasal cavity contains a number of sensory subsystems that can sense a variety of stimuli with varying physico-chemical properties, making the olfactory system of rodents unique. This distinctive property of olfactory system makes it an ideal candidate to study the mechanisms underlying multimodal information processing using a single sensory organ.

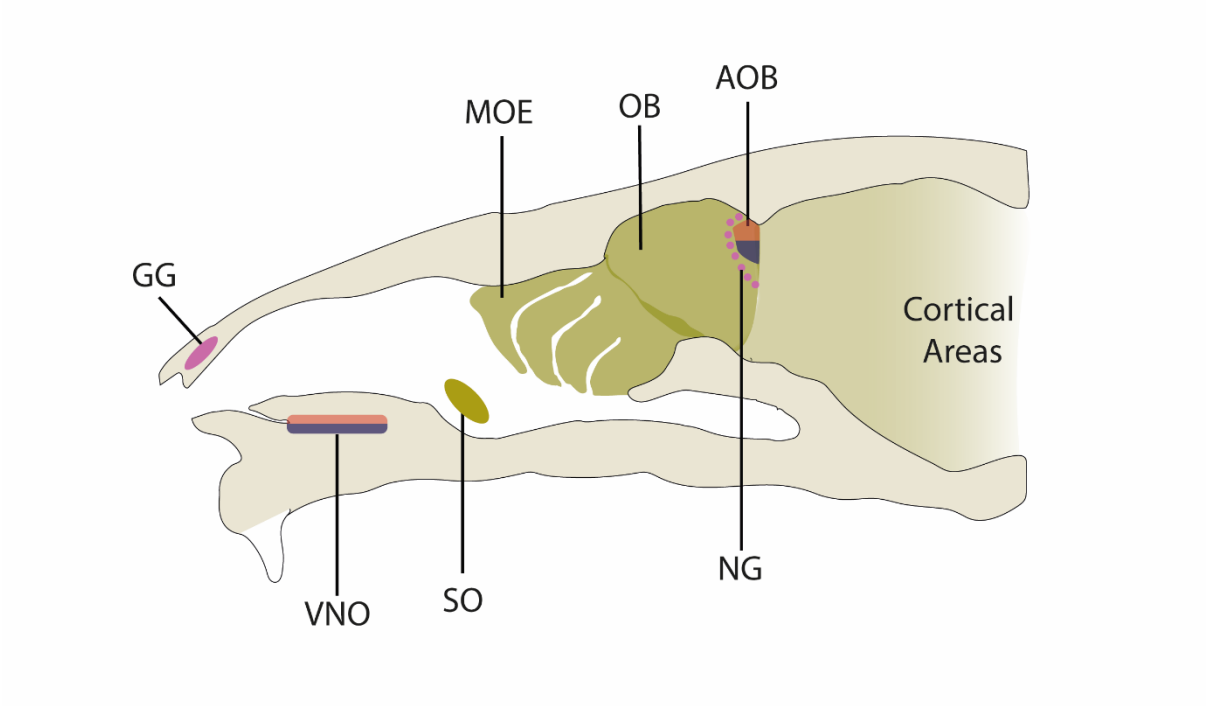

Figure 1-1 – The mouse olfactory system

The Schematic representation of the rodent olfactory system and the subsystems. GG represents Gruenberg Ganglion that sends projection to the necklace glomeruli (NG). VNO – Vomeronasal Organ projects to the accessory olfactory bulb (AOB), SO – Septal Organ projects to the Main olfactory bulb (MOB), MOE – Main olfactory epithelium also projects to the MOB. *Adopted from Hussain A. 2011, Nature Precedings* (79).

1.1.1. Nasal Cavity

The rodent nose is made up of four main olfactory subsystems: The Main Olfactory Epithelium (MOE), the Vomeronasal Organ (VNO), the Septal Organ (SO), and the Grueneberg Ganglion (GG). These subsystems comprise specialized sensory neurons that respond to specific stimuli and transport sensory information to distinct areas in the olfactory bulb (Figure 1-1).

1.1.1.1. Main Olfactory Epithelium (MOE)

In the olfactory realm, rodents sniff with frequencies ranging from 4Hz to 12Hz to receive information from their surroundings (26). The influx of airflow created by sniffing directs the odorant molecules to travel through the nasal cavity. On reaching the posterior end of the nasal cavity, these odorant molecules bind to the receptors of the olfactory sensory

neurons (OSNs) that are embedded in the turbinates of the main olfactory epithelium (MOE) (27). Olfactory epithelium is also rich in other types of cells such as glial cells, sustentacular cells, and basal cells, which support and regulate OSN turnover (80,81). Each OSN in the olfactory epithelium is known to express a single receptor out of a large repertoire (>1000) of receptors. These ORs are members of the G-protein coupled receptor (GPCR) superfamily having seven transmembrane domains (82–84). A single OR can bind to a wide range of odorants, while a single odorant can excite numerous ORs, resulting in the creation of a combinatorial code (84,85). The olfactory transduction process begins with the binding of an odorant molecule to the receptor. The binding results in the release of the GTP-bound alpha-subunit of G-protein, which activates adenyl-cyclase. Adenyl-cyclase is a protein that aids the conversion of adenosine triphosphate (ATP) to 3',5'-cyclic adenosine monophosphate (cAMP). When the intracellular concentration of cAMP rises, cyclic nucleotide-gated (CNG) channels open, allowing sodium and calcium ions to enter and chloride ions to exit. The net influx of Na+, Ca2+ and efflux of Cl- causes the depolarization of the OSN leading to generation of action potentials (Figure 1-2) (29–31). The depolarization of OSNs also happens via other secondary messenger cascades such as inositol triphosphate (IP3), and cyclic guanosine monophosphate (cGMP) when specifically stimulated with amino acids and bile salt odorants (86–88). The chemical information of an odorant that the OSNs transform into electrical signal is transmitted to the olfactory bulb (OB), which is the next relay station in the olfactory processing (89,90).

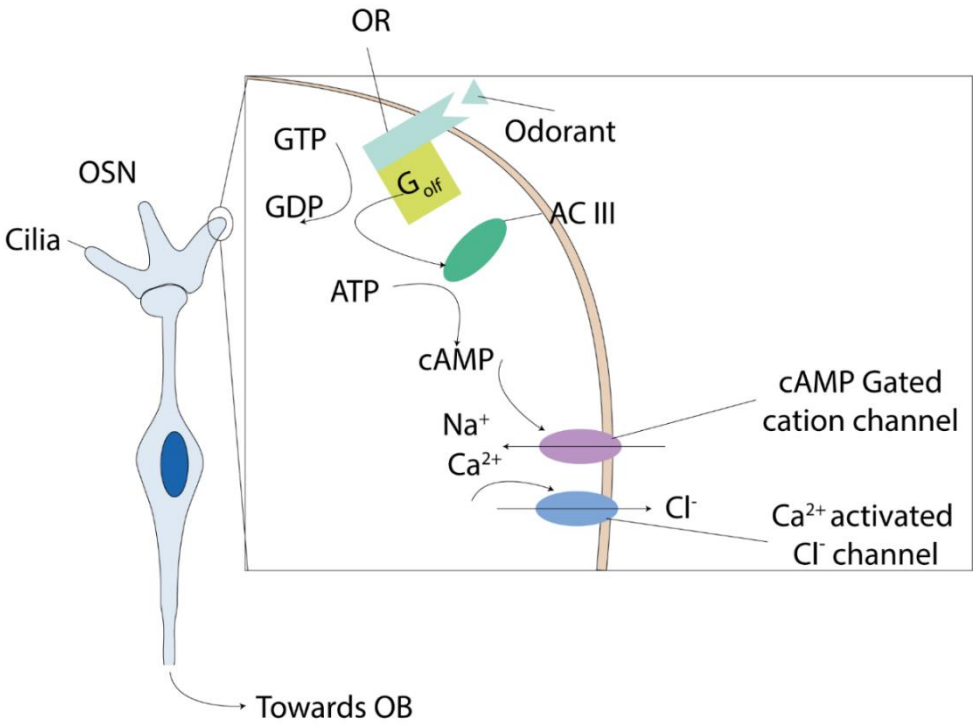

Figure 1-2 – The mouse olfactory signal transduction cascade

The Schematic diagram representing the signal transduction that takes place after odorant molecule binds to the olfactory receptors (OR). This binding leads to the release of α- bound G_{olf} subunit, which activates the adenyl cyclase III and leads to increase in the concentration of cAMP. cAMP binds to the nucleotide gated channels and allow the influx of sodium and calcium. The increase in intracellular calcium concentration opens calcium activated chloride channel which allows the chloride ion to leave the cell resulting in the more depolarizations of the cell. Once the cell reaches the depolarization threshold, it fires an action potential and this information is further transduced to olfactory bulb (OB). *Adopted from Hussain A. 2011, Nature Precedings* (79).

Most OSNs expresses a single OR from a pool of different receptors with an exception of Membrane-spanning four-pass A (MS4A) receptors. These are the non-GPCR receptors specifically found on necklace sensory neurons (91). Aside from conventional GPCRs and MS4A type receptors, the OSNs expresses a few other broad families of receptors, including trace amine-associated receptors (TAARs) and transient receptor potential channels (TRPs). Low concentrations of amines selectively activate TAARs where as TRPM5 shows responsiveness towards pheromones (92,93). In the epithelium, OSNs expressing various ORs are organized into four distinct zones. These zones span along the anterior-posterior and dorsal-ventral axes of the epithelium and OSNs belonging to these zones send their axons to stereotypic locations in OB (27,94). In addition to sensing chemical signals, OSNs exhibit mechanosensitive properties as well, the relevance of which is undetermined (12,13). Sensing the mechanical pressure produced by the airflows is one possible use of the OSNs' mechanosensitive property. Few investigations have demonstrated that airflows in double-tracheotomized animals under anaesthesia can cause oscillatory activity in the OSNs and the olfactory bulb (14,77). Even though these results indicate towards the possibility of olfactory system being able to detect the airflows, the studies examining the role of the olfactory system in achieving this behaviour are lacking.

1.1.1.2. Vomeronasal Organ (VNO)

The vomeronasal organ (VNO) is an olfactory sensory subsystem found in nearly all mammals. It is positioned in the anterior region of the nasal cavity, adjacent to the nasal septum (Figure 1-1). VNO is primarily engaged in the detection of volatile and non-volatile pheromones (95). The VNO is comprised of specialized sensory neurons (Vomeronasal

sensory neurons - VSNs) that are arranged in a pseudostratified neuroepithelium and detect chemical cues that initiate innate behavioural responses e.g. lordosis, socio-sexual behaviours. Chemical signals that enters the nasal cavity are absorbed into the VNO lumen where they bind to the receptors expressed by the VSNs. The VNO neuroepithelium in rodents is divided into two different zones: apical and basal. The chemical mechanisms underlying stimulus detection by apical and basal VNO sensory neurons are distinctive. These two VNO subsystems express discrete vomeronasal receptor V1Rs and V2Rs respectively that project to separate areas of the accessory olfactory bulb (AOB). VNO spatial segregation correlates with the differential expression of G-Protein subunits in V1R and V2R receptors (96–99). V1Rs express the Gαo subunit, whereas V2Rs express the Gi2Gαi2 subunit. Ligand binding to these receptors activates G-protein pathway, which is the first step in a phospholipase C (PLC)-mediated signaling cascade to transduce sensory inputs (100,101). Aside from V1Rs and V2Rs, a subset of neurons in the VNO express five members of the formyl peptide receptor (FPR) family, four of which are apical and one of which is basal. FPR neurons were found to show selectivity for the peptides that are signatures of pathogenic micro-organisms (102–104). Additionally, VNO neurons also express major histocompatibility complex (MHC) molecules, which suggests the role that VNO may play in recognizing potential pathogens (105,106). The spatial segregation of the subsystems at the VNO periphery is also maintained in the AOB wherein apical and basal VSNs transduce signals to the glomeruli in the rostral and caudal AOB, respectively (100,107,108).

1.1.1.3. Septal Organ (SO)

The septal organ is a small island of olfactory neuro-epithelium located bilaterally at the ventral base of the nasal septum near the nasopharynx's entrance (Figure 1-1). Septal organ is separated from main olfactory epithelium by respiratory epithelium. Many mammals, including rats, mice, rabbits, hamsters, opossums, guinea pigs, bandicoots, and koalas, have this olfactory subsystem (109–113). The SO, like the MOE, is composed of ciliated OSNs, microvillar cells, supporting cells and bowman's glands (114). Although MOE and SO cells have certain similarities, they also have some distinctions. Septal organ has OSNs in 2-3 layers, whereas MOE has sensory neurons in 6-8 layers. Septal organ cells also feature flattened stomata and shorter dendrites with large knobs (115,116). Mouse SO mostly expresses a few receptors from approximately 120 OR genes, with MOR256-3 receptor expression being the most abundant (112,117). The same receptors found in SO are also expressed in neurons in the

ventromedial zone of the main olfactory epithelium (117). The sensory neurons of the septal organ express $G_{\alpha olf}$ and ACIII, indicating that signal transduction in these neurons occurs via a cAMP pathway similar to that of the sensory neurons of the main olfactory epithelium (116). Following initial processing by sensory neurons, the signal is transmitted to the posterior and ventromedial regions of the main olfactory bulb (118). Although SO neurons account for a very small proportion of the total olfactory receptor fraction, their neurons respond to a wide range of chemicals with varying properties. In addition to responding to odorants, these sensory neurons have been shown to elicit activity towards mechanical stimulation as well, the functional relevance of which still remains elusive (13,119).

1.1.1.4. Grueneberg Ganglion (GG)

Grueneberg Ganglion is mainly a cluster of neurons (~500 neurons) that is located bilaterally in the anterior vestibule of the nasal cavity (Figure 1-1) (120). GG is known to be helpful in: mother new-born interactions, food choice under threat, sensing cold temperatures and alarm pheromones (120–123). GG neurons expresses OMP (olfactory marker protein a specific marker for mature chemosensory neurons) and their axons projects to the necklace glomeruli in the caudal main olfactory bulb (124). The necklace glomeruli are also the central target of the guanylyl cyclase D neurons. A substantial number of these OMP +ve neuron are known to express V2r83 receptor which is a V2R subtype known to be present in basal neurons of VNO (125). Some of the neurons that have V2r83 receptors also co-express guanylyl cyclase subtypes (GC-G and GC-A), indicating the existence of cGMP mediated signaling transduction pathway (126). Apart from GC subtypes, GG neurons also express phosphodiesterase 2a and cGMP-dependent kinase II which proteins associated with cGMP signaling (127). Although the GG's primary cGMP signaling route is shared with GC-D neurons as they both project to necklace glomeruli, the GG's specific chemoreceptor repertoire implies that it is a discrete olfactory subsystem developed specifically to sense the degree of coolness and alarm signals.

1.1.2. Olfactory bulb (OB)

The axons of the OSNs converge in a receptor-specific manner and project to a locus in OB known as the glomerulus. Each OSN that expresses the same OR innervates two glomeruli, one on the lateral and one on the medial surface of the OB (128). The axonal convergence of OSNs into specific glomeruli generates a functional topographic arrangement in OB (129). The spontaneous activity generated in OSNs is responsible for this unique convergence (130).

Eliminating spontaneous activity by overexpressing specific ion channels or increasing activity through optogenetics alters glomerular map formations (130–133). In the glomerulus, OSNs form excitatory glutamatergic synapses with Mitral and Tufted cells (M/T cells). M/T cells lie in the mitral cell and external plexiform layer of the OB and transduce signals to the distinct areas in the olfactory cortex (Figure 1-3A). Mitral cell axon projections are dispersed across the olfactory cortex (piriform cortex, orbitofrontal cortex, anterior olfactory nucleus, olfactory tubercle) (Figure 1-3B), whereas Tufted cell axon projections innervate the anterior olfactory nucleus and the cap region of the olfactory tubercle (134,135). Besides that, the spontaneous activity of these M/T cells are phase locked with separate phases of the breathing cycle. Tufted cells fire during the inhalation, whereas Mitral cells fire during the exhalation phase (136).

Each glomerulus of the OB is innervated by the dendrites coming from 20-30 M/T cells that receives odour information from ~5000 OSNs. This high convergence ratio ensures optimal signal amplification, resulting in a high signal-to-noise ratio (137–140). Odour information in M/T cells is further tuned by interneurons located in the glomerular layer (GL), external plexiform layer (EPL), and granule cell (GCL) layer of the OB. Periglomerular (PG) cells, short-axon (SA) cells, and External Tufted (ET) cells are all found in the GL layer and are together known as Juxtaglomerular cells. These juxtaglomerular cells provide inhibitory input to M/T cells (32–35). M/T cells also form inhibitory dendodendritic synapses with granule cells (GCs) located in the GCL. These GCs receive excitatory glutamatergic input from M/T cells and inhibit them using GABA as an inhibitory neurotransmitter. If GC inhibits the same MTC from which it receives the excitatory inputs, it is known as recurrent inhibition, while GC inhibiting neighbouring MTCs is known as lateral inhibition (Figure 1-3A). The reciprocal dendrodendritic interactions between MTCs and GCs control the overall signal-to-noise ratio of the OB (36–38). M/T cells transport refined neural signals from the OB to various areas of the olfactory cortex.

1.1.3. Olfactory Cortex (OC)

The olfactory cortex constitutes areas of the brain that receives input from the olfactory bulb. The axon bundles of the output neurons of the OB form an olfactory tract and terminates in the olfactory cortex. The olfactory cortex includes the piriform cortex, the olfactory tubercle, the orbitofrontal cortex, the prefrontal cortex, the entorhinal cortex, the anterior olfactory

nucleus, the tenia tecta and the amygdala (Figure 1-3B) (39). Out of different areas receiving projections from the M/T cells, the piriform cortex (PCx) is the most prominent one (141).

The PCx is a laminar structure with three distinct layers: Layer I receive afferent fibres from the OB, Layer II is a dense layer of pyramidal cells and semilunar cells, and Layer III is the innermost layer, also consisting of pyramidal cells that are found in superficial areas. MTCs from a single glomerulus send their projection across the PCx with no apparent spatial preference. As a result, when odour information reaches PCx, it lacks the spatially segregated chemotopic map observed in GL and exhibits sparser activation patterns (142–144). The activity of PCx neurons is also modulated by associational fibres that originate in other olfactory cortical regions such as the anterior olfactory nucleus (AON), olfactory tubercle (OT), entorhinal cortex, and amygdala. Aside from afferent and associational fibres, other areas that send input to PCx include the thalamus, hypothalamus and brainstem (145,146).

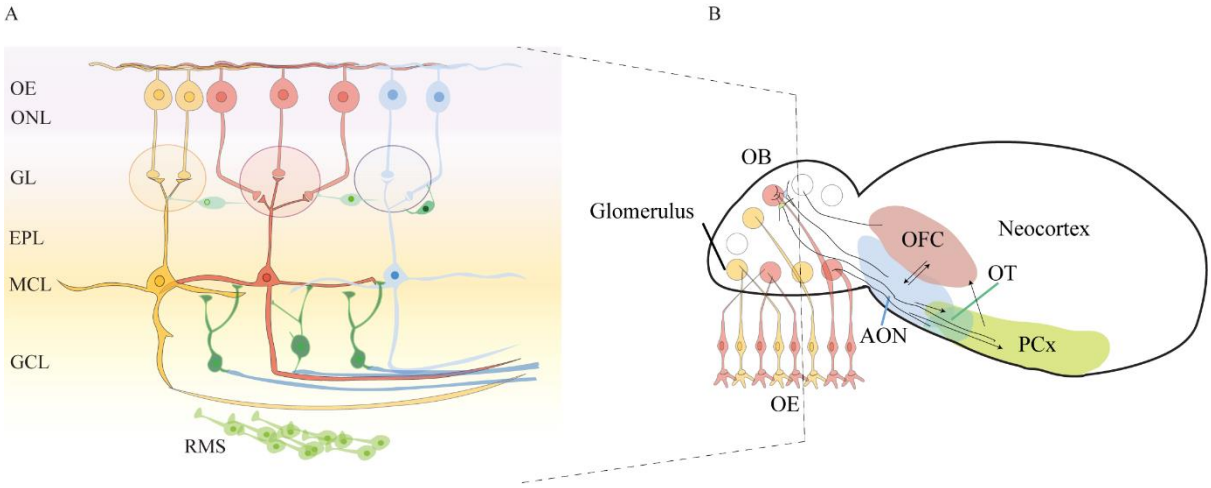

Figure 1-3 – The mouse olfactory bulb and cortex

A) The schematic representation of the layered structure of OB. The axons of the OSNs send their projections in the receptor specific manner to the glomeruli where they make synapses with M/T cells. These cells are located in external plexiform layer (EPL) and mitral cell layer (MCL). The inhibitory neurons in the GL layer and the GCL layer modulates the overall activity of the M/T cells. This information is then sent into different cortical areas. *Adopted from Sakamoto M. 2014, Frontiers in Neuroscience* (147).

B) The schematic representation of connections between OB and olfactory cortex. M/T cells project to different areas in the brain that is collectively called as olfactory cortex. These areas mainly

include, piriform cortex (PCx), anterior olfactory nucleus (AON), olfactory tubercle (OT) and orbitofrontal cortex (OFC). *Adopted from Mori K. 2013, Frontiers in Psychology* (148).

AON is another olfactory cortical region that is the first recipient of odour input and maintains odour engrams required for odour memory behavioural expression (149). It also mediates interbulbar interactions as it gathers information from the ipsilateral M/Ts and provides feedback to the GCL in contralateral OB (149,150). Another cortical area important in odour characterization that receives direct olfactory information from PCx is the orbitofrontal cortex (OFC). The OFC neurons are activated during sampling of stimulus and consumption of rewards (151,152). Another cortical region that is closely connected to the OB and processes reward information is the olfactory tubercle (OT). The OT is found in the ventral striatum and has substantial anatomical connections to the reward centres of the brain (153–155). Along with projecting to other cortical areas, the PCx and AON also send extensive inhibitory feedback projections to the GC and PG layer in the OB (141,156,157). Cortical feedback on M/T cells enhances odour-evoked inhibition, which optimize the signal-to-noise ratio to generate an efficient percept (141).

1.2. Rodent whisker system

In rodents, the whisker system, much like olfactory system, plays a vital role in navigation, identification of nesting materials, social behaviour, texture recognition, and sensing the wind speed and direction etc. The whisker system has been an attractive model in recent decades owing to its distinctive somatotopic projection map that is conserved from the periphery (whisker pad) to the barrel cortex.

Whiskers are hair-like structures that are arranged in a grid pattern on both sides of the snout. Rats and mice have five rows of whiskers, with the top two rows (A–B) having four whiskers each and the bottom three rows (C–E) having around seven. Along the caudal end of the mystacial pad are four particularly big whiskers called straddlers (158,159). The mystacial pad is constituted of muscles that can be categorized as intrinsic and extrinsic. Such muscles are innervated by distinct branches of the facial nerve, with intrinsic muscles located within the pad and extrinsic muscles situated outside the mystacial pad (160). During an exploratory

whisking cycle, the whiskers first protract, controlled by intrinsic muscles, and subsequently retract, mediated by extrinsic muscles (161).

Whiskers differ from other hairs in that they have larger follicles surrounded by blood sinus and cuticles lined up with several scales (159). Each whisker follicle is densely packed with mechanoreceptors and free nerve terminals of distinct kinds. The vibrissae, as mechanical transducers, mediate the transduction of the touch signal into these receptors. Based on their location and size on the snout, they have been classified as 1) micro-vibrissae, which are small and thin hairs around the nose tip, and (ii) macro-vibrissae, which are long stiff mystacial hairs caudal to micro-vibrissae on the whisker pad (162). Micro and macro vibrissae are believed to conduct distinct functions. Micro-vibrissae acquire detailed tactile information related to object and texture recognition, whereas macro-vibrissae transmit spatial information such as space localization (162,163).

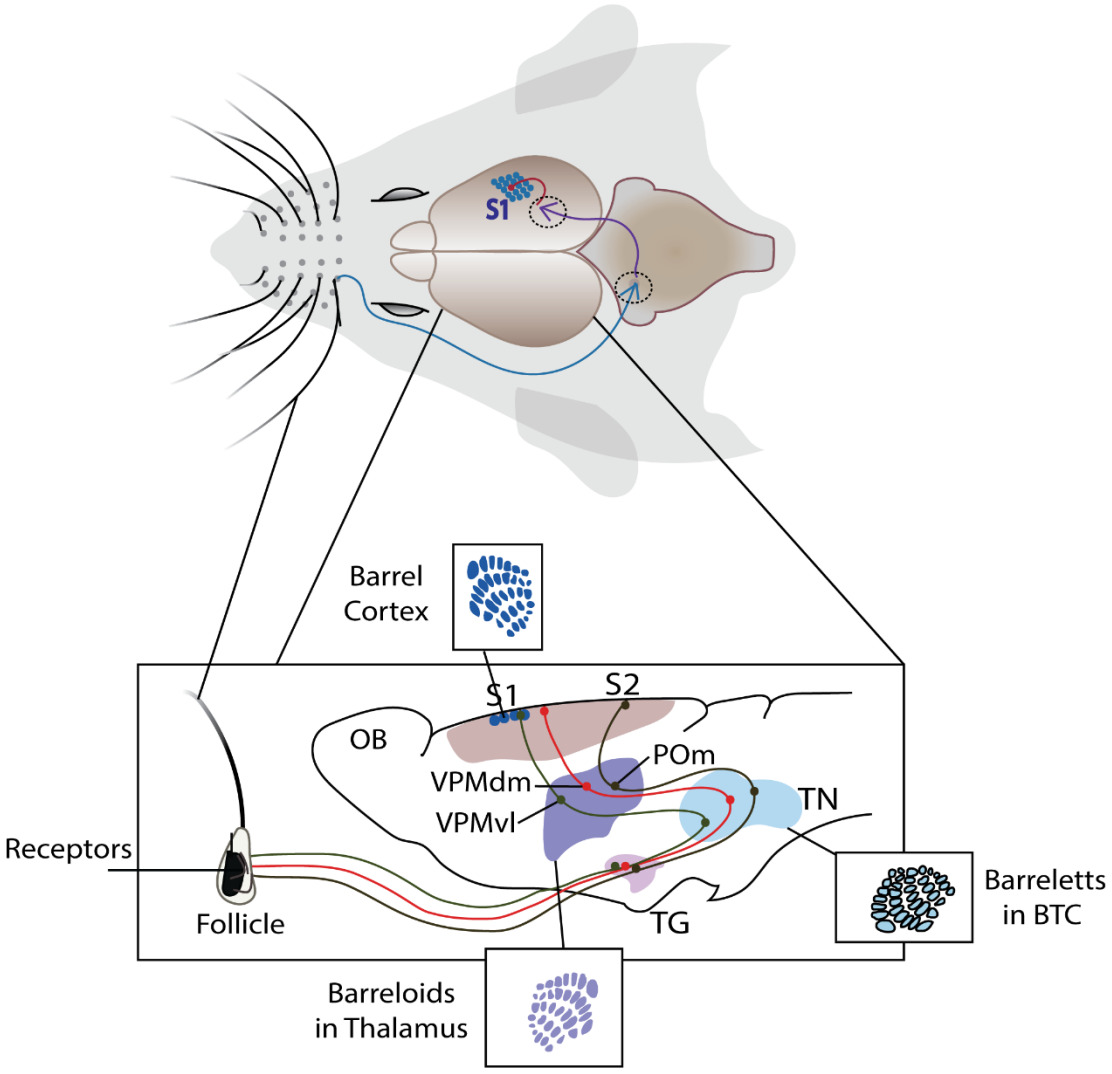

Figure 1-4 – The mouse whisker system pathway: From whisker to barrel cortex
The Schematic diagram representing the signal transduction that takes place during information processing through whisker system. Whisker deflection is sensed by the mechanoreceptors in the whisker follicles which sends the signal to the BTC/TC (Brainstem Trigeminal Complex/Trigeminal Nuclei) by means of trigeminal ganglions. The information then goes to the Thalamus via three different pathways (POm – Posterior thalamic nucleus, VMPdm – Dorsomedial nucleus of ventromedial posterior thalamus, VPMvl – ventrolateral nucleus of ventromedial posterior thalamus). The information then reaches the primary and secondary somatosensory cortex. The somatotopic organization of whiskers remains conserved throughout the signaling pathway in form of the Barrelettes (in BTC), Barreloids (in Thalamus) and, Barrels (in somatosensory cortex). *Adopted from Adibi M. 2019, Frontiers in system neuroscience* (68) *and Maravall M. 2014, Current opinion in neurobiology* (164).

Micro and macro whiskers both innervate a follicle containing nerve terminals and mechanoreceptors of various types and morphologies with distinct tuning properties. The follicle is comprised of Ruffini corpuscles, free nerve terminals, and Merkel cell complexes, with the latter being the most prominent (165,166). Different mechanoreceptors exhibit distinct adaptation patterns and are responsible for converting mechanical energy into electrical impulses. These mechanoreceptors open and close in response to the mechanical force and codes for different stimuli properties, including amplitude, speed, frequency, acceleration, duration, and direction (71,167–169). As the stimulus deflects the whisker, its motion conveys mechanical energy to the follicle, where it is transformed into action potentials. The electrical impulse is subsequently transmitted to the trigeminal ganglion, which delivers information to the trigeminal nuclei, also called the brainstem trigeminal complex (BTC) (Figure 1-4).

1.2.1. Trigeminal Ganglion: Structure and Function

The trigeminal ganglion, also known as the semilunar sensory ganglion or Gasserian ganglion, is a crescent-shaped structure located within the middle cranial fossa in Meckel's cave. The ganglion is the major sensory ganglion of the fifth cranial nerve (CN V). The trigeminal ganglion is crucial in the expression of different neuropeptides and signaling molecules that are important in gene expression, sensory information regulation, and peripheral and central sensitization. Trigeminal ganglions (TGs) are comprised of cell bodies with distal axons that innervate the whisker follicles and proximal axons that innervate the ipsilateral BTC (Figure 1-4) (163,170). Each whisker follicle is heavily innervated by TGs, with up to 200

ganglion cells per whisker follicle (171,172). This high degree of convergence provides quick and sensitive information processing and, as a result, effective decision-making. These neurons are extremely sensitive to whisker deflection, with approximately half of the neurons activating with less than 1° whisker deflection (173). It is reported that the TGs, which adapt quickly, codes for the velocity and acceleration of whisker deflection. On the other hand, other slowly adapting ganglion cells respond to whisker position and contact angle (174–176). TGs are somatotopically arranged, with the dorsal representation of caudal arcs and medial representation of dorsal rows transmitting information in the well-structured form to trigeminal nuclei (175,176).

1.2.2. Trigeminal Nuclei or Brainstem Trigeminal Complex (BTC)

The trigeminal sensory complex is the first relay centre in the processing pathway that carries tactile information from the whiskers to the somatosensory cortex. The trigeminal complex in the brainstem is generally separated into two parts: the principal sensory nucleus (PrV) and the spinal nucleus (SpV). The spinal nucleus (SpV) is further subdivided rostral-caudally into three subnuclei 1. Oralis (SpVo) 2. Interpolaris (SpVi) and 3. Caudalis (SpVc) (170). Trigeminal nuclei neurons exist as distinct clusters known as barrelettes in each subnucleus except oralis (Figure 1-4). These barrelettes comprise a cluster of 150-200 neurons exhibiting different attributes. Similar to that of TGs, it is known that sensitive BTC neurons adapt slowly, whereas less sensitive neurons adapt quickly. The somatotopic arrangement of barrelettes remains preserved and is identical to that of the arrangement of whiskers on the mystacial pad (177–180). The principal sensory (PrV) and interpolaris sub-nuclei (SpVi) provide the majority of projections to the thalamus, the next relay station in the whisker–barrel pathway (177,178,181). In addition to projection neurons, trigeminal nuclei are rich in GABAergic and glycinergic inhibitory interneurons, which shape the receptive field of barrelettes (182). The BTC also receives feedback projections from the primary and secondary somatosensory cortex, which can influence the overall output of projection neurons (182)(183).

1.2.3. Thalamus

Thalamus is a primary signal processing centre that conveys the information into the cerebral cortex. The neurons of the brainstem trigeminal complex transmit signals to the

thalamus, mainly to the ventro-posterior nucleus (VPM), the posterior thalamic nucleus (POm), and intralaminar thalamic nuclei (184,185). VPM receives both single and multiple whisker input from principal sensory neurons of the trigeminal nuclei (186). VPM constitutes barreloids (Figure 1-4), which are somatotopically organized and preserved columnar structures having whisker representations identical to barrelettes (187). Each barreloid contains 250-300 neurons and has size proportional to the length of the whiskers (188). The barreloids are more prominent in the dorsomedial region of the VPM (VPMdm) and fade away in the ventrolateral part (VPMvl). VPMdm only receives projections from PrV neurons that are associated with single whiskers. On the other hand, other PrV and Interpolaris (SpVi) neurons with dendritic arbors spread across several barrelettes projects to the posterior thalamic nucleus (POm) and ventrolateral VPM (VPMvl) respectively (177,179,184,187). These centres (VPMdm, VPMvl and POm) comprised three pathways through which information about whisker stimulations can flow from the thalamus to the cortex (Figure 1-4).

The pathway that makes synapses with the VPMdm is called the lemniscal pathway. This is the primary pathway for relaying single whisker information from ipsilateral PrV barrelettes to contralateral VPMdm barreloids to barrels in the primary somatosensory cortex (185). The Neurons primarily send their projections to layer IV of the primary somatosensory cortex, although there are axon terminals in layers V and VI. The cells in the barreloids convey whisker input with precisely timed single action potentials at short latencies (189–193).

The other pathway that forms synapses in VPM is the extralemniscal pathway which relays signals through VPMvl. VPMvl barreloids are not as distinct as VPMdm barreloids (190,193). The extralemniscal pathway receives several whisker inputs from neurons in the caudal region of the SpVi nucleus (184,186). The output of the extralemniscal circuit is directed to layers IV and VI of the secondary somatosensory cortex and the septal regions of the primary somatosensory cortex (191,192).

The paralemniscal pathway is the third pathway that channels the sensory information from the rostral part of the SpVi nucleus to the POm and then to the primary somatosensory areas, secondary somatosensory areas, motor cortex and superior colliculus. The neurons of the POm terminate mainly in layer I, Va and the septal regions of layer IV of the primary somatosensory cortex (185). The paralemniscal route predominantly transmits whisking signals, which can be used to form sensory-motor coordination and positional reference during an active exploration task. The lemniscal and paralemniscal pathways interact and are

speculated to represent the what and where of a touch signal. In addition to serving as a relay centre, the thalamus contains interneurons, which regulate the flow of information by providing negative feedback. The thalamic reticular nucleus forms a sheet of GABAergic neurons that provides significant inhibitory inputs to VPM and POm, hence modulating their output activity (194,195).

1.2.4. Barrel Cortex

The cortical representation of vibrissae is commonly referred to as barrel field, which accounts for over 20% of the primary somatosensory cortex. The cortex is a six-layered structure that contains anatomically distinct clusters of neurons called barrels (Figure 1-4), thus the name barrel cortex. Barrels are elliptical in shape, with around 2500 neurons in each barrel. Each barrel receives a one-to-one connection from the thalamic barreloid and retains the same somatotopic layout as found in the mystacial pad (196). Layer IV of the cortex is largely made up of two types of neurons. 1. star-pyramidal excitatory cells and 2. GABAergic interneurons. Both excitatory and inhibitory neurons receive input from the VPM and project into layer II/III of the same column. The Inter barrel regions in the cortex are occupied by septa. Along with layer II/III, septal neurons project into adjacent barrels, secondary somatosensory and primary motor cortex. Layer V and VI of the cortex forms reciprocal connections with thalamic VPM and POm (196–200). Layer VI corticothalamic neurons are GABAergic and provide negative feedback connections, with the upper part innervating VPM and the lower part innervating POm, therefore, modulating the information processing in both lemniscal and paralemniscal pathways (189).

1.2.5. Modes of whiskers mediated sensation

To extract relevant sensory information from their environment, all sensory systems utilize active sensing, which entails modulating the sensory equipment in a way that best suits the task to maximize the information gain. The whisker system also exhibits active sensing when rodents sweep their mystacial vibrissae to scan the environment (201). The active sensing mechanism of the rodent whisker system can be classified into two modes. 1. Generative mode of whisking and 2. Receptive mode of whisking.

In the generative mode, the rat moves its whiskers forward and backward at a frequency of around 10Hz (162,175). Each cycle is referred to as a whisk, and it is also coupled with

sniffing through oro-facial nerves and muscles (72,73,202). The whisker motion seeks touch with objects and palpates them to gather as much information about their features. Rodents employ generative whisking to sample surface textures, identify objects, their shape and size, estimate distances, and localize objects. As mice brush their vibrissae across various objects, after contact with the surfaces, whiskers are released with tremendous velocity and acceleration (203). This event is termed as the stick slip event. The profile of stick slip events uniquely reconstructs the dynamics of the surface and specifies an object's location, texture, size, and shape (204).

However, in the receptive mode, to optimize the accumulation of vibro-tactile information from a moving object, animals keep their whiskers immobile and sense the vibrations (201,205). Percept formation in the receptive mode is aided by the magnitude and frequency of the motion of object. Animals can discriminate different amplitudes while keeping the frequencies constant, as well as different frequencies while keeping the amplitude constant (206). In the cortex, the dynamics of a vibro-tactile stimulus is encoded as the product of amplitude and frequency (70,71). As modes of sensation and behavioural state can influence percept formation, it is crucial for an animal choose an appropriate mode while exploring a particular object.

CHAPTER 2

Materials and Methods

This chapter describes all experimental procedures that are common across multiple chapters. The procedures specific to a chapter are described under the materials and methods section of that particular chapter.

2.1. Ethics Statement

The experimental procedures used in this thesis are approved by the Institutional Animal Ethics Committee (IAEC) at IISER Pune, and the Committee for the Purpose of Control and Supervision of Experiments on Animals (CPCSEA), Government of India (animal facility CPCSEA registration number 1496/GO/ReBi/S/11/CPCSEA). The usage of animals in this thesis was approved under protocol numbers IISER/IAEC/2017-02-006 and IISER/IAEC/2017-02-008.

2.2. Maintenance of animals used in the study

All experiments were conducted on adult male mice. The age of the mice at the beginning of the experiment was 6-8 weeks. Mice were housed in individually ventilated cages (IVC) and maintained on a 12-hour day-light cycle. The mice were given standard rodent bedding and nesting material. The room temperature was maintained between 24-27 °C, while the relative humidity was regulated and kept at 45-55 percent. All the experiments were performed during the light cycle. On the days of behavioural training, mice had unrestricted access to food but were subjected to a water restriction schedule, however, designed to keep them at >80% of their baseline body weight. The water restriction schedule was never more than 12 hours long.

2.3. Operant Conditioning Procedures

2.3.1. Behavioural Training under freely moving conditions

2.3.1.1. Apparatus

Custom modified eight channel freely moving olfactometers (from Knosys, Washington) (207) were used for airflow/olfactory discrimination experiments. The instruments were controlled by a customized program written in IGOR (Wavemetrics). The

device included an operant chamber where the animals were kept for behavioural training. A circular sampling/reward port secured by an IR beam was located on the right side of the operant chamber (Figure 2-1A and B). In this operant training under freely moving conditions, animals could start a trial by inserting their head and breaking the IR beam that sealed the sampling/reward port. The animal was given stimulation (airflow/odorants) once the trial was initiated. The precise onset of the stimulation was assured by a system of solenoid valves controlled by software. Airflow rates were also controlled by flowmeters connected to the olfactometer channels. Three different modes of stimulus delivery were used based on the nature of the behavioural experiment (Figure 2-1C).

Mode 1 – In this mode, the stimulus was delivered on the snout of animal from the top. The stimulus was delivered by circular tube (4 mm diameter). The distance of the delivery tube from the snout was kept fixed around 8-10 mm. The input airflow rate supplied and the actual output rate observed for mode M1 were quantified and determined to be similar (Figure 2-2A).

Mode 2 – In this mode, the stimulus delivery was targeted on the whiskers. Two protruding tubes (4 mm in diameter) delivered focused stimulation to both sides of the snout. The delivery tubes protruded sufficiently to be in the same plane as the lick tube. When the animals poked their heads into the sampling port, they were provided with the airflow stimulus on their whiskers. The radial distance between the lick port and each tube was 8 mm. The delivered input airflow rate and the observed output rate for mode M2 output tubes were quantified and found to be equivalent (Figure 2-2B).

Mode 3 – In this mode also, the stimulus delivery was targeted on the whiskers but in a diffused way. The stimulus was provided to the whiskers by four holes (4 mm diameter each) arranged in a semi arc around the lick tube. In this mode the plane of the lick tube was protruded in comparison to that of the delivery ports. When mice poked their head in the sampling port, they received the stimulus in a diffusive manner. The radial distance from the centre of lick port to that of each hole was also 8 mm in this mode. The real output rate measured for different output holes of mode M3 was quantified, and the actual observed output was determined to be as expected (Figure 2-2C).

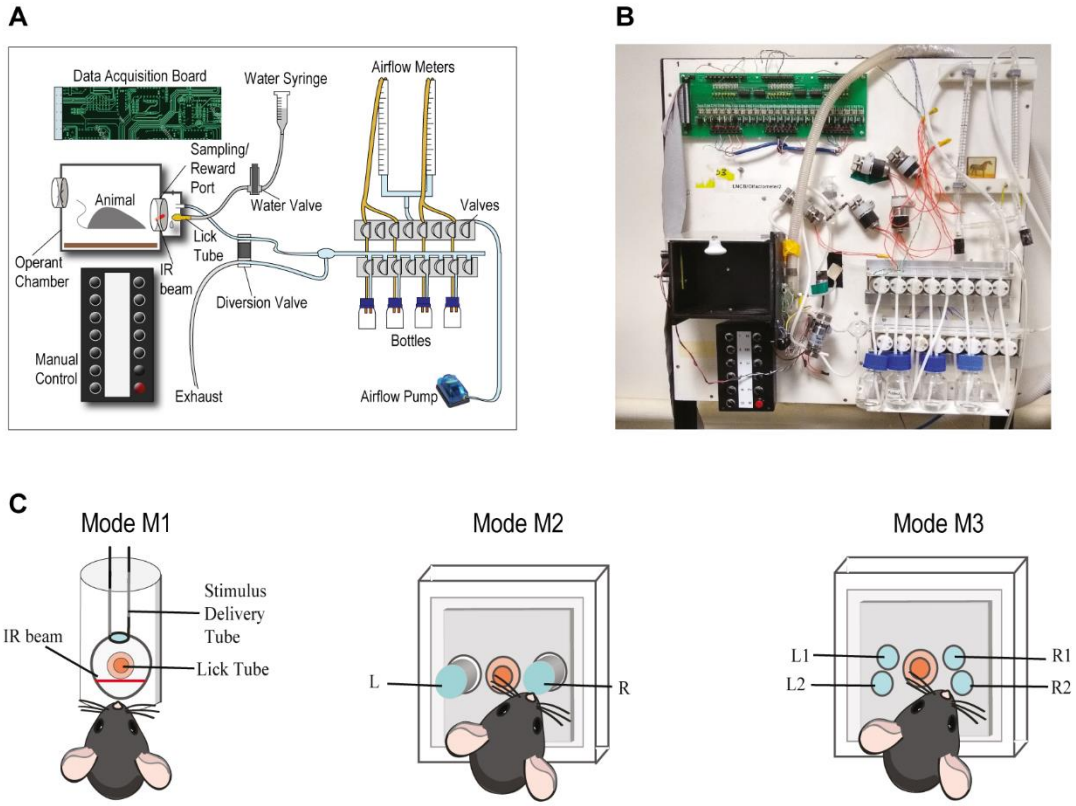

Figure 2-1 – Automated customized olfactometer for behavioural training under freely moving conditions and different modes of stimulus delivery

A) The Schematic diagram representing the olfactometer along with different components. Animal sits in the operant chamber wherein the sampling port is guarded by the IR beam. Once animal pokes the head inside the sampling port the IR beam is broken and the solenoid valve opens followed by opening of the diversion valve which leads to the presentation of the stimulus to the animal. Based on whether the stimulus is rewarded or unrewarded animal has to lick on the lick tube in order to get water reward. The room air is pumped wherein the strength of the air is controlled by the airflow meters. *Adopted from Bodyak and Slotnick 1999, Chemical Senses* (207).

B) One of the olfactometers used for behavioural training.

C) Different modes of stimulus delivery. In Mode M1 the stimulus is delivered on the snout of the animal. In Mode M2 and Mode M3 the stimulus is delivered on the whiskers of the animal in a focused and diffusive way respectively.

2.3.1.2. Task Habituation Phase

Three to four days after the start of the water deprivation schedule, the animals were subjected to task habituation training. Standard operant conditioning approaches were used to train the animals. The task habituation phase was completed in nine stages. The animals received water reward (2-3 µl) simply by breaking the IR beam in the first pre-training phase (Phase 0). This enabled the animals to locate the reward port and the lick tube. In the next stage the animals only received water when they registered at least a single lick. After 15 such trials, the subsequent phase of task habituation begins wherein the trial is initiated only when IR beam is broken by head insertion. The beam break causes the instrument valves to open, resulting in stimulus presentation for 2 seconds. The task's complexity was steadily increased from this stage onwards in order to train the mouse to lick continuously during stimulus presentation. Airflow with precise flowrate and diluted odours were delivered for the airflow and odour-based pre-training tasks, respectively. Unless otherwise specified, odours with a concentration of 1% were used and diluted with mineral oil. All of the animals completed the pre-training in three to four 30-minute sessions.

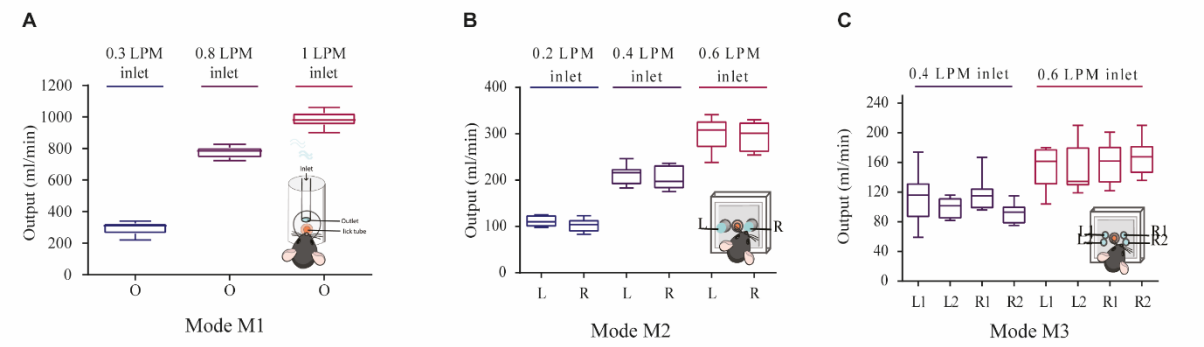

Figure 2-2 – Measured output airflow from different stimulus delivery modes

A) Outlet airflow was measured from the stimulus delivery tube in the Mode M1 while different airflows were provided as the input. For 0.3 LPM (or 300 ml/min) inlet, the measured output was 296 ± 12.58 ml/min (Mean ± SEM). For 0.8 LPM inlet (or 800 ml/min), output was 793 ± 10.44 ml/min and for 1.0 LPM (or 1000 ml/min) the output was 980 ± 15.78 ml/min. The input airflow rate supplied and the actual output rate observed were similar.

B) Outlet airflow was measured from different ports of the stimulus delivery tube in the Mode M2 while different airflows were provided as the input. For 0.2 LPM (or 200 ml/min) total inlet, the measured output was (Left port – 111.5 ± 3.625 ml/min and Right port – 102.8 ± 4.735), for 0.4 LPM (or 400 ml/min) total inlet, output was (Left port – 212.6 ± 7.131 ml/min and Right port – 203.5 ± 8.360), and for 0.6 LPM (or 600 ml/min) the output was (Left port – 303.3 ± 12.09 ml/min

and Right port – 296.5 ± 10.62). The airflow rates through left and right port for a particular inlet stimulus were non-significant and their sum were similar to that of the inlet airflow.

C) Outlet airflow was measured from different ports of the stimulus delivery tube in the Mode M3 while different airflows were provided as the input. For 0.4 LPM (or 400 ml/min) total inlet, the measured output was (Left port1 – 112.6 ± 12.23 ml/min, Left port 2 – 99.25 ± 4.758, Right port 1 – 117.5 ± 8.082 and Right port2 – 92.50 ± 4.679), for 0.6 LPM (or 600 ml/min) total inlet, output was (Left port1 – 154.5 ± 9.716 ml/min, Left port 2 – 151.3 ± 11.40, Right port 1 – 159.6 ± 9.365 and Right port2 – 166.6 ± 8.294). The airflow rates through all the ports for a particular inlet stimulus were non-significant and their sum were similar to that of the inlet airflow.

2.3.1.3. Discrimination training

All the airflow and odour-based discrimination training was performed on a Go/No-Go behavioural paradigm (207,208). The mouse initiated a trial by breaking an IR beam that guards the sampling port (Figure 2-3). This enabled the opening of one of the solenoid valves, followed by the opening of a three-way diversion valve after 500 milliseconds. After diversion valve is opened the stimulus is presented to the animal for a variable duration (specified in chapter-wise methods). The use of a diversion valve reduced the period between the onset of the stimulus and the first contact with the animal. To obtain a reward, the animal has to meet the required reward criteria based on the reward contingency of the stimulus [Rewarded (S+)/ Non-Rewarded (S-)].

The response time provided to the animal was virtually divided into four equal bins. (For example, if the given response duration is 2 seconds, it will be virtually divided into four 500 ms bins). The response time was generally kept the same as the stimulus duration. For an S+ trial to be correct animal had to register a lick in at least three of these four bins. For a correct S+ trial animal received a water reward of 3-4 µl after the end of the stimulus [Reward Criterion: Animal needs to register a lick in at least three out of four bins]. To be successful in an S- trial, the animal should not lick in more than two bins. A subsequent trial did not begin unless an Inter trial interval (ITI) of 5 seconds had passed between trials. The set ITI was long enough for the mouse to retract fast at the end of a trial. There were no regulations in place to compel the mouse to sample the odour for a minimum time before making a decision. Furthermore, there were no rules in place to restrict licking during the pre-odour time.

Stimuli were administered to the animals in blocks of 20 trials. Each of these blocks contained ten S+ and ten S- trials. The S+ and S- trials within a block were pseudorandomized

so that no more than two stimuli of the same reward contingency were delivered consecutively. The preference for a certain stimulus was avoided by counterbalancing the S+ and S- stimuli for a group of animals (for example, in a group of 8 animals, 4 mice receive one stimulus as S+ the remaining 4 animals receive another stimulus as S+). Animals were sufficiently motivated to complete 200-300 trials each day, spread out over 1-2 (30-20 min) sessions. Different instrumental readouts, such as inter trial interval and licking frequency, were used to track the motivation of animals. When the animal ceased licking for the rewarded trials, the training session was stopped.

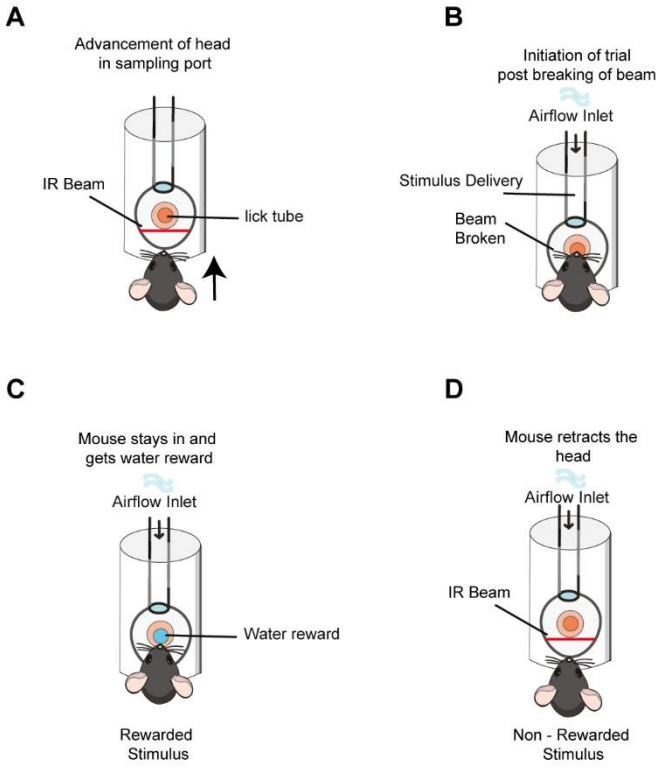

Figure 2-3 – Schematic representation of an individual trial during behavioural training under freely moving conditions

A) A trial is initiated as soon as the mouse pokes its head into the sampling port guarded by the IR beam.
B) Animal receives the stimulus and samples it.
C) If the stimulus is rewarded (S+), animal licks on the lick tube and correct licking response triggers the delivery of the water reward.
D) If the stimulus is unrewarded (S-), a trained animal doesn't lick and retracts its head from the sampling port.

2.3.1.4. Data Acquisition

The data was collected using a custom-written software in IGOR-PRO that was compatible with the MCC-CIO-DIO 48 data acquisition card.

2.3.2. Behavioural Training under head restrained conditions

2.3.2.1. Apparatus

The head constrained equipment was custom designed to deliver the air flow/odour as stimuli. A lickometer, a 10-channel olfactometer, stimulus delivery nozzle, a respiration/breathing sensor, a lick tube, and a PVC tube were all part of the setup (Figure 2-4A). The lickometer serves as an interface between all of the individual components that records and digitises lick and breath responses of the animal to various stimuli. The olfactometer was equipped with eleven mass flow controllers and electromagnetic solenoid valves enabling us to attain temporal precision during odour delivery. A splitter put in the olfactometer divided a clean air stream and routed it to various mass flow controllers. Air entered odour bottles via 10 small controllers while air from the main controller was regulated by solenoid valves and used as a dilution air stream. The dilution and odorized air streams were combined at the output through a T-tube before entering the odour delivery nozzle. The stimulation is administered to the nostril of the restrained animal by the nozzle. A preloading duration of 3.2 seconds was set before the odour presentation to guarantee that the odour plume reached a stable state (Figure 2-4B). After the preloading time, the exhaust was turned off allowing the stimulus to be delivered to the animal. This enabled us to obtain a homogeneous stimulus presentation. The equipment consisted of a PVC tube in which the animal was placed, and the head was restrained by screwing the head post onto a custom-built metallic plate attached to the tube. A lick tube was positioned near the animal's mouth to record the animal's lick state during the trial. On finishing the trial and completing the reward criteria the animal received the water reward from the lick tube. The sniffing behaviour of mice performing odour-based decision-making tasks under head-restrained condition was non-invasively monitored using a thermocouple-based pressure sensor placed near one nostril. The instrument was controlled by a LAB-View application that was custom written. During the head restrained training the inter trial interval (ITI) was kept constant at 13.2 s as this was the ideal inter trial period we observed while training animals in freely moving circumstances.

2.3.2.2. Task Habituation

Animals were subjected to task habituation training three to four days after the start of the water deprivation schedule. This was done to ensure that the animals become acclimated to the instrument and the procedures associated with it. Standard operant conditioning approaches were used to train the animals. This task habituation phase was completed in stages. Regardless of the animals' responses during the first stage, they got a water reward of 3 µl after the presentation of a 200 ms short tone. This was done for 20 trials, after which the delay between tone and reward was raised to 1 second (20 trials) and then 2 seconds (20 trials). This was done to elicit licking behaviour in water-deprived animals. Once the animals had learned to wait for the water, a stimulus was given to them. The stimulation lasted 2 seconds and came before the reward. The stimulus was also delivered to the animal during the next stages of the task habituation phase, and they had to learn to lick solely during the stimulus delivery duration. If animals only licked when a stimulus was present, they received a water reward after meeting the reward criteria (Phase 1 – Minimum 80 ms of licking and the lick is registered in at least 1/4 virtually segregated bins, Phase 2 – 120 ms; 2/4 bins and Phase 2.1 – 240 ms; 3/4 bins). If animals licked prior to the onset of the stimulus, the needed licking time to obtain the reward was increased from 100% to 200 percent in all of the above scenarios. All of the animals completed the pre-training in 4-5 sessions of 30-40 minutes each. When mice completed the training, they learned not to lick during the baseline, or time before the stimulus onset.

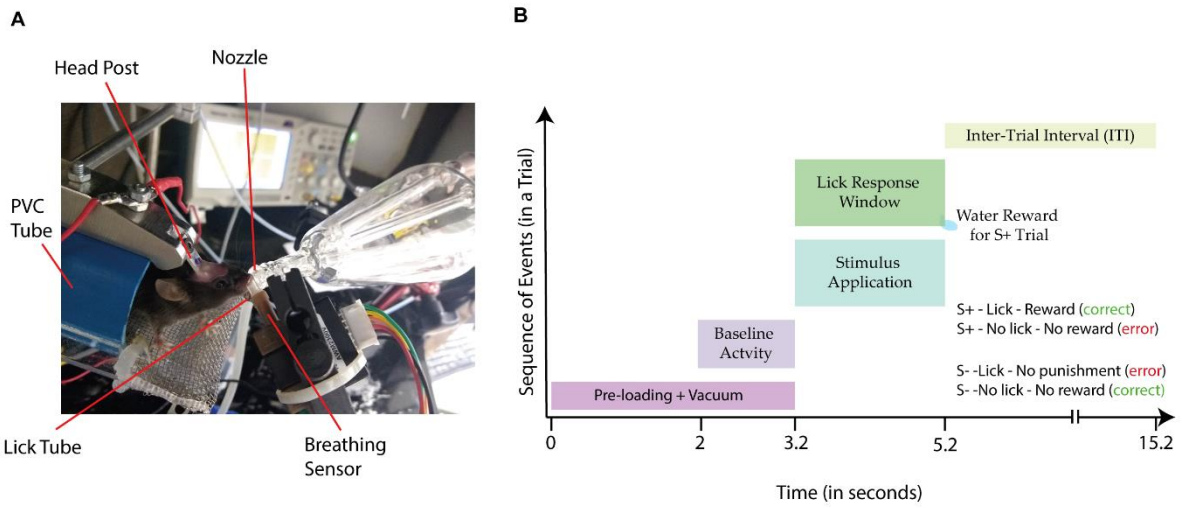

Figure 2-4 – Experimental setup to perform behavioural training under head restrained conditions

A) Animal engaged in behavioural training under head restrained condition.

B) Structure of an individual trial when animal is trained under head restrained conditions.

2.3.2.3. Discrimination training

Using a Go/No-Go behavioural paradigm (209,210), animals were trained to discriminate between two different stimuli, one of which was rewarded (S+) and the other was unrewarded (S-) (Figure 2-4B). The discrimination task was performed with a constant ITI of 13.2 seconds. The start of a trial causes one of the valves that controls the stimulus to open. The stimulus was deflected to the exhaust for the first 1 sec using a vacuum pump linked to the glass funnel. This was done, as with the freely moving setup, to eliminate the time difference between stimulus onset and its encounter with the animal. During this one sec the baseline licking was also assessed. The stimulus was presented for 2 seconds and animals had to respond within this time frame in order to get a reward (Figure 2-4B). The time required to lick in order to receive the reward for a S+ trial was determined by the baseline licking. If animals did not lick during the baseline, they were required to lick for a total of 240 ms in three (minimum 80 ms in each bin) of four 500 ms time bins. If the animals licked at the baseline, they had to lick twice as long during the stimulus presentation to earn the reward and register a correct trial. For an S- trial to be correct, the animal was not expected lick or even if they lick, it should not exceed a total of 80 ms, regardless of whether it displayed baseline licking or not. There was no punishment for the erroneous trials (Figure 2-4B).

Stimuli were administered to the animals in blocks of 20 trials. Each of these blocks contained ten S+ and ten S- trials. The S+ and S- trials within a block were pseudorandomized so that no more than two stimuli of the same reward contingency were delivered consecutively. The preference for a certain stimulus was avoided by counterbalancing the S+ and S- stimuli for a group of animals. Animals were sufficiently motivated to complete 200-300 trials each day. The frequency of licking was used to track the motivation of animals. When the animals were not motivated, they ceased licking for the rewarded trials.

2.3.2.4. Data Acquisition

Data was collected using a custom-written LAB View program that was compatible with a National Instruments (PCI 6703) data acquisition board.

2.4. Head post implantation for head restrained behavioural training

The animal was mounted in a PVC tube with a custom-made stainless-steel bracket during the head-restrained behavioural training. The PVC bracket is attached with a stainless-steel

head-post with a help of a screw. The head post is surgically implanted on top of the animal's skull. The detailed surgical procedure is described below:

1. An I.P. injection of a combination of Ketamine (50 g/g body weight) and Xylazine (10 g/g body weight) was used to anaesthetize animals. The toe pinch reflex was used to determine the level of anaesthesia. Once anesthetized, the animal was mounted on the stereotaxic instrument.
2. A local anaesthetic gel (Lignocaine hydrochloride) was applied to the skin over the skull.
3. Over the skull, an incision was made. Using a cotton swab, the region was thoroughly cleaned with artificial cerebrospinal fluid (ACSF) (125 mM NaCl, 5 mM KCl, 10 mM Glucose, 10 mM HEPES, 2 mM CaCl2, 2 mM MgSO4, in 1 L sterile Distilled water, pH = 7.4). The periosteum of the skull was carefully scraped off with a scalpel blade. The skull was allowed to airdry.
4. An etching agent was applied on the exposed skull for 15 seconds. The skull was thoroughly cleaned with the help of ACSF and the surface was air-dried.
5. A liquid primer was then applied to the skull using the applicator. The primer was allowed to airdry for 10 seconds before being exposed to the UV light for 30 seconds. The primer serves as an adhesive for the UV polymerizing cement to adhere to the bone.
6. A very thin layer of UV cure dental cement was spread on the skull and polymerized using UV light for 20 - 30 seconds.
7. The UV polymerizing cement was applied to the base of the head-post, which was then positioned upright on the cement layer on the skull. The two layers of cement were suitably fused, and the head-post location was adjusted appropriately. The cement was then polymerized for 40 to 50 seconds using UV light.
8. The remaining part of the skull was filled with cold cure acrylic dental cement. The mouse was removed from the stereotaxic device and placed in the home cage. The animal was given a recovery period of two days.

2.5. Measurement of breathing parameters

The breathing dynamics of the animal was continuously recorded during behavioural training using a non-invasive airflow pressure sensor placed near one of the nostrils. The sensor delivered real-time analogue signals to the lickometer linked breathing circuit with a resolution

of as good as 4 µs. Using a threshold function, the lickometer breathing circuit converted the raw analogue signals to a digital signal. The thresholding transformed the raw signal in binary values of 0 and 1 with 0-1 transition representing and inhalation and 1-0 transition representing an exhalation. On a trial-by-trial basis, these signals were continuously updated in the results file.

2.6. Different behavioural readouts

2.6.1. Learning Curves

We used a measure known as the learning curve to visualise the learning pace and its magnitude. The learning curve measures the change in percentage of correct responses as training progresses. Each point on the learning curve indicates the average accuracy of 100 trails [50 S+ and 50 S-] across all animals. When an animal first begins a discrimination task, its average accuracy lies at chance level (~50%), which increases as training progresses (Figure 2-5). Generally, after a few hundred trials, animals recognise the differences between rewarded and non-rewarded stimuli and begin to perform better, helping them in reaching an asymptotic phase of learning. When the experimental animals reach this stage, we consider the discrimination task as completed.

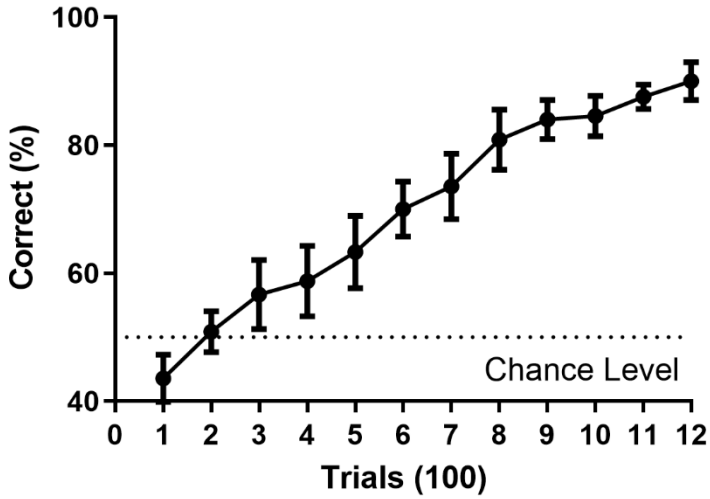

Figure 2-5 – Learning Curve for an airflow discrimination task

A typical learning curve while animal performed airflow discrimination training under head restrained conditions. The y-axis of the learning represents correct (%), which is the average accuracy across all animals across 100 trials (50 S+ and 50 S-). The x-axis represents progression of trials. In the initial phase of earning the performance of animals lies near to the chance level and with extent of learning

the performance increases and reaches an asymptotic phase. In this particular airflow pair animals performed 1200 trials (4 tasks, 300 trials in one task) and reached an average accuracy of more than 80%.

2.6.2. Discrimination time

The discrimination time was defined as the period following stimulus commencement when the animal's response to S+ and S- stimuli diverged significantly. To determine discrimination time in both head restrained and freely moving conditions, the licking behaviour of each mouse was tracked. The licking behaviour of animals was recorded with high temporal resolution and processed in 20 ms time bins for freely moving and 2 ms under head restrained conditions. With learning the licking behaviour evolved and was very different between initial and final phase of learning (Figure 2-6A and B). During the early stages of learning, when the animals were unable to distinguish between S+ and S- stimuli, they licked for both during the stimulus period. As a result, during the initial period of training, the lick reactions of animals to S+ and S- stimuli were similar (Figure 2-6A). However, once they learned to distinguish between two stimuli, they selectively licked for S+ stimuli and avoided licking for S- trials leading to a divergence in the lick responses between two (Figure 2-6B). The average difference between S+ and S- licking responses produced a sigmoidal curve, which was utilised to calculate the discrimination time. For all discrimination tasks, the discrimination time was measured over the last three hundred trials (unless specified in Figure legends). The lick responses were statistically compared between S+ (150 trials) and S- (150 trials) trials, providing a significance value (p-value) as a function of time. The discrimination time was determined by the last time the p-value fell below 0.05 (Figure 2-6C).

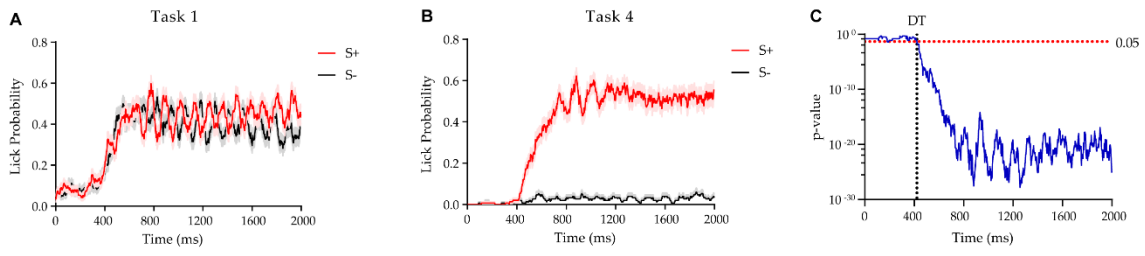

Figure 2-6 – Lick evolution with learning and discrimination time (DT) measurements from the licking behaviour of the mice towards S+ and S- stimuli

A) Representative lick responses of a single animal averaged over 300 trials (150 S+ and 150 S-) during task 1 i.e. initial phase of learning. Red traces represent average of S+ trials where as black traces

represent average of S- trials. The shaded region represents SEM. During task 1 as animal did not learn the discrimination task and performed with chance level, the lick responses for S+ and S- trials are similar.

B) Representative lick responses of a single animal averaged over 300 trials (150 S+ and 150 S-) during task 4 i.e. final phase of learning. Red traces represent average of S+ trials where as black traces represent average of S- trials. The shaded region represents SEM. During task 4 as animal performed with higher accuracy, the lick responses for S+ and S- trials diverged.

C) Statistical difference calculated between 150 S+ and 150 S- trials which yielded p-value as a function of time. The red dotted line represents the p-value level of 0.05. The black dotted line represents the time period when the curve crosses p-value of 0.05 for the last time. This time corresponds to the discrimination time (DT)

2.7. Measurement of airflow in nature

The airflow was measured from the potential rodent habitats that includes burrows, grocery shops, waste disposal sites, etc. with the help of a hotwired anemometer acquired from PCE instruments. The anemometer was kept inside the burrow or the location of potential habitat and average airflow rate for 100 seconds was measured. The measurements were done from multiple locations and were pooled together in order to compute the airflow range that rodents encounter in the nature.

2.8. PID measurements

PID measurements were taken to see if there were any consistent odorant cues within the airflow stimulus. This was done to ensure that when the animal receives the airflow stimulus, there are no odour cues connected with it that the animal may sense and use to make a decision. High intensity photons colliding with vaporised molecules of odours, if present, would cause a voltage shift in the photo ionic detector during PID measurements. PID measurements were performed for various airflows using a PID probe under similar conditions that was used for airflow detection and discrimination experiments. PID measurements were also performed on a set of odorants in order to demonstrate the difference that exists between airflow and odour generated PID patterns.

Table of Key resources

Odorant and chemicals		
Name	**Company**	**Identifier**
(+)-Octanol (≥99% purity)	Sigma-Aldrich	Cat#: 147982
(-)-Octanol (≥97% purity)	Sigma-Aldrich	Cat#: 147990
(+)-Carvone (≥96% purity)	Sigma-Aldrich	Cat#: 435759
(-)-Carvone (≥98% purity)	Sigma-Aldrich	Cat#: 124931
Iso-Amyl acetate (≥99% purity)	Sigma-Aldrich	Cat#: 306967
Ethyl butyrate (≥99% purity)	Sigma-Aldrich	Cat#: E15701
Hexanal (≥98% purity)	Sigma-Aldrich	Cat#: 115606
3- Pentanone (≥99% purity)	Sigma-Aldrich	Cat#: 345121
Zinc Sulphate Monohydrate (≥99% purity)	Sigma-Aldrich	Cat#: 96495
Methimazole	Sigma-Aldrich	M8506-25G
Mineral Oil	Fluka	Cat#: 161403
Thiopentanone Sodium (50-90 mg/kg I.P.)	Neon laboratories, India	Batch No: LU173B/2
Xylaxin (Xylazine, 10 mg/kg)	Indian Immunologicals Ltd.	
Aneket (Ketamine HCl, 50 mg/kg)	Neon laboratories, India	
Etching agent	Ivoclar Vivadent	Code No : 630210AN
UV polymerizing dental cement kit Tetric N-Ceram,	Ivoclar Vivadent	Sr No : 18-02303
Acrylic repair material DPI	RR Cold Cure	Batch No : P-4171
Hardware, Software and Data Analysis Tools		
Doric Miniaturized Fluorescence Microscope for Calcium Imaging	Doric Lenses Inc	https://www.doriclenses.com/

Custom software for freely moving behavioural experiments.	Wavemetrics	www.wavemetrics.com
Custom written scripts for data analysis.	Python	www.python.org
GraphPad Prism for data and statistical analysis	GraphPad Software Inc	https://www.graphpad.com/scientificsoftware/prism
Mass flow controllers	Pneucleus Technologies LLC, Hollis, NH	Item No: MCR-2A1B2002250N 050N-01 Item No: MDF-2A2B100200CN 020N-01
Solenoid Valves	ASCO Scientific	P/N: 401NC24830
Doric Imaging Cannula	Doric Lenses	Reduced footprint imaging cannula with 1.00 mm lens
Electromagnetic valves	SMC Pneumatic, Japan	Model No: SS073- X5V2555
Airflow thermocouple sensor	Honeywell	AWM2300V
Oscilloscopes	Tektronix	TBS-1072B-EDU and TBS-1052C
Hot Wire Anemometer	PCE Instruments	PCE-423-ICA

Table 2-1 – Table representing details of all the resources being used during the experiments

Chapter 3

Rodents use olfactory system to detect and discriminate ethologically relevant airflows

3.1. Introduction

3.1.1. Mechanosensation in the rodent olfactory system

In the natural environment, olfactory cues exist in the form of odour plumes which are associated with the airflows. Therefore, in addition to the signaling of chemical molecules, odour plumes can cause mechanosensation as well. The airflows transport odorant molecules from the source and facilitate their dispersion in space. Terrestrial animals sniff to sample the odorant molecules floating in turbulent airflows. Sniffing helps odour molecules to enter the nostrils and travel through the nasal cavity and bind to receptors on olfactory sensory neurons (OSNs) located on the epithelium. Apart from sensing the odour information, OSNs have been shown to respond to mechanical stimuli as well. The preliminary evidence of mechanosensation through olfactory system came from a novel study by Adrian wherein hedgehog's olfactory bulb neurons were demonstrated to elicit responses towards odourless air puffs (211). In addition, OB was shown to exhibit respiration coupled rhythmic activity in absence of any odour stimulus which was lost during naris occlusion (212–215). These discoveries were later supported by in vitro experiments, which revealed olfactory sensory neurons' responses towards mechanical stimulations (216). This study concluded that about 70% of the SO's OSNs and 50% of the MOE's OSNs are indeed mechanosensitive in nature. Further, OSN's responses towards mechanical stimuli were found to be dependent on stimulus strength and distance. While increasing the pressure of the ringers puff evoked higher amplitude, increasing the distance resulted in a decrease in response amplitude (216).

How does mechanical information processing happen through rodent olfactory system? This was hypothesized to be carried by the canonical G-protein coupled receptor pathway, because the expression of a non-functional mutant of this protein or disruption of the G-protein downstream pathway (deletion of adenyl cyclase III and cyclic gated nucleotide channel (cnga2) resulted in a null response from OSNs (216,217). Further, recordings from the cells with heterologous expression of olfactory receptors elicited calcium transients when stimulated with ringers puff, indicating that G-protein coupled receptors might be necessary and sufficient

to process mechanical information. As seen with odour stimuli, OSNs also transmit information associated with mechanical stimuli to OB. When airflow was employed as a mechanical stimulus to activate nasal cavity in artificially breathing double-tracheotomized rats, fMRI revealed broader and stimulus intensity dependent glomerular responses (14,15). Mechanosensation in OSNs is also shown to generate sniff-coupled oscillations and phase-coding in M/T cells (14). These observations support the hypothesis of olfactory receptors as a potential candidate responsible for processing the mechanical stimulation, whereas the behavioural relevance of mechanosensation through rodent olfactory system remains largely elusive.

3.1.2. Anemotaxic behaviour in rodents is mediated by whisker system

Active sensing, as opposed to passive sensing, is used to explore a new environment. Rodents use their whiskers to extract tactile information from their surroundings, similar to how humans use their hands and fingers to sense touch. During active sensing, the information about location, shape, size, and texture of the surrounding objects can be acquired as the animal explores the environment (167,218,219). Whiskers are hair-like structures embedded in skin follicles (165), and these follicles are densely packed with mechanoreceptors, which convert whisker based deflections into a neural code (169). Natural airflows can cause deflections at the base of whiskers, indicating that whiskers may be able to sense and process airflow information. In vitro studies have indeed shown that the whisker bends primarily in the direction of airflow and vibrates around a new average position at frequencies related to its resonant modes. The bending direction is unaffected by airflow speed or whisker geometry. In contrast, the bending magnitude increases strongly with airflow speed and the ratio of the whisker's arc length to base diameter. To a much lesser extent, the magnitude of the bending varies with the orientation of the intrinsic curvature of the whisker relative to the direction of airflow (169). These in vitro observations translate to behaviour as recent research suggests that whiskers may aid anemotaxis behaviour in rats. In a study in which rats were trained to locate an air source, the animals' performance declined significantly (~ 65% to 45%) when whiskers were removed (41). Despite the significant decrease in performance, the animals could still locate air sources with higher accuracy than chance levels (20%), indicating a possibility of another sensory system being involved in sensing and processing the airflows. Secondly, the airflows used for the localization test were significantly higher than those

observed in rodents' natural habitats, indicating the need for a robust method to investigate the sensory systems involved in airflow detection and discrimination behaviour.

As both olfactory and whisker systems are mechanosensitive and may be involved in airflow detection and discriminations, the primary goals of the experiments reported in this chapter are as follows:

1. To design and standardize an instrument for airflow detection and discrimination tasks.
2. To conduct experiments investigating if the olfactory system is primarily involved in airflow detection and discrimination behaviour.
3. If the olfactory system is involved in this behaviour:
    1. To investigate and compare sniffing strategies of animals while performing airflow and odour-based discrimination tasks.
    2. To determine whether olfactory sensory neurons and the olfactory bulb are essential for airflow detection and discrimination tasks.

3.2. Materials and Methods

Mice were trained on olfactory GNG behavioural paradigm under FM or HR conditions. The detailed methods for these behavioural paradigms are explained in material and methods chapter (section 2.3.1 and 2.3.2).

3.2.1. Animals used

All experiments in this chapter were conducted on C57BL6 J mice. Mice were obtained from Jackson Laboratories and were then bred and maintained in the National Facility for Gene Function in Health and Disease (NFGFHD, IISER Pune).

3.2.2. Measurement of airflow discrimination performance for various airflow pairs under different conditions

The learning accuracy and discrimination times (mentioned in section 2.6.1 and 2.6.2 of the materials and methods chapter) of animals were used as the key behavioural readouts to optimize the experimental paradigm.

The first set of mice (n = 5 mice) were trained under freely moving conditions and M1 mode of stimulus delivery (mentioned in section 2.3.1.1 of the materials and methods chapter) was used. The sequence of airflow pairs that used for this set are: 8 vs. 4 Litres per minute (LPM) (4s stimulus duration – 900 trials), 8 vs. 4 LPM (3s stimulus duration – 300 trials), 8 vs. 4 LPM (2s stimulus duration – 300 trials), 5 vs. 3 LPM (3s stimulus duration – 600 trials), 2 vs. 1 LPM (3s stimulus duration – 600 trials), 0.8 vs. 0.3 LPM (3s stimulus duration – 600 trials), 0.8 vs. 0.3 LPM (2s stimulus duration – 600 trials), and 0.3 vs. 0.3 LPM (2s stimulus duration – 600 trials).

The second set of mice (n = 7-8 mice) were used to elucidate the role of whiskers in airflow-based discrimination task. Animals were trained intermittently on mode M2 and M3 (mentioned in section 2.3.1.1 of the materials and methods chapter) of stimulus delivery in presence and absence of whiskers. The sequence of training for this set of animals is: 2 vs. 1 LPM (Mode M2, Whiskers Intact, 1200 trials), 2 vs. 1 LPM (Mode M3, Whiskers Intact, 600 trials), 2 vs. 1 LPM (Mode M3, Whiskers Deprived (WD), 300 trials), 2 vs. 1 LPM (Mode M2, WD, 300 trials), 1.5 vs. 0.75 LPM (Mode M2, WD, 600 trials), 1.5 vs. 0.75 LPM (Mode M3, WD, 300 trials), 0.6 vs. 0.3 LPM (Mode M3, WD, 900 trials), 0.6 vs. 0.3 LPM (Mode M2,

WD, 600 trials), 0.2 vs. 0.1 LPM (Mode M2, WD, 900 trials), 0.2 vs. 0.1 LPM (Mode M3, WD, 600 trials), 0.3 vs. 0.3 LPM (Mode M2, WD, 600 trials), and 0.3 vs. 0.3 LPM (Mode M3, WD, 600 trials).

Third set of animals (n = 9 mice underwent training under freely moving conditions (Mode M3) wherein the animals in this group were subjected to whisker plucking. The sequence of training for these animals is: 0.2 vs. 0.1 LPM (Whiskers intact, 1200 trials), and 0.2 vs 0.1 LPM (Whisker plucked, 600 trials).

Fourth set of animals (n = 5-8 mice) were trained to discriminate different airflow pairs under head restrained conditions. The breathing responses of these animals were simultaneously recorded when they were involved in the discrimination task. These animals learnt to discriminate different airflows in the sequence: 0.2 vs. 0.1 LPM (1200 trials), 0.6 vs 0.3 LPM (900 trials) and 0.4 vs 0.45 LPM (900 trials). Another set of animals (n = 6 mice) was also trained under head restrained conditions to discriminate between odours. The odour pair used was octanol (+)/octanol (-) 60-40 binary mixture [60% octanol (+) + 40% octanol (-) vs. 40% octanol (+) + 60% octanol (-)] (1200 trials).

Three groups of animals were used to delineate the role of olfactory sensory neurons in airflow detection and discriminations. Out of these groups, one group of animals received IP injections of methimazole (n = 10 mice), second group were administered intranasally with zinc sulphate solution (n = 8 mice) and third group (n = 14-15 mice) received PBS injections (half animals were given IP injections and for half of the animals vehicle solution was administered intranasally). The sequence of training for these three groups were: Before treatment: 0.6 vs. 0.3 LPM (1200 trials), 0.2 vs. 0.1 LPM (900 trials), and AA vs. EB (900 trials). After treatments: AA vs. EB (300 trials), 0.2 vs. 0.1 LPM (600 trials), and 0.6 vs. 0.3 LPM (600 trials).

Four different sets of animals were used to investigate whether OB is crucial for airflow detection and discrimination. The training schedule for these four groups were: Group 1 (n = 7-8 mice) – 0.6 vs. 0.3 LPM (1200 trials) – Bulbectomy – 0.6 vs. 0.3 LPM (600 trials), Group 2 (n = 6 mice) – 0.6 vs. 0.3 LPM (1200 trials) – Sham surgery – 0.6 vs. 0.3 LPM (600 trials), Group 3 (n = 5-8 mice) – 0.2 vs. 0.1 LPM (1200 trials) – Bulbectomy – 0.2 vs. 0.1 LPM (600 trials). Group 4 (n = 6 mice) – 0.2 vs. 0.1 LPM (1200 trials) – Sham surgery – 0.2 vs. 0.1 LPM (600 trials).

Three different sets of animals were trained to investigate whether airflow sensing via olfactory system follow Weber's law. The training schedule for these group of animals were: Group 1 (n = 8) - 0.1 vs. 0.15 LPM (1200 trials), 0.1 vs. 0.14 LPM (600 trials), 0.1 vs. 0.13 LPM (600 trials), 0.1 vs. 0.12 LPM (600 trials) and 0.1 vs. 0.11 LPM (600 trials). Group 2 (n = 8) - 0.2 vs. 0.25 LPM (1200 trials), 0.2 vs. 0.24 LPM (600 trials), 0.2 vs. 0.23 LPM (600 trials) and 0.2 vs. 0.22 LPM (600 trials). Group 3 (n = 8) - 0.3 vs. 0.36 LPM (1200 trials), 0.3 vs. 0.35 LPM (600 trials), 0.3 vs. 0.34 LPM (600 trials) and 0.3 vs. 0.33 LPM (600 trials).

3.2.3. Video recording of animals

The videos of the animals performing the airflow discrimination task were captured with a Redmi 4A smartphone at a resolution of 30 frames per second.

3.2.4. Breathing frequency calculation and histogram plotting

The breathing frequency was measured for each trial throughout the stimulus time as well as before, during, and after the decision-making window. Assuming the discriminating time is x ms different windows were defined as follow: Pre DT from 0-x to 0, During DT from 0 to 0+x, and Post DT from 13000-x to 13000. Onset of inhalation time points represented a point in the raster plot. A histogram with a bin resolution of 20 ms was used to depict the inhalation onset distribution across all trials and animals. Time of first inhalation after the onset of stimulus was considered as inhalation onset time. The area under the curve was determined using the trial wise histograms plotted for each animal. The AUC was computed just from the start of the stimulus to the discrimination time and was normalised with the maximum frequency. The sniffing peak latency was defined as the time corresponding to the mode of distribution of breath initiations. For analysis, custom built algorithms in Python were employed.

3.2.5. Surgical Procedures

3.2.5.1. Whisker Trimming

Animals were mildly anesthetized with isoflurane and whiskers were trimmed in a row wise fashion by using scissors. Whisker trimming was performed once a week on the animals

that required trimmed whiskers for all of the experiments. Animals that were on a water restriction schedule were given free water for two hours before and after the treatment.

3.2.5.2. Whisker Plucking

The process for whisker plucking was identical to that for whisker trimming. Instead of clipping the whiskers, tweezers were used to pluck them from the root.

3.2.5.3. Intranasal Zinc Sulphate injections

Animals were mildly anesthetized with isoflurane and were held vertically with their snout facing upwards. Using a micropipette, 25 µl of 5% zinc sulphate was infused into one of the nostrils. The animal was turned upside down immediately after the infusion to reduce the passage of zinc sulphate into the wind pipe or lungs. Before infusing the second nostril, the animals were given a two-hour recovery period. After infusing both nostrils, the animals were given a two-day recovery time with *ad libitum* access for food and water. Animals that were on a water restriction schedule were given free access to water for 12 hours before the treatment.

3.2.5.4. Methimazole injection

75 mg/kg of the methimazole dissolved in PBS was injected intraperitoneally (IP injection). Animals were given a two-day recovery period following injections. Animals on a water restriction schedule were given free access to water for 12 hours before the treatment.

3.2.5.5. Surgical aspiration of Olfactory Bulb (Bulbectomy)

The animals were anesthetized with a combination of ketamine and xylazine. The anaesthetized animal was then mounted on the stereotaxic instrument. An incision was performed on the skull over the olfactory bulb area, and the skull was completely cleaned. A 2.5 mm diameter window was formed over the olfactory bulb region via a tissue puncture. A 21 - G needle connected to a vacuum pump was used to aspirate the olfactory bulb. The skin was sutured back together, and the animal was given a two-week recovery time before continuing with the experiments. All of the steps were same for the animals that had sham surgery, except for the excision of the olfactory bulb.

3.2.6. Hematoxylin and eosin staining procedure

3.2.6.1. Nasal Cavity Dissection

The animals were first perfused with PBS and 4% paraformaldehyde. The animal was decapitated, and the head was properly cleaned in order to isolate the nasal cavity. Tissue was preserved overnight in 4% paraformaldehyde before being thoroughly cleaned. Tissue was then incubated in a 10% EDTA solution for a week to decalcify the bones surrounding the nasal cavity. After extracting the tissue from the EDTA solution, the nasal cavity was dissected by gently removing the surrounding bones.

3.2.6.2. Paraffinization of the cavity

1. The nasal cavity was then washed with 60% isopropanol (90 mins X 3 washes).
2. The nasal cavity was transferred to 80% isopropanol solution and was given two washes (45 mins X 2 washes).
3. To further dehydrate the tissue, nasal cavity was washed in 90% isopropanol solution (30 mins X 1 wash + 15 mins X 1 wash).
4. Nasal cavity was then transferred to xylene and three 15 mins washes were given.
5. Nasal cavity was transferred to pre melted paraffin wax and incubated overnight at 62 degrees Celsius in an oven.
6. Tissue was embedded in a wax block that was incubated at -20 °C overnight.

3.2.6.3. Microtome sectioning

1. Wax block having the nasal cavity was mounted on the microtome.
2. 5-8 µm sections were obtained and were transferred to the poly-L-lysine coated slides.

3.2.6.4. Deparaffinizing the tissue

1. The slides were incubated in a hybridization oven overnight at 62 °C.
2. The slides were incubated in xylene for 5 mins (2 times).
3. The slides were then kept in 100% ethanol for 3 mins followed by 90%, 70% and 50% ethanol for 3 mins each.
4. Slides were then placed in distilled water for 3 mins.

3.2.6.5. Staining protocol

1. The slides were removed from the water and left to air dry. A napkin was used to wipe away any excess water around the tissue .
2. Slides were placed on the rails of the humidifying chamber, and a drop of hematoxylin was added to the tissue.
3. The slides were left undisturbed for 15 minutes.
4. Excess hematoxylin stain was washed away with distilled water, and slides were rinsed under running water for 15 minutes.
5. The slides were then immersed in 1 percent HCl in 80 percent ethanol for 10 seconds.
6. A drop of eosin was added to each section.
7. After 30 seconds, the slides were transferred to 70% ethanol for 1 minute, then 90% ethanol for 1 minute, and finally 100% ethanol for 1 minute.
8. The slides were removed from ethanol and left to dry naturally.
9. After the slides had dried, they were washed twice with xylene (15 mins each). Following this, slides were removed.
10. Using a napkin, Xylene was wiped from the corners of the slides, and a drop of DPX medium was added to the sections before the slides dried completely.
11. The slides were mounted with a cover slip and edges of the cover slip was sealed.
12. The sections were then examined using a brightfield microscope.

3.2.7. Data Analysis and Statistical analysis

GraphPad Prism 9, Microsoft Excel, and Python were used for all statistical analyses in this chapter. The data is presented as Mean ± SEM. To determine p-values and test for statistical significance, we used the student's t-test, one-way and two-way ANOVA, and associated post-hoc tests.

3.3. Results

3.3.1. Rodents can detect and discriminate different airflow rates

In behavioural neuroscience, a robust behavioural assay with reliable high throughput readouts is necessary to examine a behaviour and explore its neural mechanisms. Therefore, we first modified our custom-built olfactometer and standardized the parameters to provide airflows as a stimulus to the animals in order to test them on an airflow-based discrimination task. To achieve that we trained a group of animals using a standard Go/No-Go paradigm using in custom built olfactometer. M1 mode (Materials and methods, section 2.2.1.1) of stimulus delivery was used during this experiment, since, in this mode, the stimulus is delivered onto the snout of the animal. This design was used with the rationale that animals may use both olfactory and whisker systems to sense the stimulus while airflow is delivered on the snout. M1 mode provides a platform to answer the critical question: Whether rodents can detect and discriminate airflows using either of the sensory systems? Furthermore, because this was the first time, we conducted the experiment using our in-house developed olfactometer, we needed to tune the instrument parameters in terms of stimulus strength and stimulus time as well. By training animals on different airflow pairs under different stimulus duration conditions helped us to simultaneously address both issues. As we could observe the deflection of plucked whiskers while airflow was provided in the range of 4-8 LPM, the animals were first trained to discriminate 8 vs. 4 LPM. Furthermore, while 2s is the standard stimulus duration used in olfactory behavioural tasks, we began with 4s as the stimulus duration for airflow-based tasks to ensure that animals had enough time to sample airflows and make decisions. During training, animals started at the chance level and progressed to the asymptotic phase of learning within 900 trials (Figure 3-1A), providing the first evidence that animals can detect and discriminate airflow rates. We then optimized the stimulus duration and tested the performance of these pre-learnt animals on 3s and 2s stimulus duration. Although there was an initial decrease in performance following the transition to an altered duration of the stimulus, the performance of the animals improved as the number of trials progressed (Figure 3-1A) and reached ~90% within 300 trials. The final accuracy (for last 300 trials) of the mice remained consistent across all three stimulus durations (Figure 3-1B, 4s – 93.80 ± 1.068 [Mean ± SEM], 3s – 91.20 ± 0.8602, and 2s – 89.80 ± 3.625; one-way repeated measures ANOVA, $F = 0.8460$, $p = 0.4642$). Moreover, the time required by animals to distinguish airflows was independent of stimulus duration, with non-significant differences in discrimination times (DTs) (Figure 3-1C, 4s – 480 ± 48.17 ms, 3s – 520 ± 75.63 ms, 2s – 540 ± 83.19 ms; one-way repeated measures

ANOVA, F = 0.2840, p = 0.7601). These results indicate that a 2s stimulus duration is sufficient for animals to make airflow-based decisions.

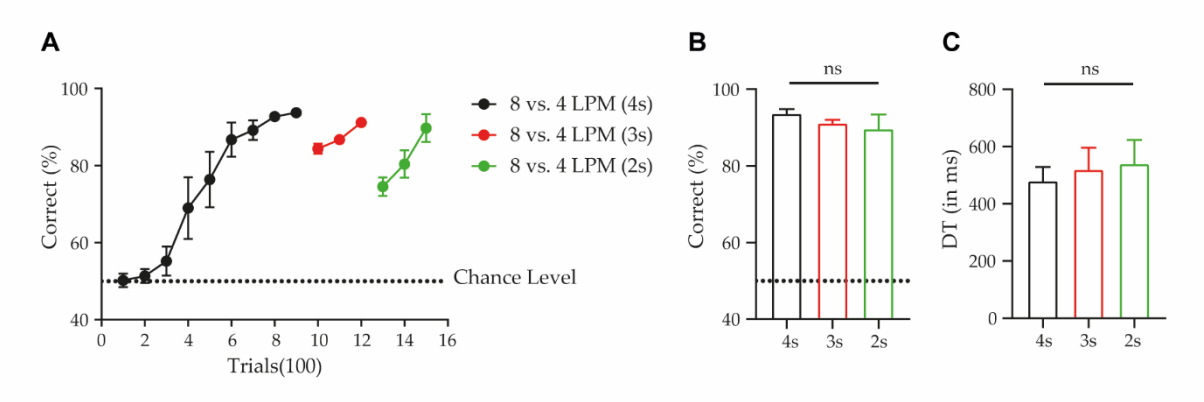

Figure 3-1 – Performance of animals across different stimulus durations while doing an 8 vs. 4 LPM airflow-based discrimination task

A) Airflow learning discrimination accuracies measured for 8 vs. 4 LPM at different stimulus durations. Each point on the learning curve represents the average of 100 trials across all animals (n = 5). This is represented by x-axis. The black dotted line at y= 50 represents the chance level.

B) Learning accuracies measured from last 300 trials for different stimulus durations and averaged across animals. The accuracies were found to be similar for all the three stimulus durations (one-way repeated measures ANOVA, F = 0.8460, p = 0.4642, n=5 animals).

C) Discrimination times measured from last 300 trials for different stimulus durations and averaged across animals. The DTs were found to be similar for all the three stimulus durations (one-way repeated measures ANOVA, F = 0.2840, p = 0.7601, n=5 animals).

As we performed these experiments with 8 vs. 4 LPM, which is a relatively high airflow rate than what rodents encounter in the nature, we next wanted to optimize the stimulus strength. To achieve this, we trained the animals on a series of airflow pairs with reducing stimulus strength and decreasing difference between the two stimuli (5 vs. 3 LPM, 2 vs. 1 LPM, 0.8 vs. 0.3 LPM, and 0.3 vs. 0.3 LPM). In addition to optimizing stimulus strength parameters, this strategy also enabled us to explore the mice' discrimination abilities towards varying airflows using their nose. The animals were first trained on 5 vs. 3 LPM with 3s as the stimulus duration. For this airflow pair, animals performed with greater than 85% accuracy in 600 trials (Figure 3-2A). The animals were then trained on 2 vs. 1 LPM and 0.8 vs. 0.3 LPM. For both of these airflow pairs animals reached asymptotic phase of learning within 600 trials (Figure 3-2A). The final accuracy of animals for the abovementioned airflow pairs remained more than

80 percent and the discrimination time lied in the range of 300-500 ms (Figure 3-2B and C, Accuracies: 5 vs. 3 LPM – 96.00 ± 1.449, 2 vs. 1 LPM – 93 ± 0.8944, 0.8 vs 0.3 LPM – 91.2 ± 1.114; DTs: 5 vs. 3 LPM – 354.4 ± 25.85, 2 vs. 1 LPM – 388.0 ± 32.20, 0.8 vs 0.3 LPM – 378.4 ± 29.98). We further investigated the performance of animals when they were subjected to a 0.5 LPM (0.8 vs. 0.3 LPM) stimulus difference and a 2s stimulus duration. Although there was a transient dip in accuracy when the animals switched from 3s to 2s, the animals performed at or above 85% within 600 trials (Figure 3-2A). The final accuracies and DTs of animals for 3s and 2s stimulus durations were similar (Figure 3-2B and C, Accuracies: 0.8 vs 0.3 LPM (3s) – 91.2 ± 0.4899, 0.8 vs 0.3 LPM (2s) – 89.2 ± 0.4899; two-tailed paired t-test, p =0.1543; DTs: 0.8 vs 0.3 LPM (3s) – 378.4 ± 29.98 ms, 0.8 vs 0.3 LPM (2s) – 372.0 ± 44.99 ms; two-tailed paired t-test, p =0.900), indicating that stimulus duration does not influence the performance. Therefore, we chose 2s as the ideal stimulus time for training the animals on the airflow detection and discrimination tasks. In addition, to rule out the possibility of animals learning any non-specific cues other than airflows, a control task (0.3 vs. 0.3 LPM) was done in which animals performed at the chance levels (Figure 3-2B). So far, our findings indicate that animals can detect and discriminate a wide range of airflows efficiently within a time range of 300-500 ms.

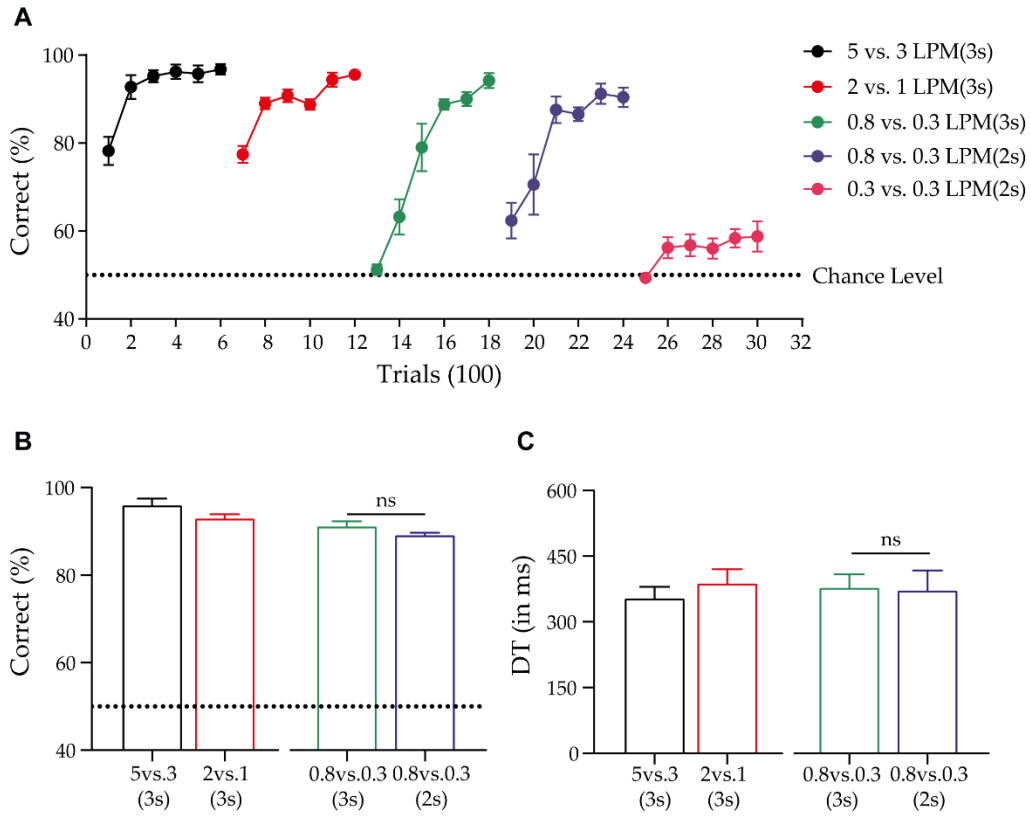

Figure 3-2 – Performance of animals across different airflow pairs

A) Training schedule and airflow discrimination accuracies measured for different airflow pairs. Airflow pairs used were 5 vs. 3 LPM (3s stimulus duration), 2 vs. 1 LPM (3s), 0.8 vs. 0.3 LPM (3s), 0.8 vs. 0.3 LPM (2s), 0.3 vs. 0.3 LPM (2s).
B) Learning accuracies measured from last 300 trials for different airflow pairs. The accuracies were found to be similar for 0.8 vs. 0.3 LPM (3s) and 0.8 vs. 0.3 LPM (2s) (two-tailed paired t-test, p =0.1543, n=5 animals).
C) DTs measured from last 300 trials for different airflow pairs. The DTs were found to be similar for 0.8 vs. 0.3 LPM (3s) and 0.8 vs. 0.3 LPM (2s) (two-tailed paired t-test, p =0.900, n=5 animals).

3.3.2. Airflow detection and discrimination is independent of the whisker system

Rodents rely on their whisker system to process airflow information as observed in their anemotaxis behaviour towards high airflow rates (41). In our experiments, we observed mice performing various airflow discriminations with high accuracy. Therefore, we wanted to study different sensory systems involved in accomplishing these discriminations. We used two alternative modes of stimulus delivery (M2 and M3; Materials and methods, section 2.2.1.1) that could supply airflow directly on the animals' whiskers either in a focused (M2 mode) or diffusive (M3 mode) manner. These two modes were employed to decouple the stimulation of whiskers and snout that M1 mode provided. First, we trained a set of animals on mode M2 on 2 vs. 1 LPM. Once the animals' accuracy reached >85% (in 1200 trials) (Figure 3-3A), we switched to M3 mode to see if different modes of whisker stimulation affected discrimination performance. Although there was an initial dip during the transition, the animals reached >85% accuracy within 600 trials (Figure 3-3A) and final performance (average of the last 300 trials) of animals in both settings was comparable (Figure 3-3B, M2 mode – 86.33 ± 0.7182, M3 mode – 89.21 ± 1.650, two-tailed paired t-test, p = 0.1348). Also, the mode switching had no effect on the DTs (Figure 3-3C, M2 mode – 440 ± 27.52, M3 mode – 480 ± 25.91, two-tailed paired t-test, p = 0.2141).

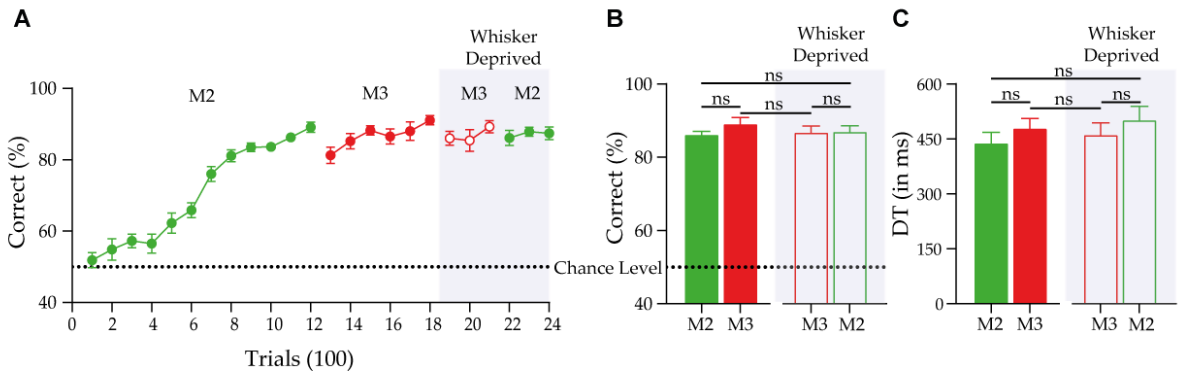

Figure 3-3 – Whisker deprivation does not affect the airflow discrimination abilities of mice

A) Training schedule and airflow discrimination accuracies measured for 2 vs. 1 LPM under different conditions. The conditions used were 2 vs. 1 LPM in M2 mode followed by M3 mode. The whiskers were then trimmed and animals' performance was tested on 2 vs. 1 LPM for M3 mode followed by M2 mode.

B) Learning accuracies measured from last 300 trials for 2 vs. 1 LPM across different conditions. The accuracies were found to be similar between M2 and M3 under whiskers intact condition (two-tailed paired t-test, p =0.1348, n=8 animals), between M2 and M2 before and after whisker deprivation (two-tailed paired t-test, p =0.6135, n=7 animals), between M3 and M3 before and after whisker deprivation (two-tailed paired t-test, p =0.3024, n=7 animals), between M3 and M2 after whisker deprivation (two-tailed paired t-test, p =0.9195, n=7 animals).

C) DTs measured from last 300 trials for 2 vs. 1 LPM across different conditions. The DTs were found to be similar between M2 and M3 under whiskers intact condition (two-tailed paired t-test, p =0.2141, n=8 animals), between M2 and M2 before and after whisker deprivation (two-tailed paired t-test, p =0.3589, n=7 animals), between M3 and M3 before and after whisker deprivation (two-tailed paired t-test, p =0.6627, n=7 animals), between M3 and M2 after whisker deprivation (two-tailed paired t-test, p =0.5166, n=7 animals).

We investigated the role of whiskers in the airflow discrimination behaviour by trimming the animals' whiskers and measuring their accuracy of performance and comparing with whisker-intact conditions. If whiskers were to play an important role in airflow discrimination behaviour, animals' performance would be affected by whisker deprivation. However, we didn't observe any difference in the performance accuracy or discrimination time taken by the animals for both modes (Figure 3-3B, Accuracies: M2 mode: whiskers intact (WI) - 86.33 ± 0.7182, whiskers deprived (WD) – 87.14 ± 1.438, two-tailed paired t-test, p = 0.6135, M3 mode: WI – 89.21 ± 1.650, WD – 86.90 ± 1.628, two-tailed paired t-test, p = 0.3024; Figure 3-3C, DT: M2 mode: whiskers intact (WI) - 440 ± 27.52 ms, whiskers deprived (WD) – 502.9

± 46.89 ms, two-tailed paired t-test, p = 0.3589, M3 mode: WI – 480 ± 25.91 ms, WD – 462.9 ± 30.99 ms, two-tailed paired t-test, p = 0.6627). These results prove that mice can detect and discriminate between airflows even in the absence of whiskers.

3.3.3. The intensity of the stimulus does not influence the airflow discriminating abilities of whisker-deprived animals

Given that removal of whiskers had no effect on mice' airflow detection and discrimination behaviour, we wanted to probe if there was any effect of stimulus strength on their performance accuracy under deprived conditions. To accomplish this, we trained these whisker deprived animals on series of airflow pairs, wherein the absolute strength of the stimuli as well as the difference between the stimuli in an airflow pair was gradually decreased. The training sequence contained flow pairs 1.5 vs. 0.75 LPM, 0.6 vs. 0.3 LPM, and 0.2 vs. 0.1 LPM. The animals were trained in both M2 and M3 modes intermittently. Even though the accuracy reduced during the shift in airflow, for all of the airflow pairs, the ultimate performance accuracies of the animals in both modes were more than 80% (Figure 3-4A). The performance of animals did not show any correlation with differences between the airflows of an airflow pair (Pearson correlation $R^2 = 0.53$). While the whiskers are trimmed, the nerve endings remain intact, and this may mediate the sensation of higher airflows. However, we did not notice any behavioural performance deficits, thus excluding any possible role of whiskers in the discrimination behaviour we observed.

We validated our early results by training another group of animals before and after whisker plucking on 0.2 vs. 0.1 LPM (airflow pair with minimum airflows and difference between them). Whisker plucking is another kind of whisker deprivation that causes significantly greater harm to nerve endings than whisker trimming. This experiment was conducted on M3 mode of stimulus delivery. Mode M3 was utilised for all subsequent experiments since it demonstrated significantly higher accuracies of animals on 0.2 vs. 0.1 LPM when compared to mode M2 (M3 – 86.52 ± 1.103, M2 – 80.00 ± 0.7015, two-tailed paired t-test, p = 0.0058). Prior whisker plucking, animals reached asymptotic phase of learning in 1200 trials (Figure 3-4B1). The whisker plucking had no effect on performance of animals, as they began performing with more than 80% accuracy immediately after the treatment (Figure 3-4B1). The final accuracies (Figure 3-4B2, Before– 84.96 ± 1.261, After – 84.71 ± 0.8578, two-tailed paired t-test, p = 0.7550) and DTs (Figure 3-4B3, Before – 593.3 ± 75.06 ms, After

– 655 ± 32.46 ms, two-tailed paired t-test, p = 0.6164) after whisker plucking were identical to those before plucking. These findings further strengthen the notion that whiskers are not involved in the airflow detection and discrimination behaviour we observed.

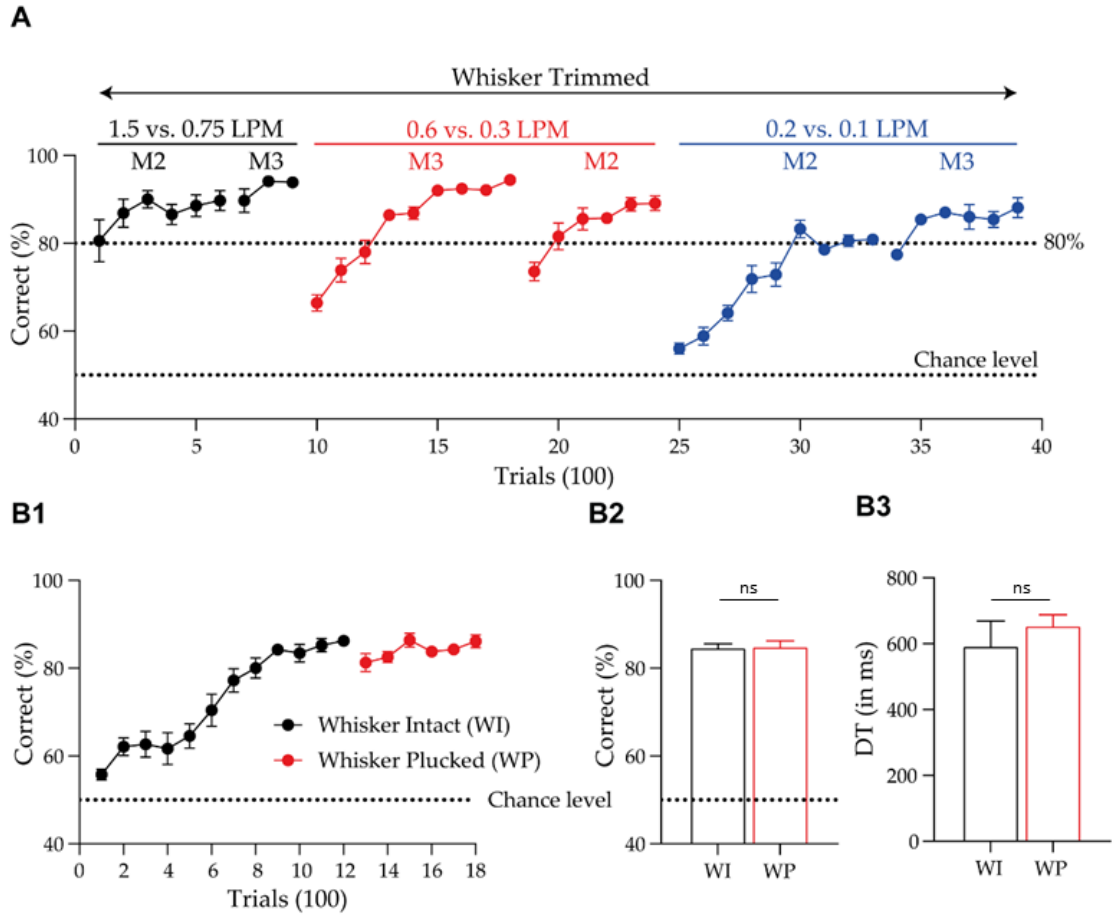

Figure 3-4 – Airflow detection and discrimination performance of animals in whisker deprived state across different airflow pairs

A) Training schedule and airflow discrimination accuracies measured for whisker trimmed animals. The airflow pairs used were 1.5 vs. 0.75 LPM, 0.6 vs. 0.3 LPM and 0.2 vs. 0.1 LPM. For all the airflow pairs the animals performed and reached more than 80% accuracy within 300-900 trials.

B) Performance of animals on 0.2 vs. 0.1 LPM before and after whisker plucking.

(B1) Learning curve before and after whisker plucking.

(B2) Final accuracies of animals (average of last 300 trials) before and after whisker plucking. The accuracies were found to be non-significant (two-tailed paired t-test, p = 0.7550, n = 9)

(B3) Final DTs of animals (average of last 300 trials) before and after whisker plucking. The DTs were found to be similar (two-tailed paired t-test, p = 0.6164, n = 9)

3.3.4. Rodents utilize their nose to sample airflows

Having observed the airflow detection and discriminations even in the absence of whiskers, we started to study the responsible sensory organ that contributes towards this behaviour. Can olfactory system be involved in processing airflow information in the absence of any odour molecules? The preliminary evidence of the olfactory system being used in such behaviour was provided by the detailed analysis of videos of animals recorded while they were involved in airflow-based discrimination task. The video analysis revealed that animals used their nose to sample the airflows in both M2 and M3 modes (Figure 3-5). When the animal received the stimulus after the trial began (t=0), it turned its head and inserted its nostrils into the stimulus delivery port (M2: t = 270 ms, M3: t = 230 ms). We observed animals sniffing the stimulus (Figure 3-5). After sampling the stimulus, animals determined whether it was a rewarded or unrewarded trial and licked correspondingly. After sampling the stimulus for sufficient amount of time, they repositioned their snout above the lick tube (M2: t = 630 ms, M3: t = 540 ms) and licked for a rewarded trial.

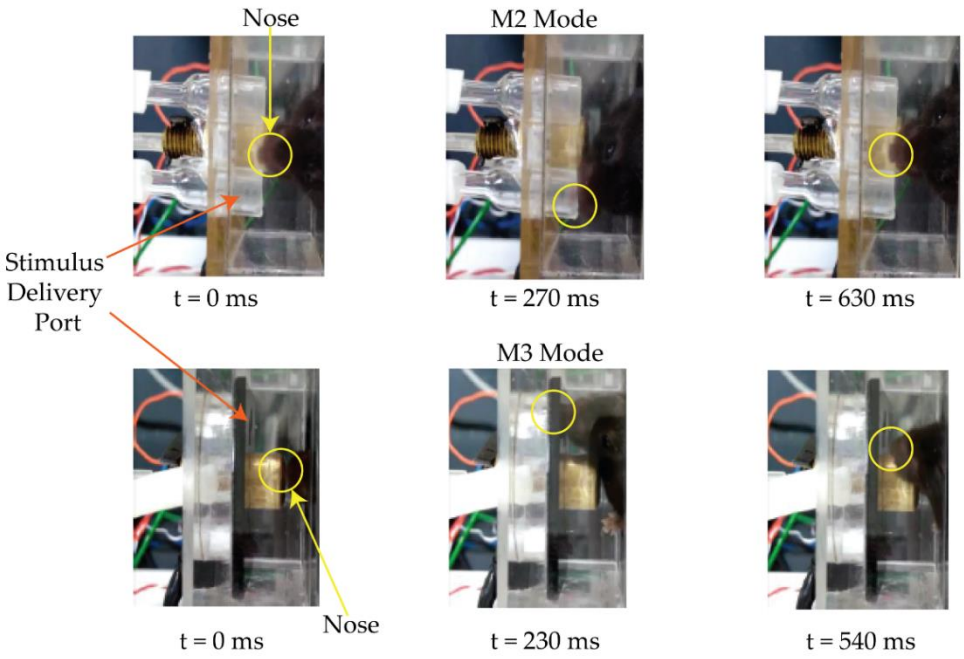

Figure 3-5 – Animals using their nose to sample the stimuli while performing airflow discrimination task

The top row depicts snapshots taken at different time points during a trial for M2 mode. The mouse inserts its nostril into the stimulus port at t= 270 ms, suggesting the use of the nose in sampling the stimulus. Bottom row depicts snapshots taken at different time points during a trial for M3 mode. In this mode also the mouse inserts its nostril into the stimulus port at t= 230 ms.

Since rodents were observed using their nose to make airflow-based decisions, it is important to determine whether there are any other sensory stimuli that they may use, specifically whether there is any odour stimulus within the airflows that animals may be using as a reliable decision-making cue. We trained these animals on a 0.3 vs. 0.3 LPM control task and observed that animals on both the modes (M2 and M3) performed with chance level accuracy (Figure 3-6A). In addition, the PID profiles for airflows were measured and compared to those for odours (Figure 3-6B1). In the case of airflow (0.3 LPM), there was no increase in PID voltage throughout the stimulus presentation, and the profile remained flat (Figure 3-6B1). In contrast, for hexanal-pentanone mix odour, the PID voltage surged as soon as the stimulus was provided and then returned to the baseline level following stimulus offset (Figure 3-6B1). Furthermore, the peak amplitudes for distinct airflows during the stimulus duration period were similar and did not correlate (Pearson correlation $R^2 = 0.2176$) and revealed any pattern (Linear regression $R^2 = 0.1572$) with the stimulus strength (Figure 3-6B2), confirming the absence of any odour stimuli that animals may utilise to efficiently discriminate different airflows.

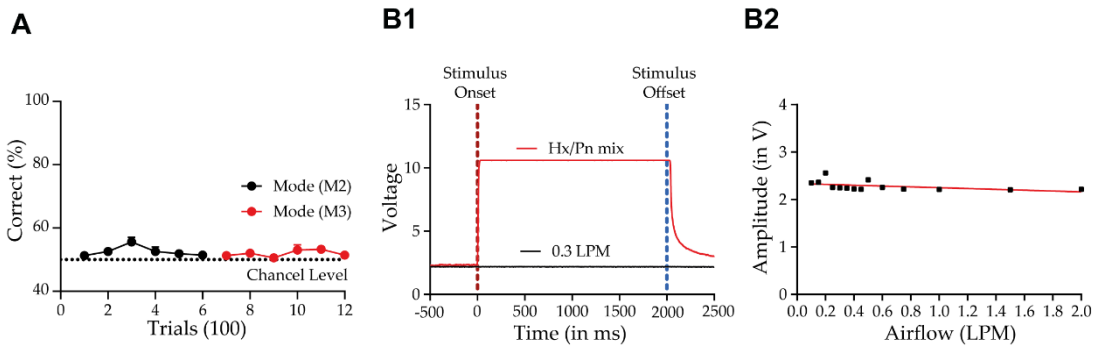

Figure 3-6 – Animals do not rely on sensory cues other than airflows to perform accurately in an airflow discrimination task

(A) Performance of animals on a control task of 0.3 vs. 0.3 LPM. Animals performed with chance level on both modes (M2 – black and M3 – red) of stimulus delivery.

(B) (B1) Comparison of PID profiles of airflow (0.3 LPM – black) and odour (Hexanal-pentanone mix – red). After stimulus onset the airflow PID profile remains flat however a sharp increase in the voltage for odour is present.

(B2) Curve representing change in amplitude voltage of different airflows with respect to their stimulus strength. The amplitude and stimulus strength exhibited no correlation (Pearson $R^2 = 2176$) as well as no linear trend (Linear Regression $R^2 = 1572$).

3.3.5. Sniffing frequency of animals increases during the decision-making window in airflow-based discrimination tasks

So far, our results show that the nose is engaged in airflow sampling. Since the nose is primarily known to sample odorants and employ sniffing as an exploratory strategy to sample them, we investigated the role of sniffing during airflow-based discrimination tasks. Before addressing this, we quantified a range of ethologically relevant airflows for rodents using a hot wire anemometer. The airflows were measured from potential rodent habitats including burrows, whole sale grocery stores, farms and waste-disposal areas. Our findings revealed an airflow distribution that ranged from 0.1 to 0.6 LPM (Figure 3-7). As a result, we limited the range of airflows for further discriminating training between this range.

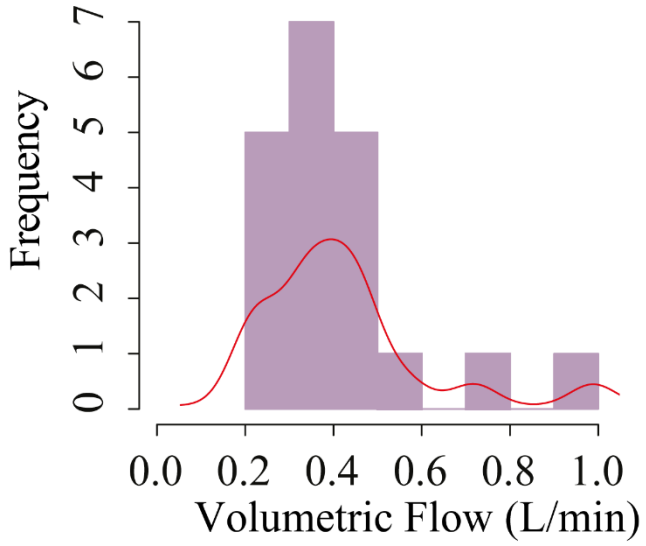

Figure 3-7 – Distribution of airflows in potential rodent habitats

The airflows in the potential rodent habitats were measured using a hot-wise anemometer. The airflows were observed to be in the range of 0.1 to 0.6 LPM, with 0.3 LPM as the most frequent.

Next, to assess the role of sniffing in sampling the airflows, we trained a naïve batch of animals to discriminate among airflow rates under head restrained conditions and recorded their sniff responses simultaneously. Mice were trained on a series of airflow pairs; 0.2 vs. 0.1 LPM (1200 trials), 0.6 vs 0.3 LPM (900 trials) and 0.4 vs 0.45 LPM (900 trials). Animals attained the asymptotic phase of learning for all airflow pairs, and their final accuracies (average of last 300 trials) were greater than 80%. The temporal sniffing patterns of animals throughout the asymptotic phase (final 300 trials) of the airflow-based discrimination tasks were quantified by raster plots, with each point in the raster representing the onset of an

inhalation. The sniffing profiles demonstrated that the inhalation count increases after the commencement of the airflow stimulus and remains high until the decision-making time (Figure 3-8A1, A2, and A3). We quantified this further by analysing sniffing frequencies (SF) throughout the stimulus duration as well as before, during, and after the decision-making phase.

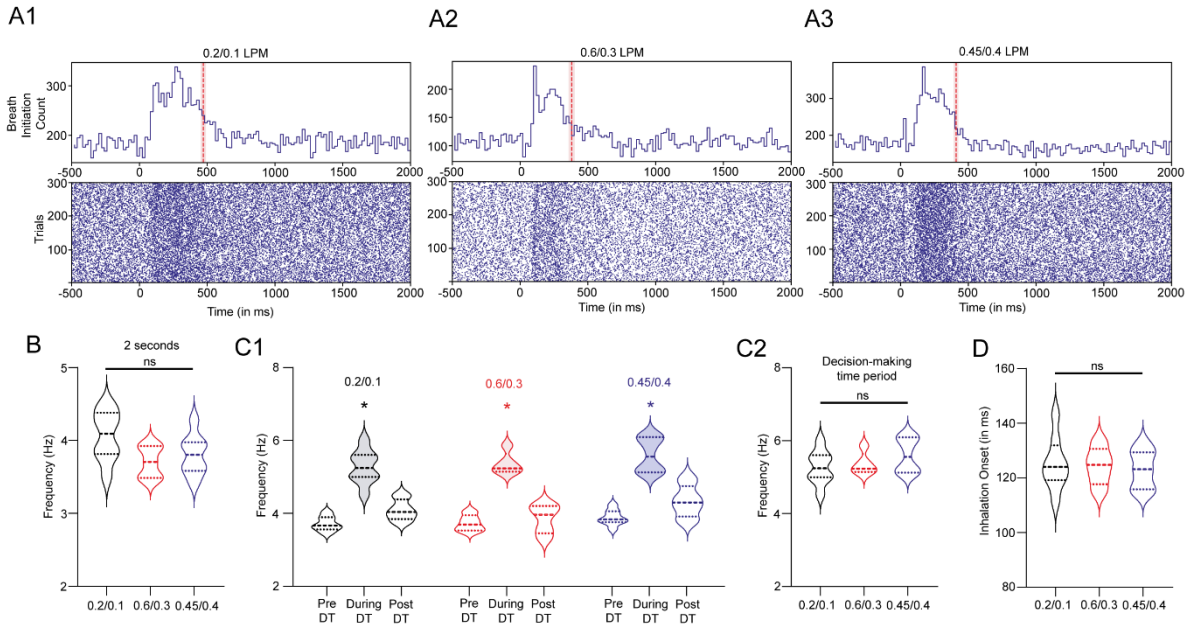

Figure 3-8 – Sampling behaviour of mice during airflow-based discrimination tasks

A) (A1, A2, A3) Raster plots and histogram representing inhalation onset for different airflow pairs. The y-axis in raster represents number of trials and x-axis represents the time. They are plotted using pooled data from all animals for last 300 trials in the asymptotic phase of training. The histogram represents frequency of inhalation onset (Breath Initiation count) along with time. The bin size of x-axis if 20 ms in the histogram. The red dotted line in the histogram represents discrimination time (DT) and the shaded red area represents SEM.

B) Violin plots showing sniffing frequencies of animals during 2 s stimulus period for different airflow pairs. Animals showed similar SFs for different airflow pairs (one-way repeated measures ANOVA, $F = 2.662$, $p = 0.0971$, $n = 5$-8).

C) (C1) Violin plots showing sniff frequencies of animals for before, during and post decision making period across different airflow pairs. Animals showed higher SF during decision making period across different airflow pairs (0.2 vs. 0.1 LPM; one-way repeated measures ANOVA, $F = 141.3$, $p < 0.0001$, $n = 8$, 0.6 vs. 0.3 LPM; one-way repeated measures ANOVA with Tukey's multiple comparison test, $F = 54.42$, $p = 0.0005$, $n = 5$, 0.45 vs. 0.4 LPM; one-way repeated measures ANOVA, $F = 139.5$, $p < 0.0001$, $n = 8$).

(C2) Violin plots showing sniff frequencies of animals during decision making period across different airflow pairs. The SFs of animals during decision making period were similar across different airflow pairs (one-way repeated measures ANOVA, F = 1.211, p = 0.3211, n = 5-8).

D) Violin plots showing onset of first inhalation during decision-making window across different airflow pairs. The inhalation onset of animals for different airflow pairs were non-significant (one-way repeated measures ANOVA, F = 0.1481, p = 0.8634, n = 5-8).

The SF calculated for a stimulus period of 2 seconds were similar for all three airflow pairs (Figure 3-8B, SF: 0.2 vs. 0.1 LPM – 4.060 ± 0.1213, 0.6 vs. 0.3 LPM – 3.705 ± 0.0979, 0.45 vs. 0.4 LPM – 3.803 ± 0.0980; one-way repeated measures ANOVA, F = 2.662, p = 0.0971). The similar phenotype was also observed while SF during the decision-making period was compared across airflow pairs (Figure 3-8C2, SF: 0.2 vs. 0.1 LPM – 5.268 ± 0.1635, 0.6 vs. 0.3 LPM – 5.358 ± 0.1357, 0.45 vs. 0.4 LPM – 5.596 ± 0.1634; one-way repeated measures ANOVA, F = 1.211, p = 0.3211). However, when SF were compared before (Pre DT), during (During DT), and after (Post DT) decision-making periods, the animals sniffed significantly higher during the decision-making time (Figure 3-8C1, SF: 0.2 vs. 0.1 LPM; Pre DT – 3.712 ± 0.0712, During DT – 5.268 ± 0.1635, Post DT – 4.092 ± 0.1018; one-way repeated measures ANOVA, F = 141.3, p < 0.0001, 0.6 vs. 0.3 LPM; Pre DT – 3.729 ± 0.0996, During DT – 5.358 ± 0.1357, Post DT – 3.885 ± 0.1762; one-way repeated measures ANOVA, F = 54.42, p = 0.0005, 0.45 vs. 0.4 LPM; Pre DT – 3.883 ± 0.0751, During DT – 5.596 ± 0.1634, Post DT – 4.330 ± 0.1549; one-way repeated measures ANOVA, F = 139.5, p < 0.0001). Additionally, we investigated whether sniffing behaviour changes with various airflows and discovered that the inhalation onset remained consistent regardless of airflows (Figure 3-8D, Inhalation onset: 0.2 vs. 0.1 LPM – 125.3 ± 3.424 ms, 0.6 vs. 0.3 LPM – 124.3 ± 3.124 ms, 0.45 vs. 0.4 LPM – 123.1 ± 2.465 ms; one-way repeated measures ANOVA, F = 0.1481, p = 0.8634). These results confirm the involvement of nose and modulation of sniffing behaviour during airflow discrimination, which was independent of airflow strengths.

3.3.6. Sniffing behaviour of animals refines with learning in airflow discrimination tasks

As we observed enhanced sniffing during decision-making in airflow discrimination tasks, we next studied the refinement of sniffing as a result of airflow discrimination learning. To accomplish this, we compared sniffing parameters from the same set of animals at 0.2 vs. 0.1 LPM during the first (first 300 trials) and final (last 300 trials) phases of learning. Because

this was the first airflow pair, only this was used for the analysis, as the effect of training can influence performance in the succeeding airflow pairs. The qualitative assessment of raster plots and histograms revealed possible refinement as training continued from the first to the last task (Figure 3-9A1 and A2). The raster plots and related histograms show that throughout the early stages of learning, breath initiation counts remained higher even after the peak and did not return to pre-stimulus levels. However, this was not the case in the final phase of learning. To confirm that animals had learned, learning accuracy and DT were used as readouts. In the initial phase of learning animals performed with chance level accuracy and their inability to discriminate airflows was also reflected in their higher DTs. While the average accuracy increased significantly in last task (87.21 ± 2.740) compared to first task (Figure 3-9B1, 57.04 ± 5.1000, two-tailed paired t-test, p = 0.0012), the discrimination time decreased as the animals learned to perform the task (Figure 3-8B2, First task – 1559 ± 216.7 ms, Last task – 475.8 ± 18.32 ms, two-tailed paired t-test, p = 0.0013).

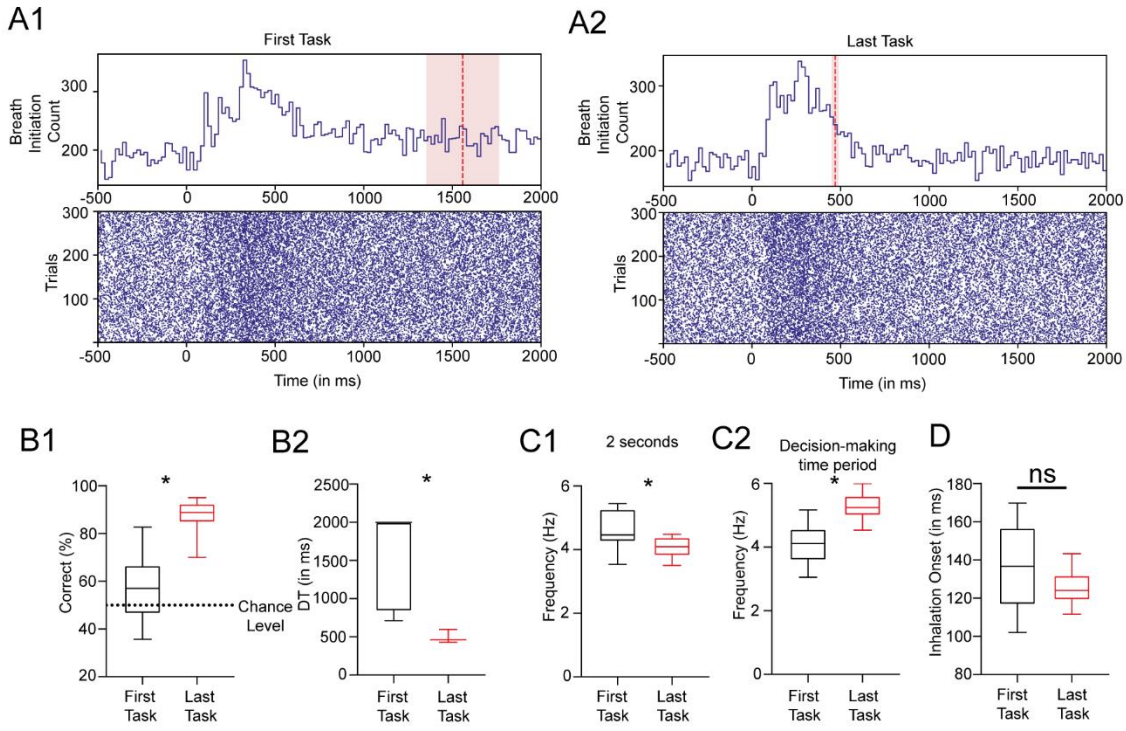

Figure 3-9 – Refinement of sampling behaviour of animals during airflow-based discrimination learning

A) (A1, A2) Raster plots and histogram representing inhalation onset during first and last task while animals were trained to discriminate 0.2 vs. 0.1 LPM.

B) (B1) Box plots showing accuracies of animals during first and last task of the training. The accuracy of animals was significantly higher for last task (two-tailed paired t-test, p = 0.0012, n = 8).

(B2) Box plots showing DTs of animals during first and last task of the training. The DT of animals was significantly lower for the last task (two-tailed paired t-test, p = 0.0013, n = 8).

C) (C1) Box plots showing SF of animals during 2s stimulus duration for first and last task of the training. The SF of animals was significantly lower for the last task (two-tailed paired t-test, p = 0.0157, n = 8).
(C2) Box plots showing SF of animals during decision-making window for first and last task of the training. The SF of animals during the decision-making window was significantly higher for the last task (two-tailed paired t-test, p = 0.0009, n = 8).

D) Box plots showing onset of first inhalation during decision-making window for first and last task of the training. The inhalation onset for first and last task was similar (two-tailed paired t-test, p = 0.1955, n = 8).

The sniff frequencies (SF) of animals was assessed during the stimulus duration and the decision-making window and compared between learning phases. While SF during stimulus duration decreased from first (4.603 ± 0.2248) to last phase (Figure 3-9C1, 4.060 ± 0.1213, two-tailed paired t-test, p = 0.0157), SF during decision-making window ensued a contrasting effect i.e. SF during decision making period increases with learning (Figure 3-9C2, First task – 4.098 ± 0.2317, Last task – 5.268 ± 0.1635, two-tailed paired t-test, p = 0.0009). We also examined whether an improvement in performance is associated to the commencement of the first inhalation and observed that the onset of the first inhalation is independent of learning (Figure 3-9D, First task – 136.3 ± 8.131 ms, Last task – 125.3 ± 3.424 ms, two-tailed paired t-test, p = 0.1955). Our findings provide conclusive evidence of refinement in sniffing behaviour as animals learn to perform an air-flow-based discrimination task.

3.3.7. Sniffing frequencies of animals during the decision-making period are independent of reward contingencies associated with the stimulus

Further, we investigated if the reward contingency linked with the stimulus influenced the sampling patterns, as sniffing activity is known to alter in anticipation of stimulus and reward administration (220). By pooling the data from all the airflow pairs while animals reached asymptotic phase of learning (last 300 trials > 80% accuracy), the sniffing frequencies (SF) for S+ and S- trials were calculated. The SF calculated for overall stimulus duration was higher in S+ airflow trials than in S- ones (Figure 3-10B1, S+ - 4.372 ± 0.1257, S- - 3.797 ± 0.1425, two-tailed paired t-test, p < 0.0001). In contrast, during the decision-making period, S+ and S- trials showed similar frequencies (Figure 3-10B2, S+ - 5.317 ± 0.1228, S- - 5.297 ±

0.1202, two-tailed paired t-test, p = 0.8663). Regardless of the reward linkage, mice learned to increase their breathing frequency throughout the decision-making process for both airflows (Figure 3-10A, C1, and C2, S+: Pre DT – 3.787 ± 0.0533, During DT – 5.409 ± 0.1046, Post DT – 4.143 ± 0.1090, one-way repeated measures ANOVA with Tukey's multiple comparison test, F = 84.92, p < 0.0001, S-: Pre DT – 3.776 ± 0.0663, During DT – 5.415 ± 0.1263, Post DT – 4.097 ± 0.1133, one-way repeated measures ANOVA with Tukey's multiple comparison test, F = 68.19, p < 0.0001). Although the SF in the post-decision-making period remained significantly greater than in the pre-decision-making period for S+ trials (Figure 3-10C1), it was comparable for S- trials (Figure 3-10C2). Once the animal makes a decision in a S+ trial, the lick probability of the animals increases in order to meet the reward criterion and receive the reward. Because licking, breathing, and whisking behaviour are linked to orofacial senses (202), an increase in lick frequency post decision-making for a S+ trial may also lead to an increase in SF, explaining why S+ trials had greater post decision making frequency as well as overall SF during 2s stimulus duration.

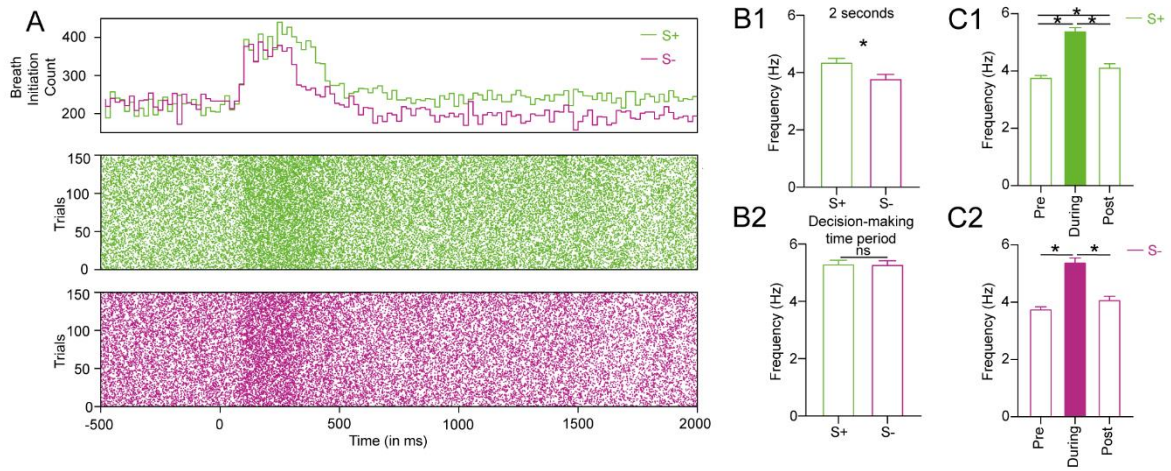

Figure 3-10 – Sampling behaviour of animals for S+ and S- trials pooled across airflow pairs

A) Raster plots and histogram representing inhalation onset for S+ and S- trials pooled across all airflow pairs.

B) (B1) Bar graphs representing sniff frequencies of animals for S+ and S- trials during 2s stimulus duration. The SFs of animals for S+ trials were significantly higher (two-tailed paired t-test, p < 0.0001, n = 5-8 mice).

(B2) Bar graphs representing sniff frequencies of animals for S+ and S- trials during decision-making window. The SFs of animals for S+ and S- trials were similar (two-tailed paired t-test, p = 0.8663, n = 5-8 mice).

C) (C1) Bar graphs representing sniff frequencies of animals for S+ trials for pre, during and post decision-making period. The SFs of animals during the decision-making period were higher (one-way repeated measures ANOVA with Tukey's multiple comparison test, $F = 84.92$, $p < 0.0001$, $n = 5\text{-}8$).

(C2) Bar graphs representing sniff frequencies of animals for S- trials for pre, during and post decision-making period. The SFs of animals during the decision-making period were higher (one-way repeated measures ANOVA with Tukey's multiple comparison test, $F = 68.19$, $p < 0.0001$, $n = 5\text{-}8$).

3.3.8. Sampling strategies of animals differ between airflows and odours

Rodents are known to use their noses primarily to sniff odorants and make sense of their olfactory surroundings. Given that they can employ sniffing to sample airflows devoid of odour molecules, the next critical question was whether sampling behaviour differ between physical (airflow) and chemical (odour) stimuli. We trained a new group of animals on an odour-based discrimination task in which they had to distinguish between a binary mixture of enantiomers (Octanol + vs. Octanol -). Once the animals performed with >80 percent accuracy, we quantified various sniffing parameters and compared with the sniffing parameters of animals that learned to discriminate airflows.

Mice showed distinct temporal patterns of breathing during airflow and odour discrimination behaviour (Figure 3-11A1 and A2). Sniffing of animals increased for both airflows and odours during the decision-making window, but the sniffing frequencies for odours were significantly greater than that for airflows (Figure 3-11B, SF: airflows – 5.268 ± 0.1635, odours – 5.925 ± 0.2156, two-tailed unpaired t-test, $p = 0.0291$). Furthermore, histograms revealed that, in comparison to odours, the animals displayed enhanced sniffing for longer durations (Figure 3-11A1 and A2). This was validated by quantifying the area under the curve (AUC) for both groups during the decision-making time, as it can be used as a measure to quantify sniffing modulations in a breath raster plot. AUC was calculated on trial to trial basis and was averaged across animals. The average AUC for airflows was noticeably higher than that for odours (Figure 3-11C, AUC: airflows – 339.1 ± 17.43, odours – 137.0 ± 11.65, two-tailed unpaired t-test, $p < 0.0001$). Apart from the broader responses, the difference between inhalation peak latency and discrimination time (DT-peak latency) for airflows was greater, implying that animals need more time to make airflow-based decisions at optimal sniff frequencies than odorants (Figure 3-11D, airflows – 164.3 ± 26.35 ms, odours – 30.67 ± 9.262 ms, two-tailed unpaired t-test, $p = 0.0012$).

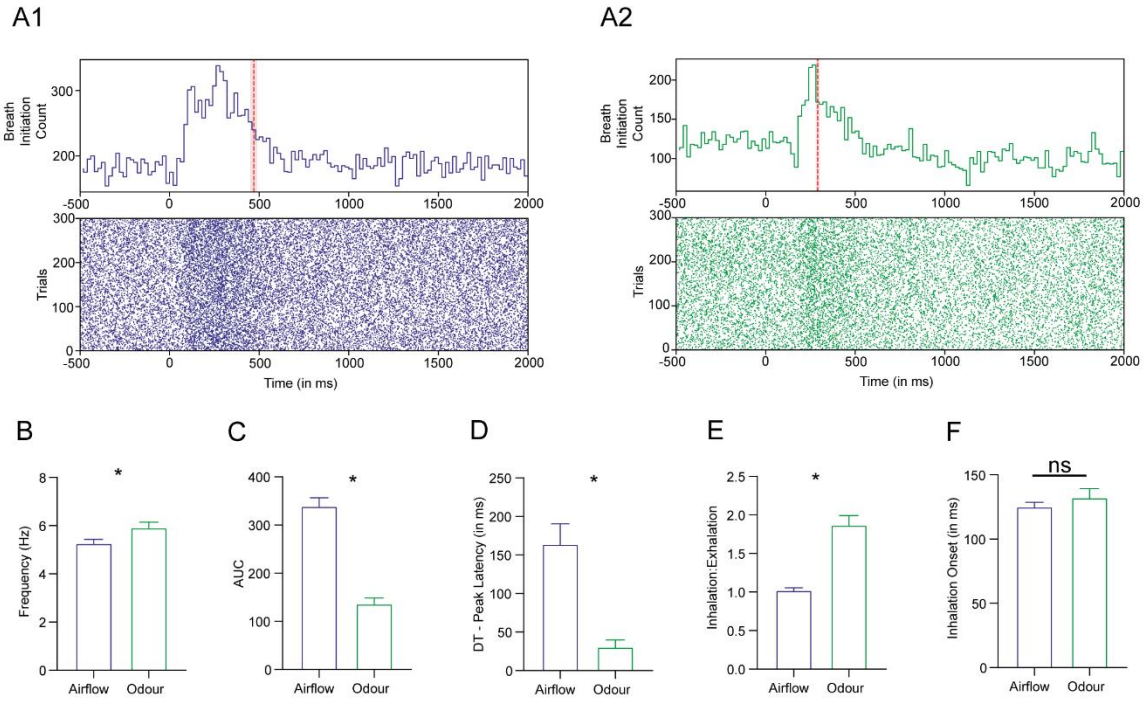

Figure 3-11 – Sampling behaviour of animals for airflow and odour-based discrimination tasks

A) (A1, A2) Raster plots and histogram representing inhalation onset for airflow (blue) and odour-based (green) discrimination pooled across animals in the last phase of learning (last 300 trials).

B) Bar graphs representing sniff frequencies of animals for airflow and odour trials during decision making period. The SFs of animals for odours were significantly higher (two-tailed unpaired t-test, $p = 0.0291$, $n_{airflow} = 8$, $n_{odours} = 6$).

C) Bar graphs representing area under the curve (AUC) for airflow and odour trials during decision making period. The AUC is calculated for sniff histograms from individual animals and averaged. The AUC for airflows was significantly higher (two-tailed unpaired t-test, $p < 0.0001$, $n_{airflow} = 8$, $n_{odours} = 6$).

D) Bar graphs representing difference in the discrimination time (DT) and Peak latency for airflow and odour trials during decision making period. The difference is calculated for individual animals and averaged. The difference was significantly higher for airflows (two-tailed unpaired t-test, $p = 0.0012$, $n_{airflow} = 8$, $n_{odours} = 6$).

E) Bar graphs representing ratio of time spent in inhalation to that of the time spent in exhalation for airflow and odour trials during decision making period. The ratio of inhalation to exhalation time was significantly lower for airflows (two-tailed unpaired t-test, $p < 0.0001$, $n_{airflow} = 8$, $n_{odours} = 6$).

F) Bar graphs representing onset of first inhalation for airflow and odour trials during decision making period. Animals showed similar inhalation onset for airflows and odours (two-tailed unpaired t-test, $p = 0.3419$, $n_{airflow} = 8$, $n_{odours} = 6$).

Further, to understand sampling behaviour in detail, we also analysed the inhalation-exhalation dynamics of animals. Odours showed a higher inhalation to exhalation time ratio than airflows (Figure 3-11E, airflows – 1.024 ± 0.0304, odours – 1.871 ± 0.1229, two-tailed unpaired t-test, $p < 0.0001$), suggesting that for odours, the time animals spent inhaling versus exhaling increased following the commencement of the stimulus, whereas for airflows, the time spent in both phases was the same. Despite changes in several sniff parameters, the time when first inhalation occurs remained same for odours and airflows (Figure 3-11F, Inhalation Onset: airflows – 125.3 ± 3.424 ms, odours – 132.4 ± 6.972 ms, two-tailed unpaired t-test, $p = 0.3419$), implying that first inhalation happens independently of stimulus characteristics and the temporal dynamics of breathing profile evolves depending on the kind of stimulus. Together, these results show that for airflows and odours, animals employ distinct sampling measures, indicating that they use different sniffing strategies to gather mechanical and chemical sensory information.

3.3.9. Airflow detection and discrimination behaviour is mediated by olfactory sensory neurons (OSNs)

So far, we have established that rodents employ sniffing, a sampling approach linked with the olfactory system, to sample airflows, and that sniff strategies differ depending on the airflow and odour stimuli. We then wanted to probe if airflow information is processed by olfactory sensory neurons (OSNs). To accomplish this, we quantified behavioural readouts before and after modifying the OSN activity. First, three different groups of animals were trained on airflow pairs. Once they began to perform with high accuracy (>80 %), these animals were subjected to various OSN ablation treatments before being tested on the previously learned airflow pairs. OSN ablation was achieved by using intranasal zinc sulphate injections and IP methimazole injections. Both of these treatments has been shown to induce anosmia in animals (221,222). After two days of injections, we also observed that the OSN layer was disrupted, with the thickness of the OSN layer reduced by approximately 60% (Figure 3-12A and B, Width of olfactory epithelium: Vehicle – 49.95 ± 1.110, Methimazole – 18.24 ± 1.035,

$ZnSO_4$ – 17.41 ± 0.7997, one-way ANOVA with Tukey's multiple comparison test, F = 354.2, p < 0.0001) .

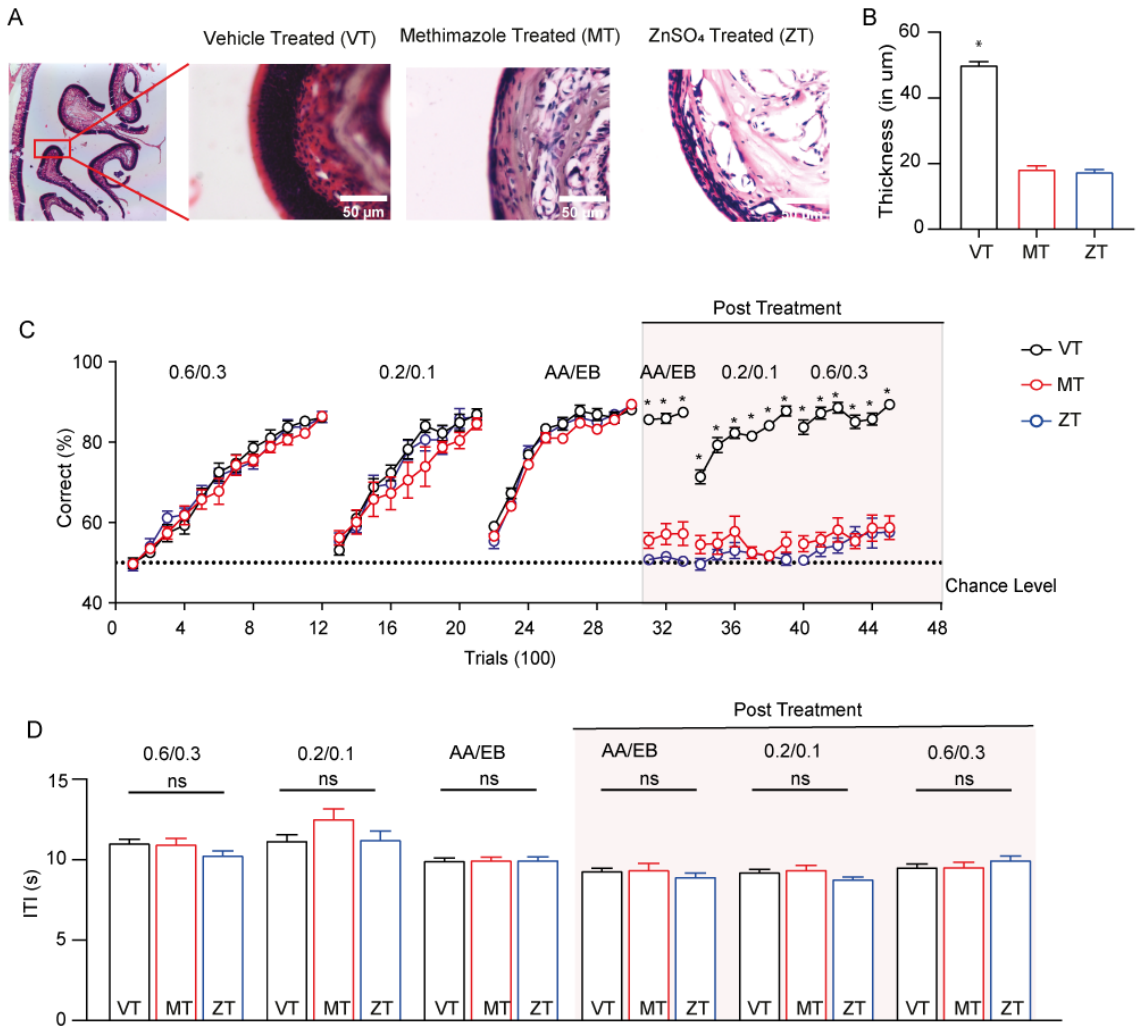

Figure 3-12 – OSNs mediate airflow detection and discriminations

A) Images showing Hematoxylin and Eosin stained section of nasal turbinates under different treatment conditions.

B) Thickness of epithelium measured across vehicle, methimazole and zinc sulphate administered animals after two days of the treatment. Epithelium thickness for vehicle (VT: Vehicle Treated) was significantly higher as compared to the width of epithelium in methimazole (MT) and zinc sulphate (ZT) treated animals (one-way ANOVA, F = 354.2, p<0.0001, n =2 mice for all groups, N = 50 region of interests from 6 sections from each mice).

C) Learning curve representing discriminating accuracies of animals for different airflow and odour pairs before and after the treatment. The learning accuracies of animals that underwent ZT and MT

were significantly lower to that of the control group. Statistical comparison across different groups for each airflow or odour pair is measured by using two-way ANOVA with Tukey's multiple comparison. * are used when $p<0.05$. n_{VT} = 14-15, n_{MT} = 10, n_{ZT} = 8)

D) Bar graphs representing inter trial interval (ITI) of animals, which is used as a readout for motivation levels. The ITI is compared for animals across different groups across different airflow and odour pairs under different OSN ablation treatments. The ITI of all animals throughout the training remained in the range of 9-11 s. Statistical significance was measured using one-way ANOVA with Tukey's multiple comparison and p-value of >0.05 was observed across different groups for different airflow and odour pairs.

To begin, we trained three groups (zinc sulphate, methimazole, vehicle treatment groups: referred as ZT, MT and VT respectively) of animals to first discriminate 0.6 vs. 0.3 LPM. Once the animals reached the asymptotic phase of learning we further trained the animals on 0.2 vs. 0.1 LPM. In addition, the animals were also trained on a monomolecular odour-based discrimination task (amyl acetate (AA) vs. ethyl butyrate (EB)). All three groups of animals were able to differentiate both airflows and odours with similar accuracy, eliminating the chances of inter-group variability accounting for the differences in the behavioural readouts (Figure 3-12C, two-way ANOVA: 0.6 vs. 0.3 LPM; $F(22,360) = 0.5380$, $p = 0.9581$, 0.2 vs. 0.1 LPM; $F(16,240) = 1.183$, $p = 0.2820$, AA vs. EB; $F(16,232) = 1.044$, $p = 0.4114$). Following this, one group of animals received an intranasal injection of 5% zinc sulphate, second group received methimazole treatment and third control group of animals was injected with the vehicle (half animals with intranasal PBS treatment and half with IP injection of PBS). Post injections, the performance of animals infused with zinc sulphate and methimazole in the odour discrimination task decreased to chance level, showing that the treatments were effective. However, animals treated with vehicle showed no impairments in odour discrimination (Figure 3-12C, two-way ANOVA with Tukey's multiple comparison test: * indicates p-value of <0.05). After the odour discrimination task, the performance of animals was assessed on previously learnt airflow pairs. When compared to their pre-treatment accuracy and performance of vehicle-treated animals, these animals revealed a deficit in airflow discrimination behaviour (Figure 3-12C, two-way ANOVA with Tukey's multiple comparison test: * indicates p-value of <0.05). Because PBS-treated animals showed no performance deficit, but methimazole and zinc sulphate-treated animals could not perform better than chance level even after 600 trials, these findings prove that, in addition to odour-based information processing, OSNs are also required to process ethologically relevant airflow information. The

performance of animals was unaffected by any potential changes in the motivation level of animals associated with treatments, because the inter trial interval (ITI), which is a readout for motivation, remained consistent throughout training (Figure 3-12D, one-way ANOVA, $p > 0.05$ across all conditions).

3.3.10. The olfactory bulb (OB) is essential for processing airflow information

The olfactory bulb (OB) is a pre-cortical region in the brain that receives odour-based information from the OSNs, refines it, and transmits it to higher cortical regions. Since OSNs are implicated in mediating airflow-based discriminating, the next critical question is whether OB receives and processes airflow information from the OSNs to carry out airflow detection and discrimination behaviour. To do this, we quantified behavioural readouts before and after bulbectomy. We began by training two groups of animals on an airflow-based discrimination task and allowing them to get to the asymptotic phase of learning. Following that, one set of mice had bulbectomy (surgical aspiration of the OB), while the other group underwent sham surgery (control group). We assessed their performance on the previously learned airflow pair after these surgical manipulations. We conducted two independent experiments for two airflow pairs using distinct sets of animals, i.e., two groups of animals were trained for each airflow pair (bulbectomy and sham surgery group). The airflow pairs examined for the role of OB were 0.3 vs. 0.6 and 0.2 vs. 0.1 LPM, which were identical to those employed in the OSN experiment.

Within 1200 trials, the animals performed with greater than 80% accuracy for both airflow pairs. Both the experimental and control groups had equal learning rates for 0.6 vs. 0.3 LPM (Figure 3-13A1, two-way ANOVA, $F(11,132) = 1.282$, $p = 0.2415$). This was consistent with the learning abilities of animals observed for 0.2 vs. 0.1 LPM (Figure 3-13B1, two-way ANOVA, $F(11,132) = 1.162$, $p = 0.3198$). Once they reached the asymptotic phase of learning, two groups of animals (experimental group for 0.3 vs. 0.6 LPM and 0.2 vs. 0.1 LPM) underwent bulbectomy. Sham surgery was likewise performed on two groups of animals that were trained on different airflow pairs. Following surgery, animals were given a 12-15-day recovery period before being tested on the airflows that they had been trained on before the surgery. The performance of bulbectomized animals dropped to chance levels, which was not observed in animals that underwent sham surgery (Figure 3-13A1 and B1, Bulbectomy vs. Sham surgery group for 0.6 vs. 0.3 LPM and 0.2 vs. 0.1 LPM: two-way ANOVA with Tukey's multiple

comparison test, * represents $p<0.05$). The learning accuracies of sham surgery mice were much higher than those of the bulbectomized animals, which remained at chance level even after 600 trials of training (Figure 3-13A1 and B1). Furthermore, this influence on performance was not attributable to a change in the animals' motivational levels, as the ITI for all groups of animals for both airflow pairs was the same (Figure 3-13A2 and B2, one-way ANOVA: 0.6 vs. 0.3 LPM – $F = 1.841$, $p = 0.1466$, 0.2 vs. 0.1 LPM – $F = 2.304$, $p = 0.0839$). These results provided conclusive evidence of OB being crucial for information processing of ethologically relevant airflows.

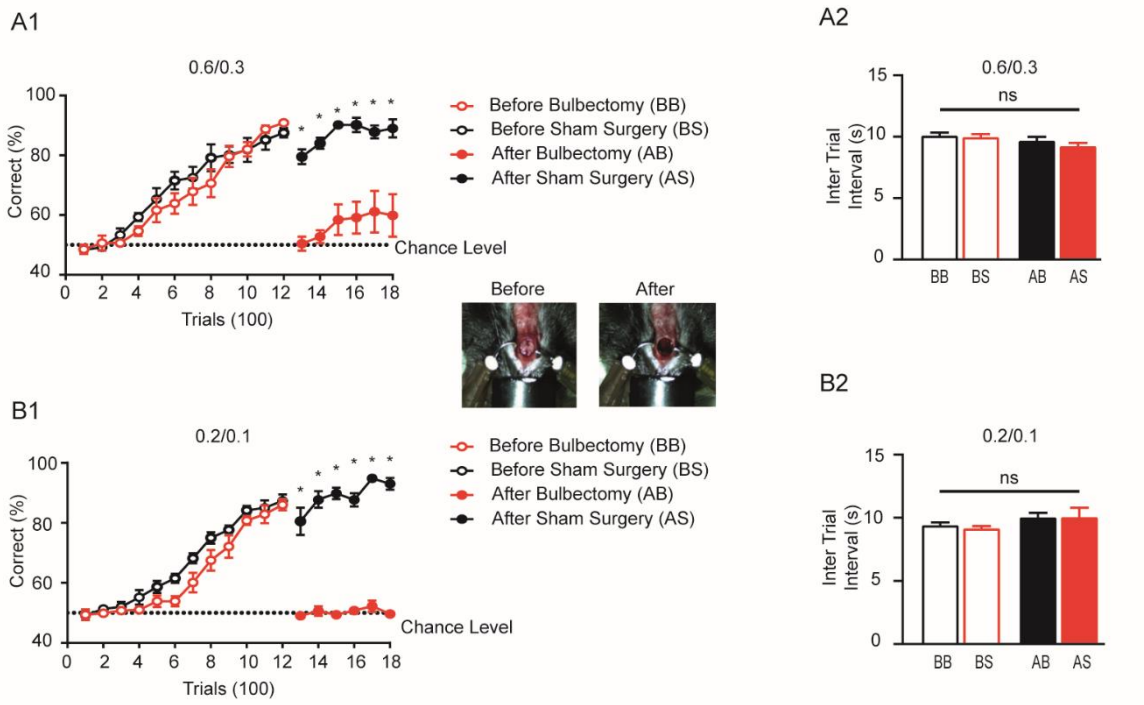

Figure 3-13 – OB is essential for airflow discriminations in mice

A) (A1) Learning of two groups of animals for 0.6 vs 0.3 LPM before and after the surgery. Before the surgery both bulbectomized and sham surgery group showed similar learning pace (two-way ANOVA, $F(11,132) = 1.282$, $p = 0.2415$, $n_{bulbectomy} = 8$, $n_{sham} = 6$). Following surgery, the performance of bulbectomized group dropped to the chance level and remained so for 600 trials, however the sham surgery group did not show any performance deficit (two-way ANOVA with Tukey's multiple comparison test, * represents $p<0.05$, $n_{bulbectomy} = 7$, $n_{sham} = 6$).

(A2) Inter-trial intervals of different groups of animals for 0.6 vs. 0.3 LPM before and after the surgery. ITI of the animals did not reveal any significant differences across different groups and surgical manipulations (one-way ANOVA, $F = 1.841$, $p = 0.1466$).

B) (B1) Learning of two groups of animals for 0.2 vs 0.1 LPM before and after the surgery. Before the surgery both bulbectomized and sham surgery group showed similar learning pace (two-way ANOVA, $F(11,132) = 1.162$, $p = 0.3198$, $n_{bulbectomy} = 8$, $n_{sham} = 6$). Following surgery, the performance of bulbectomized group dropped to the chance level and remained so for 600 trials, however the sham surgery group did not show any performance deficit (two-way ANOVA with Tukey's multiple comparison test, * represents $p<0.05$, $n_{bulbectomy} = 5$, $n_{sham} = 6$).

(B2) Inter-trial intervals of different group of animals for 0.2 vs. 0.1 LPM before and after the surgery. ITI of the animals did not reveal any significant differences across different groups and surgical manipulations (one-way ANOVA, $F = 2.304$, $p = 0.0839$).

3.4. Discussion

The olfactory system has traditionally been thought to be involved in sensing and processing chemical information (odorants and pheromones). However, few studies pointed towards the role of olfactory system in sensing and processing mechanical stimuli related information (14,16,77,211,217,223). Despite of these limited experimental evidences, behavioural relevance and neural mechanisms underlying this property remain unknown. In this chapter, we demonstrated for the first time that rodents can detect and discriminate between airflows devoid of odour molecules using their olfactory system.

3.4.1. Olfactory system aids airflow detection and discrimination in mice

During this study, we successfully developed a novel instrument to train animals on an airflow-based discrimination task using the Go/No-Go operant conditioning paradigm (208). Since whiskers and olfactory systems were potential sensory systems for airflow detections and discriminations (13,40,41,223), we investigated the role of the whisker and olfactory system in airflow sensing by doing various surgical manipulations, including whisker trimming, olfactory sensory neuron ablation via intranasal zinc sulphate and IP methimazole injections, and surgical aspiration of the olfactory bulb. Discrimination abilities of animals in the presence and absence of whiskers and the role of olfactory sensory periphery and the pre-cortical centre were tested over a range of airflows between 0.1- 1.5 LPM.

Although animals could discriminate airflows in the absence and presence of whisker, ablation of either olfactory sensory neurons or OB resulted in a deficit in this discrimination behaviour, indicating that the olfactory system is critical for detection and discrimination of ethologically relevant airflows. Furthermore, while performing an airflow-based discrimination task, animals were observed to sample airflows with their nose, and their sampling frequency increased. Additionally, since all sensory systems including vision, hearing, taste, touch, and smell follows the Weber's law of just noticeable differences (224–228), and as this study revealed a novel sensory dimension of olfactory system, it is important to assess whether airflow detection and discrimination via the olfactory system also adheres to this law. According to the law, the change in a stimulus that is barely noticeable is a constant ratio of the original stimulus (229). In other words, "the minimum increase in stimulus required to produce a perceptible increase in sensation is proportional to the pre-existing stimulus. We attempted to test it by training animals at three different initial stimuli and quantified their Just

Noticeable Difference (JND_{75} – 75% as the threshold) and proportionality constant (k) by subjecting them to discrimination task. One group of animals was trained first on 0.1 vs 0.15 LPM, and the animals reached an asymptotic level of learning. Following that, the base airflow was held constant at 0.1, while the other airflow was gradually reduced from 0.15 to the point where animals could not perform with more than 75% accuracy (Figure 3-14). This difference threshold point was designated as JND_{75}. JND_{75} was also calculated for different groups of animals with base airflows of 0.2 and 0.3 LPM and the increase in the base airflow correlated with the JND (Figure 3-15A, $R^2 = 0.9994$, $p = 0.0160$). In addition, the Weber's constant (k) observed for base airflow 0.1, 0.2 and 0.3 were similar (Figure 3-15B, one-way ANOVA $F = 0.2330$, $p = 0.7941$), providing preliminary evidence indicating that airflow sensing via olfactory system may follow Weber's law. However, additional studies with more groups of animals and different base airflows will allow further validation.

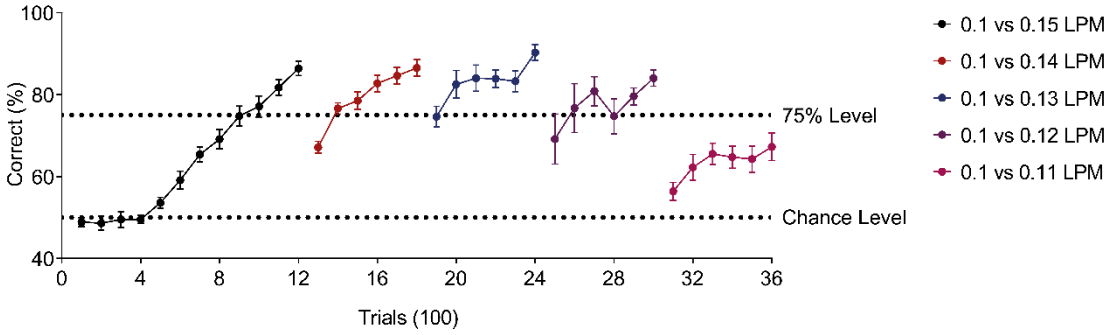

Figure 3-14 – Finding difference threshold during airflow discrimination

Animals trained to discriminate different airflow rates (0.1 vs. 0.15 LPM, 0.1 vs 0.14 LPM, 0.1 vs. 0.13 LPM, 0.1 vs. 0.12 LPM, 0.1 vs. 0.11 LPM) in order to calculate the just noticeable difference (JND_{75}) while the difference threshold was kept at 75% accuracy.

Together, these findings support the claim that the olfactory system aids airflow detection and discrimination in mice and while sensing airflows olfactory system may operate under principles that are universal for sensory systems. We propose that mechanosensation by olfactory system may contribute towards navigation, because during the natural exploration of an animal, the behaviourally important information is obtained from odour plumes that mediate the dispersal of odorant molecules from the source with the help of the airflows. While odour concentrations in an odour plume reveals only a limited information about the location of the

source (19,23), the OSN-mechanosensation may provide additional mechanical information in the form of direction cues (23). However, future research that examines the involvement of the olfactory system mechanosensation in olfactory navigation will provide a greater understanding on the behavioural significance of such a property.

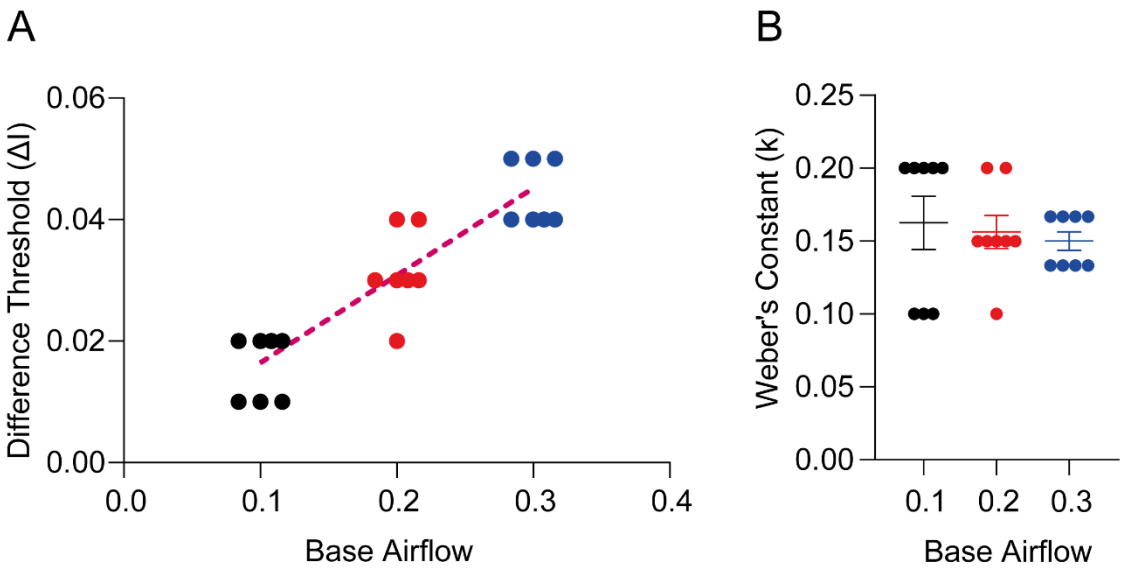

Figure 3-15 – Airflow discrimination via olfactory system follows Weber's Law.

A) Difference threshold (ΔI) for different base airflows. Point represents values of ΔI for individual animals. ΔI increases with increase in the airflow base value (R^2 = 0.9944, p = 0.060). Magenta dotted line shows linear regression with R^2 = 0.8300 and slope = 0.1438) (n = 8 for all three base airflows).

B) Weber's constant (k) calculated for different base airflows. The dots represent individual values whereas horizontal line represents mean along with SEM (one-way ANOVA, F = 0.2330, p = 0.7941) (n = 8 for all three base airflows).

3.4.2. Stimulus independent airflow discrimination times

The effects of stimuli on odour discrimination times have been thoroughly investigated. Odour discrimination times have been observed to vary with factors such as stimulus complexity, reinforcement schedule, and animal motivation level (208,230–233). While odour discrimination times were observed to be longer when animals were trained to discriminate complex mixtures versus simple binary odours (208,210,230), airflow discrimination times were consistent and did not change with the stimulus. Airflow discrimination times were always observed to be in the 300-500 ms range, with these times being non-significant across

different airflow pairs. These stimulus independent airflow discrimination times could be explained by the activity patterns evoked at the level of OSNs and thereby the characteristics of glomerular activity patterns produced by different airflows. In-vitro calcium recordings from the glomeruli of double tracheotomized animals revealed that airflow causes oscillations in the glomeruli, with the phase remaining constant while the amplitude changing as the airflow rate increases. The phase observed for different airflows was equivalent to the time of two sniff cycles, which roughly corresponds to the discrimination time range (14). Thus, it can be argued that in order to discriminate airflows, animals must complete at least two sniff cycles in order to efficiently sample airflows and thus make a decision. This assumption is consistent with the conclusions from the breathing raster plots of different airflows, wherein a broader sniffing response was observed that remained high from stimulus onset to discrimination time. These results provide novel insights into the potential mechanism that the olfactory system may employ to detect and discriminate airflows.

3.4.3. Sniff invariant airflow information coding

Rodents are known to adjust their breathing behaviour in different contexts in order to gather as much information as possible for better odour discrimination. They increase their breathing frequency when investigating a new odour source or performing an odour-based task (234). During the decision-making phase of an odour-based discrimination task, their sniffing frequency increases (209). Rodents also exhibited an increase in sniff frequency during the decision-making period while performing an airflow-based discrimination task, similar to what was observed for odours. The sniff frequency remained high during the decision-making window and then returned to baseline. The sniffing frequency remained unaffected by stimulus strength during the decision-making period, indicating that sniff invariant airflow sampling is being done. The phase coding of the M/T cells may be used to explain this finding. Given that sniffing is known to cause oscillations in the M/T cells of animals that are artificially breathing, and that only the amplitude of these oscillations is affected by the strength of the airflow, sniff invariant airflow information processing offers a reliable mechanism to maintain the phase of these oscillations (14). In addition, the sniff frequency of animals was same for S+ (rewarded) and S- (unrewarded) airflows during the decision-making period. However, a total increase in the sniff frequency of S+ was observed when compared to S-. Since licking and breathing are synced via orofacial senses (202,219), and animals lick for S+ odour after decision in order to get the reward, the overall increase in sniff frequency for S+ is most likely

due to licking. These findings suggest that breathing synchronisation during the decision-making window was not driven by airflow strength or reward anticipation. Because sniff frequencies are independent of airflow strengths, sniff invariant coding is proposed for the airflow information processing through rodent olfactory system. This property is conserved for different cues (chemical and mechanical) that are processed through olfactory system, as there is a growing consensus of sniff independent odour coding (235–237).

3.4.4. Differential sampling strategies for odour and airflow tasks

Sniffing strategies of rodents vary in order to sample airflow and odour stimuli through the olfactory system. Overall sniffing responses and temporal sniff dynamics were observed to differ between these two stimuli. While sniffing frequency increases for both airflows and odours during decision making time, airflows showed sniff responses lasting longer as compared to odorants. These differences in the sniffing behaviour for airflows and odours correlates with the glomerular activation topology as revealed by fMRI (77). The airflows were observed to exhibit broader weaker responses and oscillations, whereas odour exhibited intense localised responses (14,77). In addition to sniff frequency variations, the ratio of time spent by animals in inhalation and exhalation phase was also different between airflows and odours. Animals spent the same amount of time inhaling and exhaling for airflow-based decisions (Figure 3-11E, Inhalation: Exhalation ratio ~ 1), indicating that mechanosensation evoked by these processes might be contributing towards airflow discriminations. We were unable to measure the sniffing amplitudes for various airflows in this work, however, quantifying this would undoubtedly give us additional understanding of the airflow-related sniffing mechanisms. In contrast, for odour-based decisions the inhalation to exhalation time ratio was higher (Figure 3-11E, Inhalation: Exhalation ~ 1.5), implying that animals spent more time in inhalation phase. Spending longer time in the inhalation phase enables animals to gather the maximum amount of odorant molecules from their surroundings in order to complete an effective olfactory percept. In addition, the peak latency during the airflow discrimination task was sharp and preceded the stimulus onset, whereas the peak coincided with the discrimination time during the simple odour discrimination task. Also, the difference between discrimination time and the peak latency for airflows was significantly higher, suggesting that airflow information processing may require more time as compared to odours. Although, this chapter provides relevant information regarding peripheral mechanisms involving airflow information processing, it is still unknown how the olfactory bulb network as a whole modulates this

information and leads to perception. This question will be thoroughly addressed in the following chapter of this thesis.

3.5. Future Directions

Although we have demonstrated conclusively that the rodent olfactory system is involved in airflow detection and discrimination, there are still a few unanswered questions. The most important ones are: how is airflow sensed, and what receptors are involved. Despite previous research indicating that G-protein coupled receptors (217,223), which govern the canonical odour sensing pathway, may also be involved in airflow sensing, the causal link between these two has yet to be established. In our lab, we are investigating the presence of piezo 2 on the cilia of the main olfactory epithelium to dissect out a possible channel mediating mechanosensation through olfactory system.

CHAPTER 4

Synaptic inhibition in the olfactory bulb modulates airflow detection and discrimination behaviour

4.1. Introduction

When sensory systems are processing the stimulus, the neural representations that form are refined over time. The olfactory system in rodents is unique as it possesses a highly specialized pre-cortical region called the olfactory bulb (OB) that performs significant signal refinement by inhibitory circuits before sending it to higher cortical regions (16,238–241). The OB is the first relay station in the olfactory pathway, receiving signals directly from olfactory sensory neurons. OSN axons converge into OB in a specific location known as glomeruli. This convergence occurs in a receptor-specific manner, resulting in a meaningful topographic organization in the OB. In OB, a single glomerulus receives information from thousands of OSNs, which form synapses with Mitral/Tufted cells. M/T cells, which are olfactory bulb output neurons, send signals to higher cortical areas for further processing (17). Different interneurons located in different layers of the OB modulate M/T cell activity and transform stimulus-associated information.

The glomerular layer (GL) of the OB contains Juxtaglomerular cells, which are a mix of Periglomerular (PG) cells, Short-axon (SA) cells, and External Tufted cells (ET). The extensive dendritic arborization of these Juxtaglomerular cells exists within a single glomerulus and significantly alters odour information (32). Interactions of M/T cells with these interneurons within the glomerulus can be both inhibitory and excitatory, with inhibitory interactions being the most prevalent. The PG cells are inhibitory interneurons that use neurotransmitters such as gamma-aminobutyric acid (GABA), dopamine, or a combination of the two to exert their inhibitory action (34,242). The majority of PG cells express one of two GABA isoforms: GAD 65 and GAD 67 (34). While PG cells expressing GAD 67 are also Tyrosine hydroxylase positive and thus dopaminergic-GABAergic neurons, PG cells expressing GAD 65 are exclusively GABAergic (42). PGs have distinct functions that include directly inhibiting M/T cells, retrogradely inhibiting OSNs, and laterally inhibiting the neighbouring PG cell (33,35,237,243). In addition to this direct action, OSNs can activate PGs by activating ET cells. ET cells are intraglomerular excitatory interneurons. ET cells receive

glutamatergic inputs from OSNs within a glomerulus, which can then provide monosynaptic glutamatergic inputs to SA and PG cells (243–245). In addition to the modulatory actions of PG and ET cells, the GL contains SA cells, which aid in the overall modulation of glomerular activity (34). SA cells are GABAergic and dopaminergic, and the majority of them are activated disynaptically by OSNs via ET cells, with only a few being activated monosynaptically. SA neurons are unique in that they can form excitatory synapses with PG cells that are nearly ~ 20 glomeruli away. This interglomerular interaction mediated by SA cells allows an activated glomerulus to suppress the activities of surrounding glomeruli via centre-surround inhibition thereby, increasing the spatial contrast between odour-evoked glomerular activity patterns (246,247).

Just beneath the GL lies the external plexiform layer (EPL). EPL receives several secondary M/T cell lateral dendrites, which form dendro-dendritic synapses with granule cells (GC) and parvalbumin (PV) expressing interneurons (248). The GCs lies primarily in the granule cell layer (GCL) and PV positive cells lies primarily in the EPL layer of the OB. GCs are GABAergic in nature and, like PGs, express either of the two GABA isoforms (GAD 65 or GAD 67) (242). Although GAD-expressing neurons are found in most OB layers, the primary layers are GL and GCL. Between GL and GCL, GCL has the highest proportion of GAD positive interneurons, accounting for 98 percent versus 55 percent in GL (42). M/T cells generate action potentials in response to excitatory input from OSNs, which causes dendritic glutamate release, which activates ionotropic glutamate receptors on GCs. This further leads to stochastic Ca2+ transients in GC spines, resulting in GABA release from GCs (248–250). The GABA released then binds to the receptors on the M/T cells, inhibiting them. If the GABA released inhibits the same M/T cell, this is known as recurrent inhibition; if it inhibits a neighbouring M/T cell, this is known as lateral inhibition (37,251). Because M/T cells are the OB's output neurons, the interaction of GCs with M/T cells modulates the OB's overall gain output (36,252). The inhibition provided by GCs aids decorrelation and may be a key mechanism for increasing the spatial contrast between odour-evoked glomerular activity patterns, enabling discrimination of odours that elicit highly overlapping glomerular activity (37,253,254). In addition to decorrelating M/T cells firing activities via inhibitory mechanisms, activation of GCs with different latencies also plays a crucial role in generating M/T cells' temporal patterns, which in turn influence the activity of other granule cells, thereby providing a dynamic feedback loop (255). Although GCs have been shown to play an important role in the discrimination of complex odours through contrast enhancement and decorrelation

(37,254,256–258), their role and mechanism in processing airflow information, which represents another sensory dimension for the olfactory system, remain unknown. As a result, we are attempting to focus on the roles of GCs in the processing of airflow information in this chapter. This is primarily accomplished by addressing the following objectives:

1. To investigate the activation of different cells of the OB in an airflow-based discrimination task.

Since GCL neurons were most abundantly activated by airflows, further experiments were carried out to investigate their role in airflow information processing.

2. To test whether airflows can elicit responses in GCL neurons, specifically in neurons that express GAD-65.
3. To determine whether optogenetic modulation of the activity of GAD-65 expressing neurons can alter airflow discrimination.

4.2. Materials and Methods

Mice were trained on olfactory GNG behavioural paradigm under FM or HR conditions. The detailed methods for these behavioural paradigms are explained in material and methods chapter (section 2.3.1 and 2.3.2).

4.2.1. Animals used

To train animals under freely moving conditions, male C57BL6/J mice were used in behavioural experiments. Mice were 6-8 weeks old when behavioural experiments began. For Ca2+ imaging of GCL interneurons, B6N.Cg-Gad2$^{tm2(cre)Zjh}$/J line was crossed (Figure 4-1) with B6.129SGt(ROSA)$^{26Sortm95.1(CAGGCaMP6f)Hze}$/J for expression of GCaMP6f in GAD 65 positive cells. In order to perform optogenetics experiments under head restrained conditions, B6N.Cg-Gad2$^{tm2(cre)Zjh}$/J line was crossed with B6.Cg-Gt(ROSA)$^{26Sortm32(CAGCOP4*H134R/EYFP)Hze}$/J or B6.129SGt(ROSA)$^{26Sortm35.1(CAGaop3/GFP)Hze}$/J (The Jackson Laboratory) line to specifically express channel rhodopsin (ChR2) and archaerhodopsin (Arch) in GAD 65 positive cells. The animals were genotyped using DNA from tail samples and also characterized by studying the expression of fluorescent markers in targeted GAD 65 interneuron population.

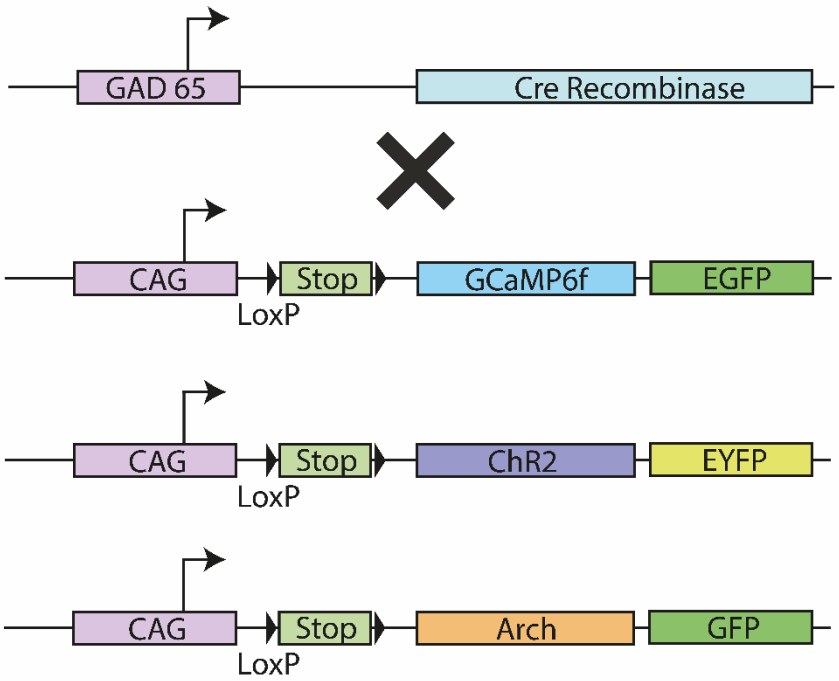

Figure 4-1 – Scheme of genetic crosses used in calcium imaging and optogenetics experiments
To achieve stable expression of ChR2, Arch, and GCaMP6f in GAD 65 +ve neurons in different sets of animals, homozygous GAD 65-Cre mice were crossed with homozygous conditional mouse lines for ChR2, Arch, and GCaMP6f.

4.2.1.1. Genotyping details

The GAD 65-cre, ChR2-floxed, Arch-floxed, and GCaMP6f-floxed mice were kept in homozygous condition, as recommended by Jackson Laboratories. Primer sequences for the aforementioned mouse lines were obtained from the Jackson Laboratory website and used for genotyping. During weaning, tail clips of approximately 2 mm length were collected from young mice for genotyping. We isolated DNA from tissue for genotyping using the KAPA Express Extract Kit (Kapa Biosystems), as recommended by Jackson Laboratories. The KAPA2G Fast Genotyping Mix was then used to set up PCR reactions (Kapa Biosystems). In standard TAE (Tris base, acetic acid, and EDTA) buffer, a 2% agarose gel was prepared. The gel was loaded with PCR product (14 µl) + loading dye (6x, 1 µl) in each well. A 3-4 µL DNA ladder separated by 100 base pairs (bp) was loaded into one of the wells. Because the expected bands were far apart, running the power unit at 100-120V for 30-45 minutes resolved the bands.

4.2.1.2. Phenotyping details

Adult GAD 65-GCaMP6f mice were perfused with 20 ml chilled Dulbecco's phosphate-buffered saline (DPBS), then fixed with 4% PFA to examine GCaMP6f expression. The saturating Ca2+ concentration (0.9 mM) in DPBS increases the fluorescence of GCaMP6f. The dissected brain was stored in 4% PFA overnight after perfusion. It was then embedded in 2% low melting agarose in DPBS and vibratome-cut into 50-µm free-floating coronal sections. Sections were stained with 4',6-diamidino-2-phenylindole (DAPI) to check for co-localization with nuclei (Sigma, 1:500). Confocal images were taken to confirm the presence of GCaMP6f in GAD 65+ve neurons in the OB.

GAD 65-Cre mice were crossed with either ChR2- or Arch-floxed mice, and one F1 mouse was phenotyped for ChR2 or Arch protein expression in GAD 65 +ve cells. Following perfusion with 4% paraformaldehyde (PFA) in a 0.1 M phosphate buffer (PBS), the brain was dissected. The dissected brain was stored in 4% PFA overnight for further fixation. The tissue was embedded in 2% low melting agarose (LMA, Sigma) the next day, and 50 µm

free-floating coronal sections were taken with a vibratome. To confirm the expression of ChR2 and Arch in GAD 65 +ve neurons, the sections were stained with DAPI (Sigma, 1:500) and confocal images were taken. ChR2 and Arch expression in GAD 65 interneurons was confirmed by co-localization of DAPI with EYFP and GFP, the tagged fluorescent markers with ChR2 and Arch, respectively.

4.2.2. Immunohistochemical staining of c-fos protein in the olfactory bulb sections

A new group of GAD-EYFP mice (n = 7) were trained to distinguish between 0.2 and 0.1 LPM. Three mice were randomly processed for immunohistochemical analyses once they reached the asymptotic phase of learning. Mice were perfused with (1X) PBS and 4% PFA, and the dissected brain was stored at 4 °C for 24 hours in 4% PFA. 50 µm floating coronal sections were taken with a vibratome. These sections were washed three times for 15 minutes each with 1X Tris Buffered Saline (TBS). Blocking was performed for two hours to remove any non-specific binding. The blocking solution contained 0.2% Triton-X (Sigma), 7.5% Normal Goat Serum (NGS) (Abcam, ab7481), and 2.5% Bovine Serum Albumin (BSA) (Sigma Aldrich) in TBS. Following blocking, primary antibody was used: rabbit anti-c-fos (1:500 dilution). The sections were incubated overnight at 4 °C for 13-15 hours. The following day, three TBS washes (15 minutes each) were given. The secondary antibody was then incubated at room temperature for two hours. The secondary antibodies used was anti-rabbit Alexa Flour 594 (1:500 dilution) (Jackson Immunoresearch, USA, code:111-585-003). Three TBS washes (15 minutes each) were given. Finally, the sections were stained with DAPI (Sigma, 1:500 dilution in 1% NGS) for 10 minutes and were mounted on the slides. The sections were imaged using Leica Sp8 confocal microscope.

4.2.3. Micro-endoscopic Ca^{2+} imaging

Two groups of GAD 65-GCaMP6f mice were used to perform Ca2+ imaging. The first group consisted of 5 animals that underwent calcium imaging while anaesthetized, while the second group consisted of 5-7animals that underwent calcium imaging while awake.

4.2.4. Implantation of imaging cannula

1. The animals were anaesthetized with a combination of ketamine and xylazine. The anaesthetized animal was then mounted on the stereotaxic instrument.
2. An incision was performed on the skull over the olfactory bulb area, and the skull was completely cleaned.
3. A 1mm cranial window was created in the centre of the right hemisphere of the olfactory bulb using a dental drill.
4. A 1 mm track was made by inserting a blunt Hamilton needle in the olfactory bulb. The needle was kept in the OB for 5 mins before being taken out. 1 mm was chosen based on the observation that most of the GAD 65 expressing interneurons lies at this depth.
5. The 1 mm protruding GRIN lens was lowered vertically until it reached the GCL.
6. To secure the lens assembly to the skull surface, a combination of cyanoacrylate gum and acrylic dental cement was used.
7. A headpost was implanted behind the implanted lens.
8. Mice were given a month to recover.

4.2.5. Image acquisition

Calcium imaging was performed on animals while they were anaesthetized and awake under head restrained conditions. GAD 65 +ve interneurons in the OB GCL were imaged using a snap-in fluorescence microscope (OSFM model L, Doric lenses Inc., Canada) mounted on an implanted GRIN cannula (1 mm length). The cannula had a working distance of 80 µm and a focal range of 50 µm. At a frame rate of 10 Hz, a field of view corresponding to 350 µm X 350 µm that was further binned to 2 X 2 times, was imaged (Figure 4-2). The CE: YAG fluorescence source of 465 nm output was set used with power ranging from to 400- 700 mA.

For imaging under anaesthetized conditions, an IP injection of a ketamine-xylazine cocktail was administered to animals before beginning of each session. Before mounting the animals on the setup, their toe reflexes were tested. Each session consisted of 60-80 trials with an inter-trial interval of 13.2 seconds. The animals (first group n = 5 mice) were given different airflows with the stimulus of 100, 200, 300, and 400 mL/min, which were presented to them in a pseudorandomized fashion. Twenty trials per animal were conducted and analysed for each airflow.

Animals were subjected to standard airflow-based detection and discrimination tasks under head restraint conditions for imaging under awake state. Animals (second group n = 5-7) mice were first pretrained before imaging was performed while mice were passively exposed to various airflows (same as above) during the detection task in a pseudorandomized manner. Each session consisted of 60-80 trials with an inter-trial interval of 13.2 seconds. Twenty trials per animal were conducted and analysed for each airflow. Only one session per day was conducted. Calcium traces were also recorded in animals during an airflow-based discrimination task. They were trained to distinguish between two airflows: 0.5 vs. 0.4 LPM (4 tasks - 1200 trials). Calcium traces were recorded during the first 40 trials (20 S+ and 20 S-) of each task (300 trials) at the start of each task. An external tone TTL signal from the olfactometer synchronised Ca2+ imaging to the start of the trial. The imaging for each trial lasted 10 seconds, with the first 1.2 seconds serving as a baseline, followed by stimulus delivery for 2 seconds. The imaging was done at a resolution of 100 ms. The trial-by-trial imaging data was compiled by comparing the trial sequence generated by the olfactometer result file.

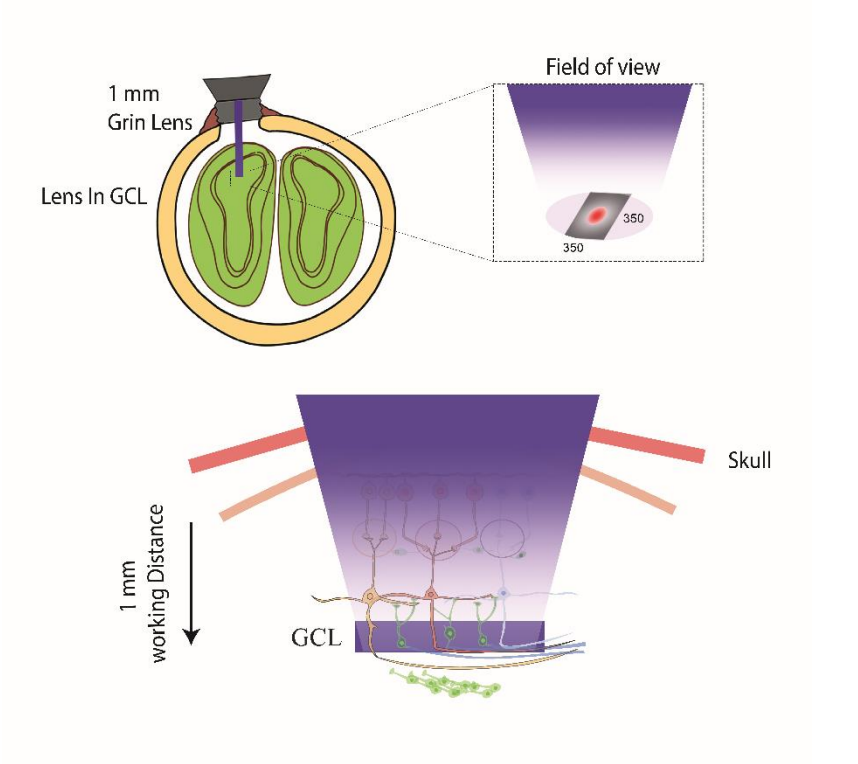

Figure 4-2 – Illustration representing micro-endoscopic imaging

Depth range and field of view of imaging cannula used for imaging GCs.

4.2.6. Imaging analysis

Custom Python scripts were used to analyse the images. The population activity was analysed by selecting the regions-of-interest (ROIs) of 300 µm X 300 µm. If there were any frame drops during image acquisition, such trials were identified and excluded from the analysis. The relative changes in fluorescence for each frame were calculated using F(t)/F0 = [F(t) - F0]/F0, where F0 is the mean activity during the baseline. The F0 was calculated on a trial to trial basis. The F(t)/F0 amplitude and area under the curve (AUC) of individual animals were measured on a trial to trial basis.

4.2.7. Optogenetic modulation of OB specific GAD 65 expressing interneurons

To investigate the effects of inhibition on M/T cells and their effects on airflow detection and discrimination behaviour, we optogenetically modulated the activity of OB specific GAD 65 expressing interneurons in a bidirectional manner by expressing ChR2 and Arch under the GAD 65 promoter. Three different set of animals were used for optogenetic experiments: First group – GAD 65-Arch (n = 12-14), Second group – GAD 65-ChR2 (n = 7-10), Third group – GAD 65-EYFP (n = 12-14). While mice were performing airflow/odour discrimination, GAD 65 +ve interneurons were photo-stimulated/photo-inhibited. To activate the interneurons, we used 5 ms pulses of blue light (473 nm specific for ChR2) at a frequency of 40 Hz. To inhibit the interneurons, we used 1000 ms pulses of amber light (595 nm specific for Arch) at 1 Hz frequency (Figure 4-3A and B). For these sets of experiments, the light stimulations were timed to coincide with the onset of the stimulus.

4.2.8. Cranial window and LED implantation

Blue or amber LEDs were implanted over the OB region to achieve optogenetic modulation of OB specific GAD 65 +ve interneurons (Figure 4-3A and B). To avoid direct contact with brain tissue, the LEDs were implanted over cranial windows. The detailed procedure for creating a cranial window and implanting LEDs is provided below.

1. The animals were anaesthetized with a combination of ketamine and xylazine.
2. The anaesthetized animal was then placed on the stereotaxic instrument.
3. An incision was made over the skull, and the skull was thoroughly cleaned.
4. A window 2.5 mm in diameter was created over the olfactory bulb region using a tissue puncture.

5. Using a blunt-ended dental drill bit, a circular slit in the skull was made around the perimeter of drilled area. Artificial cerebrospinal fluid (ACSF) (125 mM NaCl, 5 mM KCl, 10 mM Glucose, 10 mM HEPES, 2 mM CaCl2, 2 mM MgSO4, in 1 L sterile Distilled water, pH = 7.4) was applied on a regular basis while thinning the skull to avoid heating and damaging the tissue beneath.
6. Thinning continued until the vasculature of the cortical circuit was visible beneath the circular groove.
7. The slit was slowly removed from the skull using sharp forceps and the surface of the brain was then cleaned with ACSF.
8. To reduce inflammation, a drop of dexamethasone, a glucocorticoid steroid, was applied on the dura surface.
9. The exposed dura was then covered with a transparent cover slip (3 mm diameter), which was then secured to the cranial window by sealing its side with cold cure dental cement.
10. On the skull, a head post was implanted posterior to the cranial window.
11. The clarity of the cranial window was checked after one week, and an LED was mounted over it with cold cure dental cement.

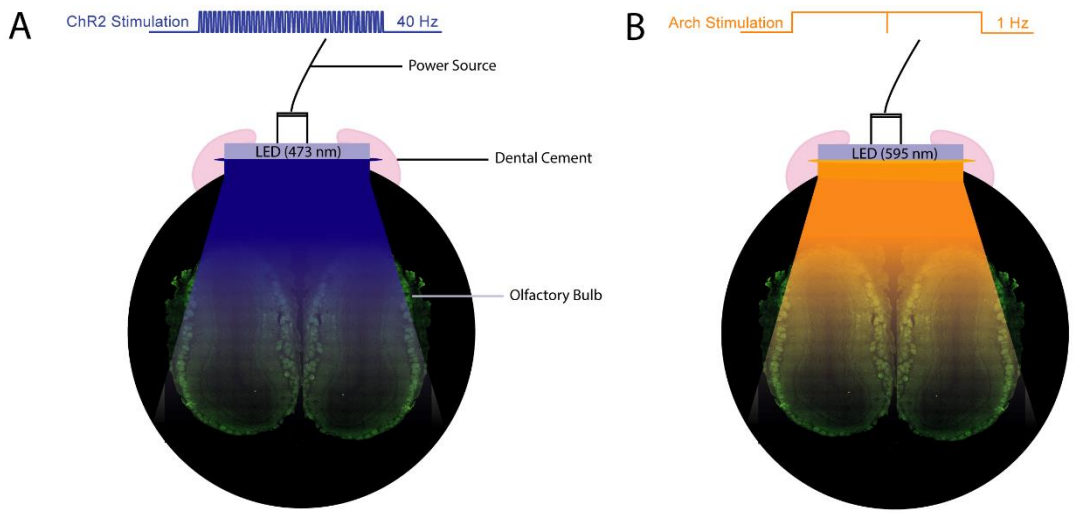

Figure 4-3 – Illustration representing optogenetic (LED) stimulation of the OB

A) A 473 nm blue LED is fixed on top of a circular cranial window over the OB in a GAD 65-ChR2 expressing mouse. Schematic of LED stimulation.

B) A 595 nm amber LED is fixed on top of a circular cranial window over the OB in a GAD 65-Arch expressing mouse. Schematic of LED stimulation.

4.2.9. Task Habituation phase and LED power standardization

After 1 week of LED implantation the water deprivation schedule of animals began. Animals were subjected to task habituation training three to four days after the start of the water deprivation schedule. The operant conditioning paradigm used for these animals was the same as for the head restrained task habituation phase. As optogenetic experiments were carried out to determine whether modulation of GAD 65 +ve interneurons affects airflow discrimination behaviour, and because the extent of transparency of the cranial window may vary between mice, the optimal power required to modulate the majority of GAD 65 +ve interneuron activity would also vary. As a result, when the animals completed the task habituation, the strength of the LEDs was standardised using the detection task. The LEDs were powered by an LED driver, and the stimulus used to standardise the LED power was a 0.2 LPM airflow stimulus. While standardising the LED intensity, we also ensured that tissue temperature do not go beyond the body temperature (37 °C). Using a laser power and energy metre, we measured the surface temperature of the LED and the wattage for each light power setting.

Animals were given the stimulus along with photodiode (LED) activation mounted over the OB corresponding region of the skull to standardise LED power. The photoactivation-ON trials were interleaved with no-photoactivation trials (20 light ON trials followed by 10 light OFF trials). Different light intensities were used, and 20-40 trials were performed for each LED intensity. Lick responses of animals were recorded and compared during stimulus presentation under light ON and OFF conditions. The average lick responses of the animals in GAD 65-Arch and GAD 65-ChR2 groups decreased as the intensity of LED increased (Figure 4-4A and B). For subsequent optogenetic experiments, the LED intensities of the animals were chosen so that there was no difference between the light ON and OFF states. whereas the lick responses of the control EYFP animals did not alter (Arch - 2.93 mw and ChR2 - 6.96 mw). Because GAD 65-EFYP was used as a control group and expressed EYFP, which is also expressed in GAD 65-ChR2, the intensity of light used for optogenetics training for these animals was the same as for the ChR2 group (6.96 mw). At this light intensity, there was no difference in the lick responses of these animals when compared to those in light OFF conditions (Figure 4-4C).

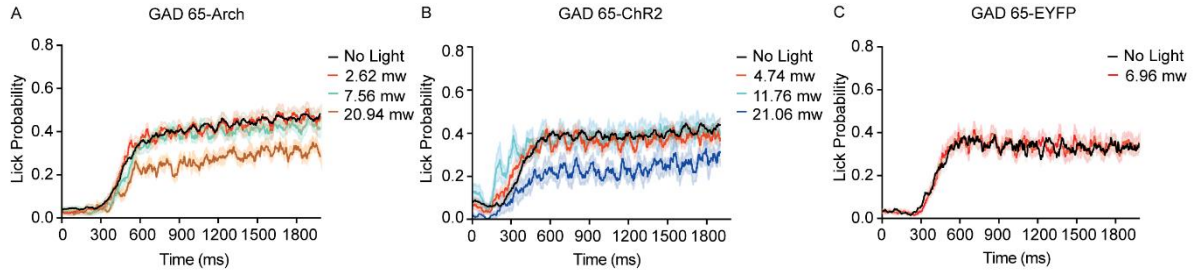

Figure 4-4 – LED power optimization for optogenetic modification of GAD 65 +ve interneurons

A) Average lick responses of GAD 65-Arch mice to different light intensities. The solid lines and shaded areas represent the mean and standard error of mean, respectively. Because each mouse licked differently at different LED powers, the LED power was determined individually.

B) Average lick responses of GAD 65-ChR2 mice to different light intensities. The solid lines and shaded areas represent the mean and standard error of mean, respectively. Because each mouse licked differently at different LED powers, the LED power was determined individually.

C) Average lick responses of GAD 65-EYFP mice at no light and light at 6.96 mw. The solid lines and shaded areas represent the mean and standard error of mean, respectively.

4.2.10. Sequence of discrimination training

Animals were trained for airflow discriminations under head restrained conditions, and the paradigm and reward criteria for this task were the same as those mentioned in the section on behavioural training under head restrained conditions. Whiskers of the animals were kept trimmed throughout the experiment, to rule out any possibility of whiskers being involved in airflow discrimination behaviour. In addition, we did not observe any changes in their discrimination abilities under whisker-deprived conditions (Chapter 3, Figure 3-3). The whiskers were trimmed once a week. The table below summarizes the order in which all of the animals performed discrimination tasks during optogenetic experiments.

Flow Pair/Odour Pair	Light condition	Airflow used
0.5 vs. 0.4 LPM (1200 trials)	Light OFF	
0.15 vs. 0.1 LPM (900 trials)	Light ON	
0.3 vs. 0.25 LPM (600 trials)	Light OFF	
0.45 vs. 0.35 LPM (600 trials)	Light ON	

0.6 vs. 0.6 LPM (300 trials)	Light OFF	
Octanol (+) (60%) (-) (40%) vs. Octanol (-) (60%) (+) (40%) (600 trials)	Light ON	0.6 LPM
Hexanal (60%) Pentanone (40%) (0.4 LPM) vs. Pentanone (60%) Hexanal (40%) (0.3 LPM) (600 trials)	Light ON	
Carvone (+) (0.6 vs. 0.4 %) (600 trials)	Light ON	0.2 LPM

Table 4-1 Training sequence of animals for various tasks under different photoactivation conditions

4.2.11. Statistical analysis

GraphPad Prism 9, Microsoft Excel, and Python were used for all statistical analyses in this chapter. To determine p-values and test for statistical significance, we used the student's t-test, one-way and two-way ANOVA, and associated post-hoc tests.

4.3. Results

4.3.1. OB interneurons shows activation towards airflow stimuli

We've already established that olfactory system of rodent aids in anemo-detection and -discrimination behaviour. To further investigate the OB specific neural mechanisms in processing airflow information, we examined the expression of c-fos (red colour dots – Figure 4-5A) in the OB of animals that had learned to discriminate airflows. We discovered that neurons in various layers of the OB were c-fos positive (Figure 4-5A). The c-fos signal was most abundant in the GCL layer, which contains the majority of GAD 65+ (EYFP labelled-green colour - Figure 4-5A) inhibitory interneurons. This finding provided preliminary evidence of olfactory bulb neuronal circuitry being involved in airflow discrimination. To further investigate and validate our findings, we measured the population calcium dynamics of GAD 65 +ve interneurons in the GCL in response to airflows while the animals were anaesthetized. This was achieved by expressing genetically encoded Ca2+ indicator GCaMP6f in GAD 65 +ve interneurons to record from the majority of OB GABAergic interneurons. We recorded population activity within the field of view using a micro-endoscopic GRIN lens inserted into the GCL of the OB at a depth of -1 mm. GAD 65 +ve interneurons were found to elicit population activity in response to different airflows (Figure 4-5B1 and B2). Ca2+ transients showed a slow rise and decay that was independent of stimulus strength (Figure 4-5C). The peak latency observed for different airflows were similar (0.1 LPM – 1900 ms, 0.2 LPM – 1960 ms, 0.3 LPM – 1925 ms, 0.4 LPM – 1900 ms). While the shape, onset, and offset of the calcium traces remained unchanged as stimulus strength increased, the amplitude of the DF/F0 increased and correlated with stimulus strength (Figure 4-5D, Pearson correlation: R^2 = 0.9911, p = 0.0045).

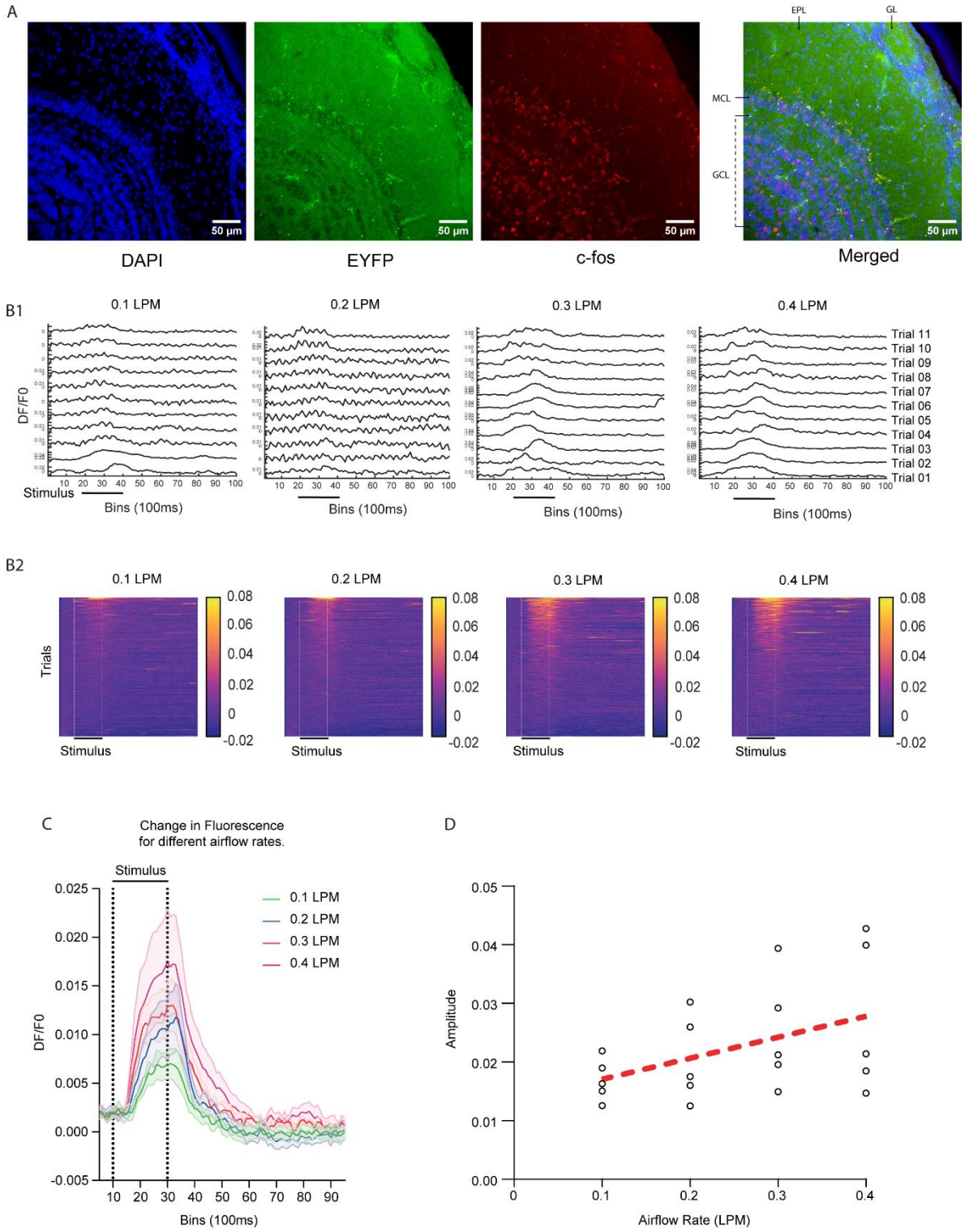

Figure 4-5 – GAD 65 +ve OB interneurons are involved in processing airflow stimuli

A) c-fos expression in various OB layers in animals trained to distinguish between different airflows. The GCL layer, which houses the majority of the GAD 65 expressing interneurons, has the highest level of c-fos expression. Blue - DAPI staining, Green - GAD 65 - EYFP staining, Red - c-fos staining.

B) B1) Trial-by-trial traces of GAD 65 +ve OB interneuron response to different airflows in a single animal under anaesthetized conditions.

   B2) Pseudo-colour heatmaps of Ca2+ dynamic responses elicited by various airflows. Data were collected from 5 mice, with 20 trials for each airflow. Data from all trials are sorted in decreasing order of Ca2+ response during airflow application. For all the airflows, GAD 65 interneurons showed activity towards airflows during the stimulus presentation period.

C) The average DF/F0 responses of all animals for various airflows. The solid line represents the mean across all animals, while the shaded area represents the standard error of the mean. The DF/F0 increased after the stimulus presentation and decayed after the stimulus offset.

D) The graph depicts the change in amplitude as the stimulus strength increases. Individual dots represent animal wise amplitude values. The amplitude is found to be positively correlated with stimulus strength (Pearson correlation: $R^2 = 0.9911$, $p = 0.0045$, $n = 5$ mice).

We then investigated the kinetics of Ca2+ signals in awake mice in response to various airflow stimuli. In awake conditions, the interneurons responded to all airflows as shown by the heatmaps (Figure 4-6A), but their responses were different from what was observed in anaesthetized conditions (Figure 4-6B). The amplitudes were observed to change between the anaesthetized and awake states. When peak amplitudes for different airflows were compared in the awake and anaesthetized states, the peak amplitude was significantly higher in the anaesthetized state for all airflows (Figure 4-6B, Peak amplitudes for 0.1 LPM: Anaesthetized – 0.1696 ± 0.0016, Awake – 0.0096 ± 0.0030; one-tailed unpaired t-test, $p = 0.0452$, for 0.2 LPM: Anaesthetized – 0.2046 ± 0.0032, Awake – 0.0089 ± 0.0016; one-tailed unpaired t-test, $p = 0.0025$, for 0.3 LPM: Anaesthetized – 0.2487 ± 0.0043, Awake – 0.0082 ± 0.0019; one-tailed unpaired t-test, $p = 0.0015$, for 0.4 LPM: Anaesthetized – 0.2745 ± 0.0057, Awake – 0.0099 ± 0.0017; one-tailed unpaired t-test, $p = 0.0037$). In summary, these findings provide the first in vivo evidence of OB interneurons being active in response to airflows in both anaesthetized and awake conditions.

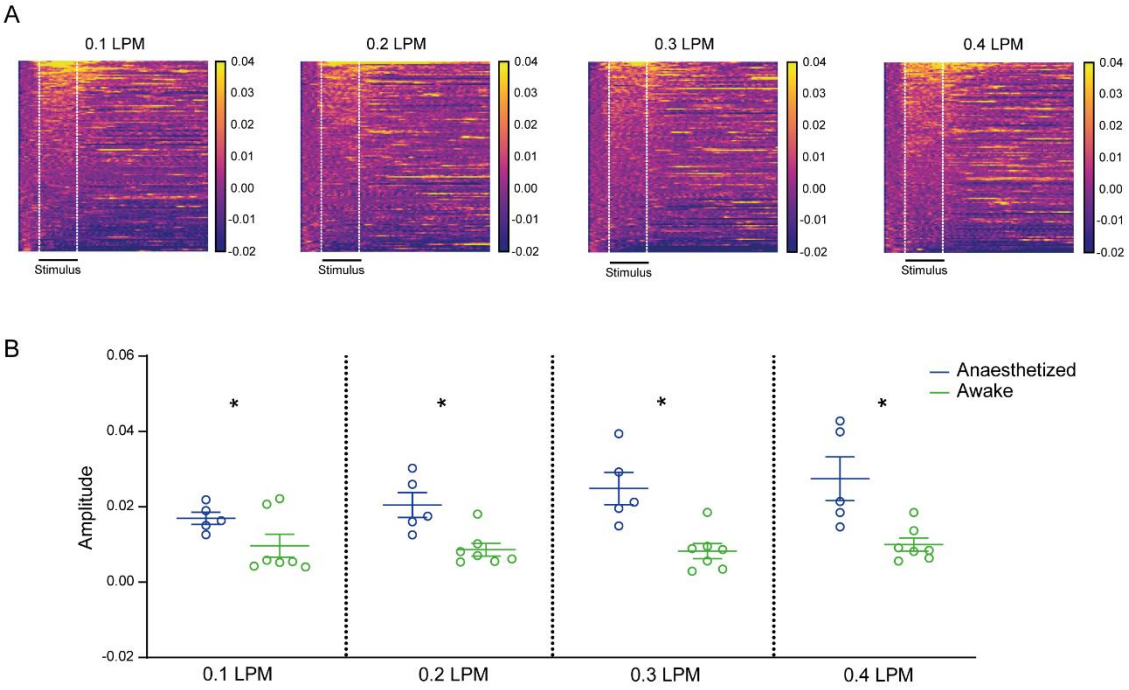

Figure 4-6 – Comparison of response kinetics of GAD 65 +ve OB interneurons under awake and anaesthetised conditions

A) Pseudo-colour heatmaps of Ca2+ dynamic responses elicited by various airflows. Data were collected from 7 mice, with 20 trials for each airflow. Data from all trials are sorted in decreasing order of Ca2+ response during airflow application.

B) The graph comparing the amplitude of calcium responses under awake and anaesthetized conditions. For all airflows the amplitude in awake conditions was significantly lower than that in the anaesthetized condition (one-tailed unpaired t-test, $p < 0.05$, $n_{anaesthetized} = 5$, $n_{awake} = 7$).

4.3.2. Learning-dependent refinement of the GAD 65 interneuron calcium activity

Since we observed that GAD 65+ve interneurons elicited activity in both awake and anaesthesized states, we investigated the effect of airflow discrimination learning on interneuronal activity. To accomplish this, we trained these animals to discriminate between 0.5 and 0.4 LPM while simultaneously recording their calcium traces. At the start of each task, imaging for 40 trials (20 S+ and 20 S-) were performed, and this was continued until the animals reached the asymptotic phase of learning (1200 trials - 4 tasks). The animals began with chance accuracy and improved to more than 80% accuracy by the end of the training (Figure 4-7A).

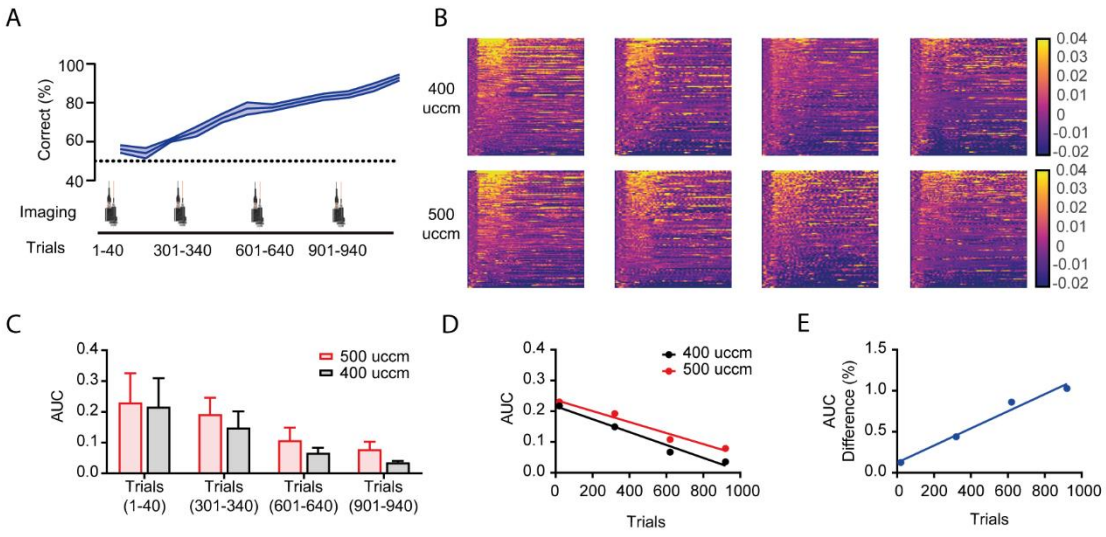

Figure 4-7 – Airflow learning dependent refinement of OB specific GAD 65+ve interneuronal activity

A) The learning curve representing accuracy of performance as the training progress. The solid line shows the average accuracy of all animals, while the shaded area shows the standard error of the mean. Additionally, schematic for the imaging schedule of the experiment is provided.

B) Pseudo-colour heatmaps of Ca2+ responses elicited by 0.4 and 0.5 LPM for different tasks. Data were collected from 5-6 mice, with 20 trials for each airflow. The heatmaps show a potential refinement in the Ca^{2+}transiets with learning. Data from all trials are sorted in decreasing order of Ca2+ response during airflow application.

C) Bar graphs representing average AUC of animals for 0.4 and 0.5 LPM for different tasks. As learning progressed, the AUC for both airflows decreased.

D) Plot representing change in average AUC of animals for 0.4 and 0.5 LPM with number of trials. y-axis represents AUC whereas x-axis represents number of trials. For both airflows, change in average AUC showed an inverse correlation with learning. (0.4 LPM: r = -0.9862, R^2 = 0.9726, p = 0.0138, 0.5LPM: r = -0.9816, R^2 = 0.9636, p = 0.0184, n = 5-6 mice)

E) Plot representing difference in average AUC of animals between 0.4 and 0.5 LPM with number of trials. y-axis represents AUC difference whereas x-axis represents number of trials. The difference in AUC correlated positively with number of trials. (r = 0.9879, R^2 = 0.9759, p = 0.0121, n = 5-6 mice).

Qualitative analysis of pseudo heatmaps revealed that both airflows elicited responses in the interneurons throughout the training session, and learning refinement in activity for both airflows was observed (Figure 4-7B). To quantify these refinements further, area under the curve (AUC) was used (Figure 4-7C). The initial AUC for both airflows were high, but they refined as the learning progressed. The AUC for both airflows showed inverse correlation with the number of trials, which serves as a proxy for learning progression (Figure 4-7D, AUC: 0.4LPM: Task1 – 0.2168 ± 0.0927, Task 2 – 0.1492 ± 0.0527, Task 3 – 0.0667 ± 0.0168, Task 4 – 0.0356 ± 0.0045; r = -0.9862, R^2 = 0.9726, p = 0.0138, 0.5LPM: Task1 – 0.2301 ± 0.0958, Task 2 – 0.1922 ± 0.0536, Task 3 – 0.1077 ± 0.0409, Task 4 – 0.0789 ± 0.0239; r = -0.9816, R^2 = 0.9636, p = 0.0184). Further, the AUC difference between for both airflows increased as the number of trials increased, implying a positive correlation (Figure 4-7E, AUC difference: r = 0.9879, R^2 = 0.9759, p = 0.0121). These findings provide novel insights into the learning dependent olfactory bulb associated mechanisms of airflow information processing.

4.3.3. Optogenetic modulation of GAD 65 expressing interneurons alters airflow discrimination behaviour

Since we previously demonstrated that OB is involved in processing of the airflow stimuli and learning of the airflow discrimination correlated with refinement in the GAD 65 +ve interneuron activity, we wanted to investigate whether modulating the activity of these neurons influences airflow discrimination learning. To accomplish this, we used an optogenetic approach to modulate the activity of GAD 65-expressing interneurons in a bidirectional manner using ChR2 and Arch expressed specifically in GAD 65 +ve interneurons. As GAD 65 interneurons comprise ~78% of total interneuron population in OB (259), this experiment investigated how overall OB inhibition affected airflow discrimination behaviour.

The animals (three groups: Gad 65-Arch, GAD 65-ChR2, and GAD 65-EYFP (control)) were first trained to discriminate 0.5 vs. 0.4 LPM in the absence of photoactivation. All three groups of animals demonstrated comparable learning abilities, ruling out the possibility that one group is inherently faster than the others (Figure 4-8A, two-way ANOVA: 0.5 vs. 0.4 LPM; F (22,400) = 0.9010, p = 0.5939). Further, learned animals (last task) did not show any difference in the time taken to discriminate this airflow pair and their sniffing frequencies were similar (Figure 4-8B and 8C, DTs: GAD 65-Arch – 387.3 ± 17.25, GAD 65-ChR2 – 370.0 ± 18.68, GAD 65-EYFP -379.7 ± 18.61, one-way ANOVA, F = 0.962, p =

0.8228; SF: GAD 65-Arch – 4.924 ± 0.1294, GAD 65-ChR2 – 4.828 ± 0.1582, GAD 65-EYFP -4.919 ± 0.1627, one-way ANOVA, F = 0.1130, p = 0.8935), confirming that all groups have comparable sampling strategies and airflow discrimination abilities. The animals were then trained on 0.15 vs. 0.1 LPM under photoactivation ON conditions. We observed faster learning when GAD 65-expressing interneurons were inhibited by Arch stimulation and slower learning when ChR2 was stimulated (Figure 4-8A, two-way ANOVA with Tukey's multiple comparison test: * indicates p-value of <0.05). Despite learning differences, after 900 trials, the accuracies of control and Arch animals were similar; however, the accuracies of ChR2 animals were still very low. These differences in final performance were reflected in the DTs, with DTs for ChR2 significantly higher than for both groups (Figure 4-8B, GAD 65-Arch – 384.3 ± 21.48, GAD 65-ChR2 – 661.5 ± 104.8, GAD 65-EYFP – 385.3 ± 15.75, one-way ANOVA with Tukey's multiple comparison test, F = 10.57, p = 0.0003). Furthermore, sniff frequencies during the DTs were also comparable for all groups (Figure 4-8C, GAD 65-Arch – 5.110 ± 0.1129, GAD 65-ChR2 – 4.735 ± 0.2449, GAD 65-EYFP – 5.241 ± 0.0912, one-way ANOVA, F = 3.009, p = 0.0627), indicating that these differences in performance are not due to differences in sampling parameters but rather to differences in information processing in OB.

To ensure that the observed bidirectional modulation of airflow discrimination behaviour is very specific to photoactivation conditions, we trained these animals again to a set of airflow pairs sequentially in light OFF and ON conditions. Specifically, animals were trained on 0.3 vs. 0.25 LPM under no light conditions, followed by 0.45 vs. 0.35 LPM under light ON conditions. As previously observed for no-light conditions, performance of animals was similar across different groups for 0.3 vs. 0.25 LPM (Figure 4-8A, two-way ANOVA: F (15,119) = 0.5933, p = 0.8753). Further, under no-light conditions, the DTs and sniff frequencies were comparable (Figure 4-8B and C, DTs: GAD 65-Arch – 395.1 ± 17.51, GAD 65-ChR2 – 373.8 ± 13.70, GAD 65-EYFP – 393.1 ± 17.09, one-way ANOVA, F = 0.3614, p = 0.6994; SF: GAD 65-Arch – 4.955 ± 0.1130, GAD 65-ChR2 – 5.373 ± 0.2513, GAD 65-EYFP – 4.936 ± 0.1857, one-way ANOVA, F = 1.546, p = 0.2281). However, when animals were trained on 0.45 vs. 0.35 LPM under photoactivation conditions, Arch animals performed better while Chr2 animals showed performance deficits. The learning accuracies of animals were better for Arch group as compare to ChR2 and control group. Even after 600 trials, while the accuracies of Arch and control group became similar, ChR2 group animals still showed lower accuracies (Figure 4-8A, two-way ANOVA with Tukey's multiple comparison test: * indicates p-value of

<0.05). DTs for the ChR2 group were significantly higher, as previously observed, while there was no difference in sniff frequency (Figure 4-8B and C, DTs: GAD 65-Arch – 370.1 ± 11.65, GAD 65-ChR2 – 652.8 ± 105.7, GAD 65-EYFP – 363.4.3 ± 12.04, one-way ANOVA with Tukey's multiple comparison test, $F = 12.42$, $p < 0.0001$; SF: GAD 65-Arch – 5.177 ± 0.1873, GAD 65-ChR2 – 5.386 ± 0.3033, GAD 65-EYFP – 5.181 ± 0.0951, one-way ANOVA, $F = 0.3330$, $p = 0.7191$). Despite the initial differences in learning pace between the Arch and EYFP groups under light ON conditions, their accuracies were comparable at the end of the task. As a result, we investigated what happens to the DT between these groups when the accuracies were greater than 80%. We combined all tasks with accuracies greater than 80% for all the airflow pairs under light ON conditions and compared the corresponding DTs between these two groups. We found that the Arch group has significantly faster DT (Figure 4-8D1 and D2, K-S D-value = 0.256, $p = 0.0157$) than the control group, but there is no difference in task accuracies between these two groups (K-S D-value = 0.0848, $p = 0.9532$).

To ensure that animals are making decisions in response to airflows, however not using any non-specific cues, we extended our training and asked these animals to distinguish between 0.6 and 0.6 LPM. For all groups of animals, their accuracy was always around the chance level (Figure 4-8A), ruling out the possibility of animals using any additional cue to discriminate the airflows. Together, these findings show that altering the activity of GAD 65 +ve interneurons while animals perform the task can modulate their airflow discrimination behaviour.

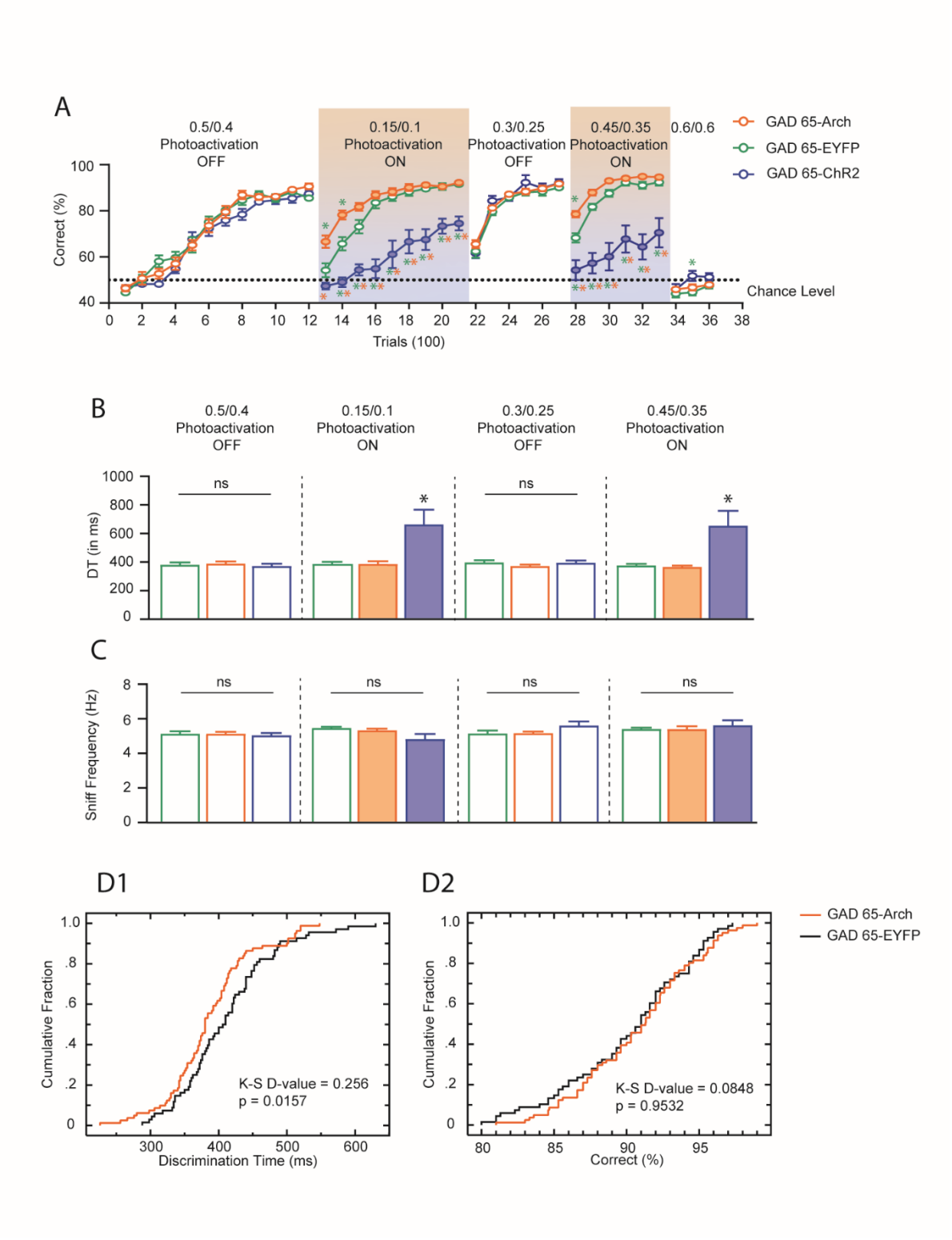

Figure 4-8 – Airflow discrimination behaviour is altered by optogenetic modulation of GAD 65 expressing interneurons

A) Learning curves representing performance accuracy for various airflow pairs under different photoactivation conditions. Animals were trained in the following order: 0.5 vs. 0.4 LPM (1200 trials - Light OFF), 0.15 vs. 0.1 LPM (900 trials - Light ON), 0.3 vs. 0.25 LPM (600 trials - Light

OFF), 0.45 vs. 0.35 LPM (600 trials - Light ON), 0.6 vs. 0.6 LPM (600 trials - Light ON). Animals learnt faster when GAD 65 expressing interneurons were stimulated with Arch, whereas a deficit in learning occurred for ChR2 activation. (Two-way ANOVA with Tukey's multiple comparison test: * represents $p < 0.05$).

B) Bar graphs representing average DTs for all groups of animals for various airflows under different photoactivation conditions. The DTs of animals under photoactivation conditions for ChR2 group was slower compared to other groups of animals. (One-way ANOVA with Tukey's multiple comparison test * represents $p < 0.05$).

C) Bar graphs representing average sniff frequencies for all groups of animals during discrimination time for various airflows under different photoactivation conditions. No differences in the SF for all the groups under different photoactivation conditions were observed. (One-way ANOVA with Tukey's multiple comparison test * represents $p < 0.05$).

D) D1) Cumulative fraction representing the frequency corresponding to a specific DT for different groups. Orange line represents cumulative fraction of DTs for GAD 65-Arch group, whereas black line represents the same for GAD 65-EYFP group. Under photoactivation conditions Arch animals made faster decisions. (K-S D-value = 0.256, p = 0.0157).

D2) Cumulative fraction representing the frequency corresponding to a specific accuracy for different groups. Orange line represents cumulative fraction of accuracies for GAD 65-Arch group, whereas black line represents the same for GAD 65-EYFP group. The accuracy of both groups of animals were similar. (K-S D-value = 0.0848, p = 0.9532).

4.3.4. Optogenetic modulation of odour-based discrimination behaviour

The canonical function of olfactory system is processing the odour-related information. As we observed differences in learning behaviour of animals for airflow-based discrimination tasks when OB specific inhibitory interneurons were optogenetically modulated, we wanted to investigate the influence of this modulation on odour-based discrimination tasks as well. This was accomplished by training the animals on a complex odour discrimination task in which they were asked to distinguish between a 60-40 binary mixture of octanol (+) and octanol (-) enantiomers under photoactivation ON conditions. During the odour-based discrimination task, Arch animals learned at a slower rate, whereas ChR2 animals learned faster. Even after 600 trials, Arch animals showed their performance deficit (Figure 4-9A, two-way ANOVA with Tukey's multiple comparison test: * indicates p-value of <0.05). The DTs measured were significantly slower for Arch animals (Figure 4-9B, GAD 65-Arch – 531.2 ± 64.92, GAD 65-ChR2 – 374.5 ± 8.087, GAD 65-EYFP – 329.8 ± 11.87, one-way ANOVA with Tukey's

multiple comparison test, F = 6.418, p = 0.0047). Unlike what was observed with airflow-based learning, sniff frequencies of different groups of animals did not remain consistent during this task. ChR2 group showed higher sniff frequencies (Figure 4-9C, GAD 65-Arch – 4.632 ± 0.1533, GAD 65-ChR2 – 5.313 ± 0.1987, GAD 65-EYFP – 4.511 ± 0.2567, one-way ANOVA with Tukey's multiple comparison test, F = 3.312, p = 0.0497).

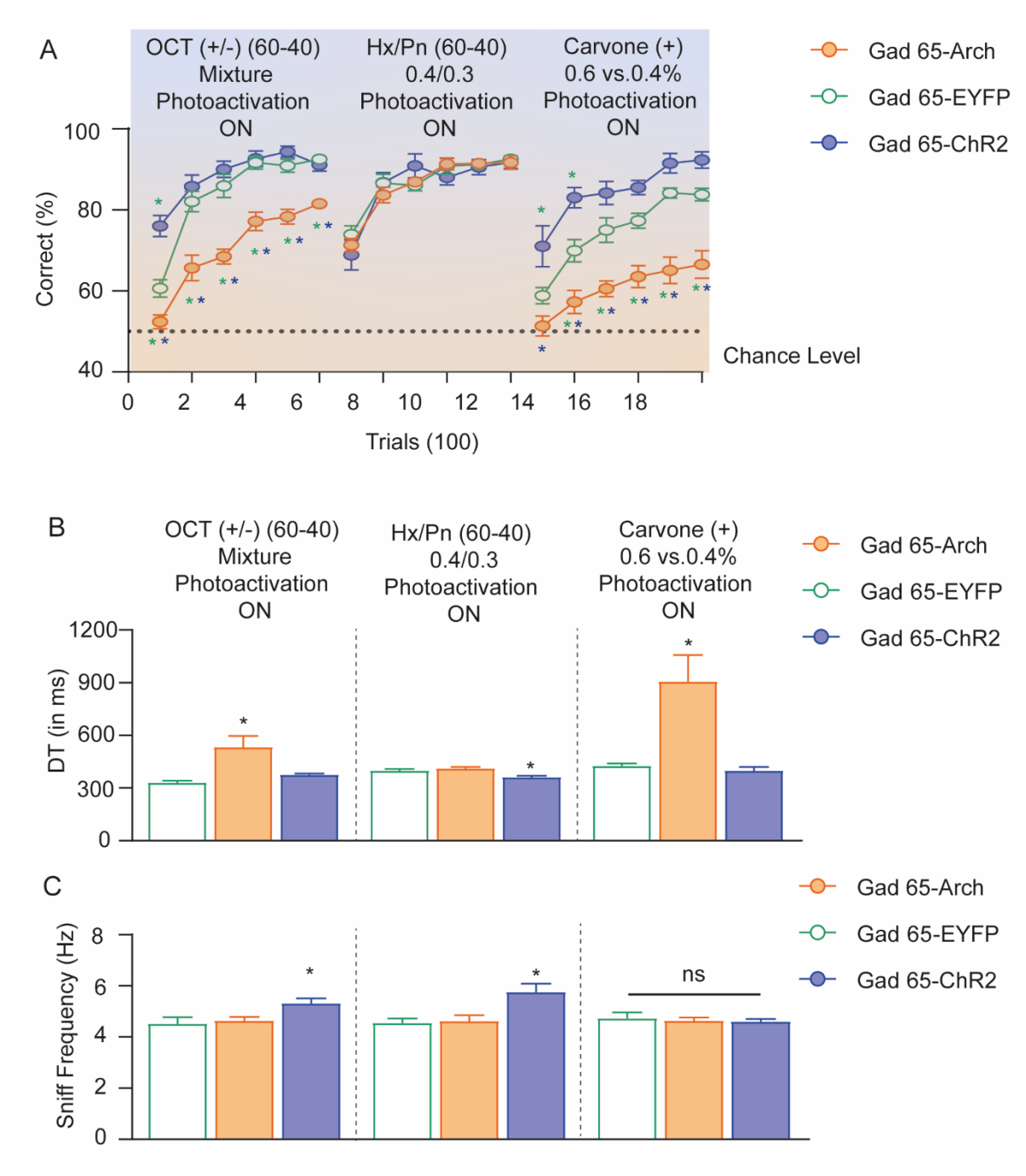

Figure 4-9 – Odour-based discrimination behaviour is altered by optogenetic modulation of GAD 65 expressing interneurons

A) Learning curves representing animal accuracy for various odour-based tasks using same/different airflow rates. Animals were trained in the following order: Octanols (+)/(-) – 60-40 mixture (600 trials - Light ON), Hx/Pn – 60-40 mixture – 0.4/0.3 LPM (600 trials - Light ON), Carvone (+) 0.6 vs. 0.4 % (600 trials – Light ON). Two-way ANOVA with Tukey's multiple comparisons. (* represents $p< 0.05$).
B) Bar graphs representing average DTs for all groups of animals for various odour-based tasks. One-way ANOVA with Tukey's multiple comparisons. (* represents $p< 0.05$).
C) Bar graphs representing average sniff frequencies during discrimination time for all groups of animals for various odour-based tasks. One-way ANOVA with Tukey's multiple comparisons. (* represents $p< 0.05$).

As the optogenetic modulations for odour-based discrimination task provided contrasting behavioural readouts compared to airflow-based discrimination task, we investigated how altering both components i.e. different airflows and odours for rewarded and non-rewarded stimuli, would influence their learning abilities on optogenetic modulations. We trained all three groups of animals to discriminate a complex mixture of hexanal and pentanone under light ON conditions, with one stimulus coupled to one airflow (Hx/Pn (60-40) - 0.4 LPM and Pn/Hx (60-40) - 0.3 LPM). The results revealed no difference in learning across groups (Figure 4-9A, two-way ANOVA: $F (10,180) = 0.9290$, $p = 0.5078$), indicating that altered combination of both stimuli may have rescued the learning deficit caused, when only one stimulus was used (odour- or airflow-based learning). For ChR2 group reduction in DTs, and increase in sniff frequencies was observed (Figure 4-9B and C, DTs: GAD 65-Arch – 410.3 ± 10.64, GAD 65-ChR2 – 360.6 ± 8.941, GAD 65-EYFP – 397.2 ± 11.68, one-way ANOVA with Tukey's multiple comparison test, $F = 4.045$, $p = 0.054$; SFs, GAD 65-Arch – 4.617 ± 0.2365, GAD 65-ChR2 – 5.749 ± 0.3345, GAD 65-EYFP – 4.544 ± 0.1781, one-way ANOVA with Tukey's multiple comparison test, $F = 6.521$, $p = 0.0043$). Since combining different odour stimuli with different airflows can result in concentration differences, we trained animals on a concentration-based task to see if this phenotype was caused by animals relying on different concentrations as cue. We trained animals to discriminate 0.6 vs 0.4 percent concentration of carvone (+) under light ON conditions. Concentration discrimination was found to be very similar to odour discrimination, with the Arch group showing a learning deficit and the ChR2 group learning faster (Figure 4-9A, two-way ANOVA with Tukey's multiple comparison test: * indicates p-value of <0.05). For this task, Arch animals showed slower DTs (Figure 4-9B, GAD 65-Arch – 905.5 ± 151.8, GAD 65-ChR2 – 397.3 ± 23.22, GAD 65-EYFP – 425.0 ± 15.63, one-way ANOVA with Tukey's multiple comparison test, $F = 7.558$, $p =$

0.0025), which was consistent with previous finding of odour-discrimination, but there was no difference observed in sniffing frequencies (Figure 4-9C, GAD 65-Arch – 4.632 ± 0.1312, GAD 65-ChR2 – 4.594 ± 0.1081, GAD 65-EYFP – 4.726 ± 0.2395, one-way ANOVA, $F = 0.1159$, $p = 0.8910$). The task-dependent variations in sniffing that we observed for ChR2 group in case of olfaction-based discriminations need further investigations on the possible communication between respiratory and olfactory centres.

4.4. Discussion

Although there have been studies that observed OB activity (mostly presynaptic, arising from OSNs) in response to mechanical stimuli, no study has been able to address the neural mechanisms underlying these responses. To begin, we used c-fos staining in mice performing airflow discrimination behaviour. The highest activation of GAD 65 +ve interneurons in GCL was revealed by c-fos staining. These findings compelled us to look into the role of the OB interneuronal population in airflow-based discrimination behaviour. We used in-vivo calcium imaging to examine the activation of these GAD 65+ve GCL interneurons in response to airflows in both awake and anaesthesized conditions. While these interneurons elicited activity for airflows in both conditions, the activity of interneurons in the anaesthetized state was significantly higher than that in the awake state. Although similar granule cell responses to odours have previously been recorded in both awake and anaesthetized states, our findings were consistent with these observations that the peak amplitude of granule cells is lower in the awake state (260). Since these interneurons modulate the activity of M/T cells, which are the bulb's output neurons, our findings show that the degree of reformatting of M/T cell ensembles varies for different airflows and also between awake and anaesthetized states, thereby influencing airflow-information processing. The decreased amplitude in the awake state may be a result of the recruitment of non-responsive M/T cells during passive sensory exposure (261). Further, it has been demonstrated that repeated odour exposure reduces both excitatory and inhibitory M/T cell responses as well as dynamic reformatting of ensemble odour representations (260,261). This plasticity obtained through activity refinement improves pattern separation, which aids odour discrimination during active learning (260). To investigate how responses of GAD 65 +ve interneurons shape with airflow discrimination learning, we trained the animals to distinguish between two airflows while simultaneously recording their calcium activity. We discovered a similar pattern, in which the interneurons showed inverse correlation with learning, confirming a learning-dependent refinement in the interneuron population activity and thereby in the output from OB.

4.4.1. Airflow and odour discrimination behaviour are differentially modulated by optogenetic manipulations of interneurons.

To better understand the role of synaptic inhibition in airflow information processing, we optogenetically modulated the activity of OB GABAergic interneurons in a bidirectional way. This was accomplished by expressing light-gated archaerhodopsin (Arch) and channel

rhodopsin (ChR2) channels under the GAD 65 promoter, which allows optical stimulation of these neurons with high spatial and temporal resolution. While Arch causes cell hyperpolarization, ChR2 activates cells by depolarizing them (262–265). Optogenetic inhibition of interneurons (GAD 65-Arch group) improved learning in an airflow discrimination task, whereas stimulating these neurons (Gad 65 ChR2 group) resulted in an airflow discrimination performance deficit. These differences in the performance was also reflected in the discrimination times of the animals. The internal control experiment with two different airflows in the absence of photoactivation ensured that the effect we observed was very specific for optogenetic modulations. Furthermore, when we trained these animals on an odour discrimination task, the optogenetic modulations produced opposing phenotypes. While increased inhibition resulted in poor performance on airflow tasks, it resulted in improved learning on odour-based tasks (odour discrimination as well as concentration discrimination task). Our findings that an increase in synaptic inhibition of OB circuits by optogenetic modulation of interneuronal activity improves odour-based discrimination learning were in line with previous research (254,266). The contrasting phenotype observed suggests that the optimal inhibition required for refining odour and airflow information varies. Our hypothesis is supported by the previously observed broader activation patterns in OB towards airflow stimuli compared to odours (14,77). Although our findings demonstrate the neural mechanisms underlying OB-mediated mechanical information processing, further experiments are needed to investigate the optimal inhibition required to process and refine airflow vs. odour information.

4.4.2. Multimodal information processing by olfactory system

As we observed contrasting phenotypes for airflow- and odour-based discrimination tasks, we investigated how the interaction of the two stimuli would alter animal's behavioural readouts. To accomplish this, we trained animals in a multimodal discrimination task under photoactivation conditions, where one odour was coupled with one airflow, which acted as a single stimulus. Surprisingly, all three groups of animals performed similarly in these conditions. Specifically, when two stimuli were presented together as combined, the deficits observed for ChR2 and Arch groups in airflow- and odour- discriminations, respectively, were rescued. The increase in performance of animals observed when two coherent stimuli are presented simultaneously is known as the principle of multi-sensory enhancement. However, multisensory enhancement is more relevant when subthreshold levels of sensory stimuli

corresponding to two different sensory systems are presented (267–281). Although the stimuli in our experiment are neither subthreshold nor corresponds to two different sensory systems, we do observe rescue or enhancement in the learning phenotype, pointing towards the possibility of stimuli interacting and leading to the formation of a multimodal percept aided by the olfactory bulb circuitry. These findings not only provide insights into potential neural mechanisms underlying multimodal information processing, but also serve as a platform for studying multimodal decision making using only a single sensory system.

4.4.3. Differential sampling strategies for airflow and odour driven behaviour under different optogenetic conditions.

Active respiration is known to synchronise the activity of M/T cells, indicating that there is a close relationship between respiration and intrinsic OB activity (282–285). Respiration-driven intrinsic M/T cells and cortical responses have been shown to be associated with the regulation of cognitive functions (284,286,287). With this information and our results, which showed differential sampling dynamics for airflows and odours in the previous chapter, it can be hypothesised that M/T cell activity for airflows and odours may follow distinct patterns. Furthermore, using optogenetic modulation of inhibitory interneuron activity, we observed stimulus-specific (airflow and odours) differences in discrimination learning and sniffing responses. For airflow discrimination tasks, all three groups (GAD 65-Arch, GAD 65-ChR2, and GAD 65-EYFP) had similar sniffing frequencies, whereas in odour and multimodal discrimination tasks, the breathing frequencies of the GAD 65-ChR2 group were significantly higher than the other two groups. It is well known that breathing synchronizes M/T cells activity (285), and M/T cell population exhibits greater decorrelation at higher frequencies, which aids in the discrimination of the odors (236,254). As a result, in the odor-based discrimination task, the ChR2 group, which displayed faster learning, exhibited the increased sniffing. Surprisingly, the sniffing frequencies of animals were comparable across three groups for concentration discrimination, even though the learning phenotype for this task was identical to that of odour discrimination and these observations need further investigations. Together, these findings establish a link between breathing and OB specific neural activity patterns associated with airflow- and odour-based discrimination tasks.

4.5. Future Directions

4.5.1. OB output neuron-specific mechanisms for airflow and odour information processing

This study demonstrates that optimal inhibition needed to refine airflow and odour information differs. Although we modulated M/T cells firing activity in this study by manipulating inhibitory interneurons in the OB, the results do not provide direct evidence of how M/T cells process these stimuli sensed by the olfactory system. Hence, it will be critical to study the neural activity of M/T cells towards airflow stimuli. To achieve this, we can make use of the cell-type-specific markers for M/T cells such as Pcdh-21 and Tbet-21. Using in-vivo calcium imaging to record and optogenetics to modulate the activity of M/T cells during airflow and odour-driven behaviours will help us better understand the neural mechanisms underlying 'multimodal' information processing through rodent olfactory system.

4.5.2. Cortical mechanisms underlying airflow vs. odour discrimination behaviour

As we have already demonstrated that information processing of airflow and odour stimuli differs in the OB, we further wish to investigate the cortical mechanisms underlying information processing for these two stimuli. The olfactory cortex comprises many brain regions that mainly includes the piriform cortex, orbitofrontal cortex, anterior olfactory nucleus, and olfactory tubercle (39). We have preliminary lab results that show differential c-fos activity in different olfactory cortical regions after animals learned to perform on discrimination tasks for airflows vs odours (Figure 4-10B C). The percentage of c-fos positive cells in the piriform cortex (Figure 4-10B1, B2, and C1) and anterior olfactory nucleus (Figure 4-10B1, B2, and C3) was higher for odours than for airflows, whereas the percentage of c-fos positive cells in the orbitofrontal cortex was higher for airflows (Figure 4-10B1, B2, and C2). Our long-term goal is to identify the cortical mechanisms underlying this processing, as these findings provide preliminary evidence of differential cortical activity for airflows and odours. One way to achieve this is by using in-vivo electrophysiology to collect data from these cortical areas while animals perform airflow and odour discrimination tasks.

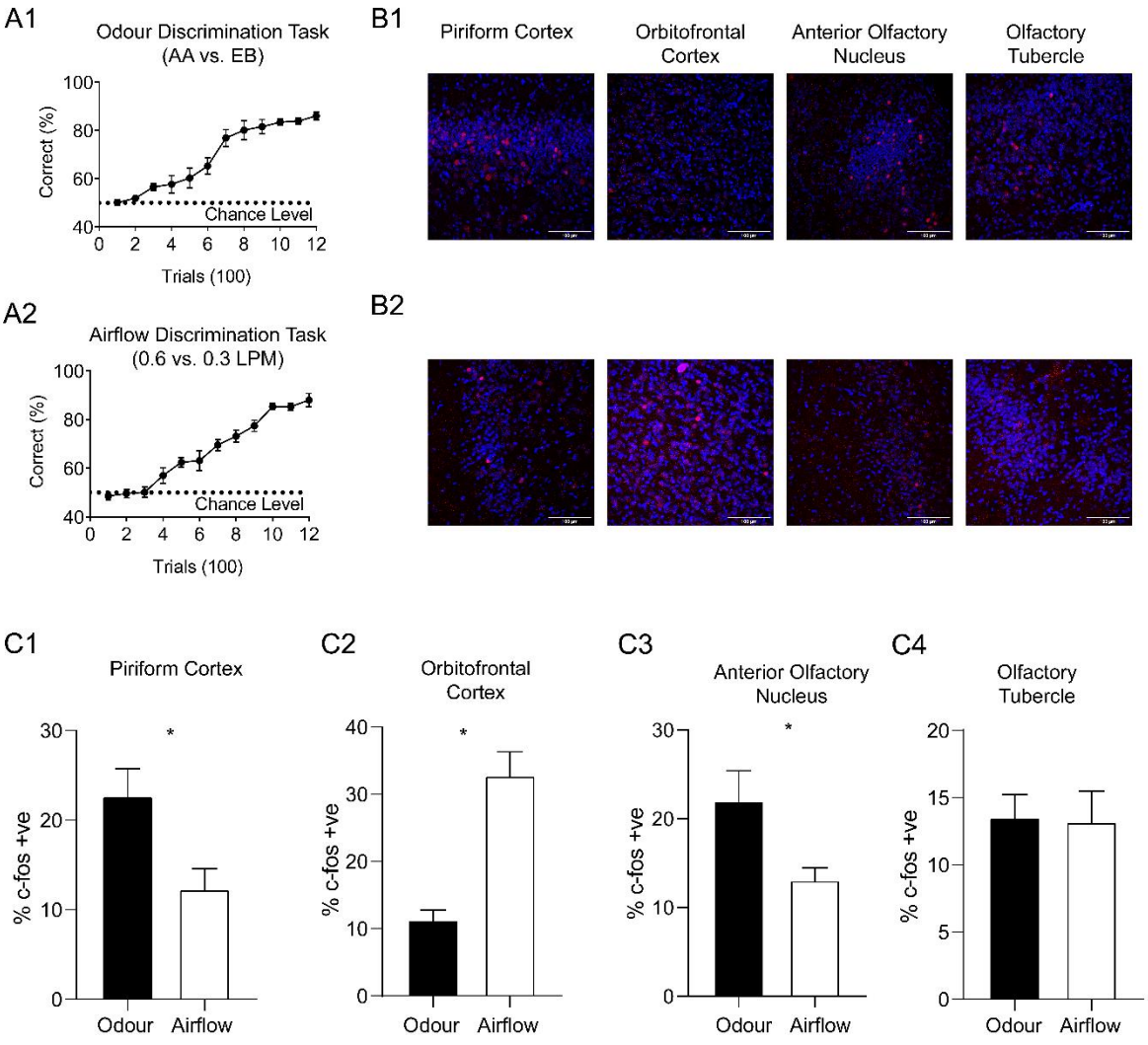

Figure 4-10 – Differential olfactory cortical activation in response to airflows and odours

A) A1) and A2) Learning curve representing the average accuracies of animals along with the number of trials for odour (AA vs. EB) and airflow (0.6 vs. 0.3 LPM) discrimination tasks, respectively.

B) B1) and B2) c-fos staining for piriform cortex, orbitofrontal cortex, anterior olfactory nucleus, and olfactory tubercle for odour and airflow discrimination tasks, respectively. Blue - DAPI staining, Red - c-fos staining.

C) C1) Percentage of c-fos positive cells in the piriform cortex for an airflow task is lower than that for an odour discrimination task (unpaired t-test $p = 0.0148$).

C2) Percentage of c-fos positive cells in the orbitofrontal cortex for an airflow task is higher than that for an odour discrimination task (unpaired t-test $p < 0.0001$).

C3) Percentage of c-fos positive cells in the anterior olfactory nucleus for an airflow task is lower than that for an odour discrimination task (unpaired t-test $p = 0.0238$).

C4) Percentage of c-fos positive cells in the olfactory tubercle for an airflow vs. odour discrimination task is similar (unpaired t-test p = 0.9087).

4.5.3. Functional relevance of 'multimodal' information processing through rodent olfactory system

Our findings suggest that there is a potential interaction between airflow and odour stimuli, which could alter olfactory perception and thus decision making. We confirmed this by training the animals on airflow, odour, and multimodal discrimination tasks at subthreshold levels. Animals were not able to perform and learn to discriminate airflows and odours alone at the subthreshold level, but their learning abilities were enhanced when the discrimination task was performed on multimodal stimuli combining both (Figure 4-11). Furthermore, we intend to address olfactory bulb-specific mechanisms underlying multimodal decision making through behavioural training, in-vivo calcium imaging, and optogenetics. As an initial step, experiments addressing the role of synaptic inhibition in multimodal information processing have already begun. Our preliminary results indicate the relevance of airflow information processing in the context of subthreshold odour discriminations that animals might be challenged to resolve in a highly dynamic olfactory environment.

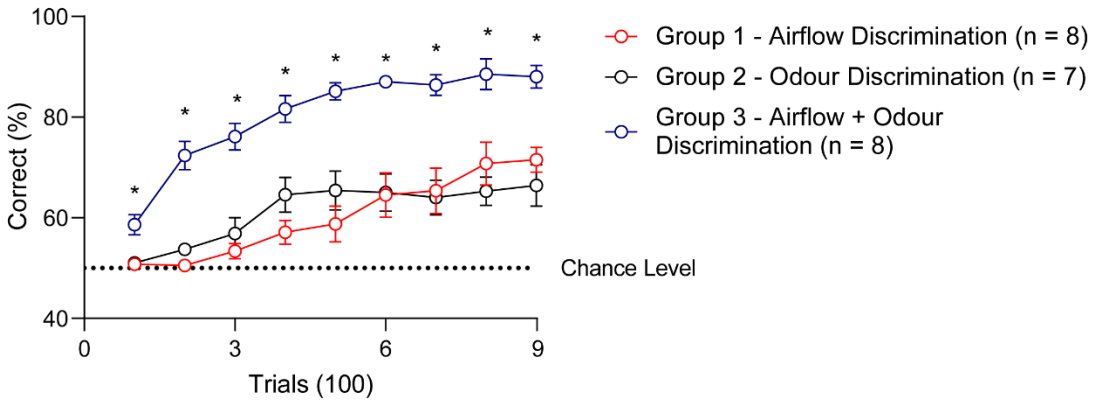

Figure 4-11 – Multimodal discrimination learning

The learning curve representing animals' discrimination abilities for airflows, odours, and multimodal (airflow + odour) stimuli. Animals that underwent multimodal discrimination performed better than unimodal groups at subthreshold levels of stimuli. (two-way ANOVA with Tukey's multiple comparison tests, * represents $p < 0.05$).

CHAPTER 5

A novel experimental strategy for assessing human sniffing behaviour during olfaction-based cognitive tasks

5.1. Introduction

Olfactory dysfunctions such as anosmia and hyposmia are known to be a common symptoms associated with several neurological disorders, including Parkinson's and Alzheimer's (43–47). Additionally, olfactory dysfunctions are also seen in several upper respiratory tract infections (48). Numerous investigations conducted since the beginning of coronavirus 2019 (COVID-19) pandemic have shown that anosmia/hyposmia is a common symptom among COVID-19 infected patients (48–52), and the olfactory dysfunctions remain persistent even after recovery from the infection (53–56). This highlights the essentiality of studying olfaction in health and disease.

Sniffing is the first step in odour information processing that can influence the olfactory perception. It is an active sensing system that permits odorant molecules to enter the nose and travel all the way through the nasal cavity to the olfactory epithelium (288,289). Breathing, in addition to facilitating olfactory perception, also has multiple physiological roles such as regulation of homeostasis, metabolism, satiety, brain activity, attention and memory (58–66,290). Studies on olfactory information processing, have shown that minute respiratory volume (defined as the volume breathed or expelled by a human lung in one minute) and the respiratory amplitude increase during odour sampling (66,291). Further, sniff volumes fluctuate in an inversely proportional manner with odorant concentration (292,293). However, information on how breathing patterns are modulated during olfactory decision making in healthy subjects and patients with olfactory dysfunctions remain less explored.

The aim of the experiments discussed in this chapter was building an apparatus capable of quantifying breathing patterns during olfactory decision-making and developing a framework to use this method under clinical settings. We accomplished this by integrating a thermocouple-based air sensor to our custom-built olfactory-action meter. The olfactory-action meter has already been demonstrated to be beneficial in exploring several facets of olfactory perception in both normal subjects and COVID-19 patients (49,56). Combining it with breath

sensor allowed us to assess human sniffing parameters while they were actively participating in olfactory detection and olfactory matching tasks with a temporal resolution as high as 30 ms. While the odour detection task is a simple sensory perception test, the olfactory matching task is a more cognitively challenging one. We observed robust respiratory dynamic patterns across all odorants, with increased inhalations found during odour presentation. Additionally, a considerable increase in different sniff metrics, which was consistent across all odorants. We further employed this method to investigate sniffing patterns in participants recovered from COVID-19, as they had been demonstrated to have persistent olfactory deficits (56).

5.2. Materials and Methods

5.2.1. Study Population

Our study included a total of 134 participants divided in separate cohorts of healthy and post-COVID-19 subjects (Subjects that were tested positive for COVID-19). The majority of the participants were recruited from the residential campus of the Indian Institute of Science Education and Research (IISER), Pune, INDIA.

Inclusion criteria for normal healthy subjects:

- Only healthy subjects who agreed to participate in the study were chosen.
- At the time of the study none of them reported to have any illness.
- All participants signed a consent form before taking part in the study.

Inclusion criteria for post-COVID-19 subjects:

- Subjects who tested positive for COVID-19 at some point (3-12 months before the start of the experiment) were included in the study.
- Only subjects who agreed to participate in the study were considered. Before they could participate, everyone had to sign a consent form.
- At the time of the study none of them reported to have any detectable health problems.

5.2.2. Setup design

The breathing patterns of humans during odour-based cognitive tasks were investigated using a custom-built olfactory action metre (OAM) coupled with a thermocouple air sensor. The apparatus delivers odorized air through a 12-channel glass funnel connected to a ventilator mask, where subjects inhaled various odours. Using an air pump coupled with a charcoal filter, the deodorised air was pumped into the olfactometer at a rate of 5 litres per minute. Using a metallic custom-built manifold, the air inside the olfactometer was split into eleven channels which were coupled with ten mini and one large mass flow controller (MFC) (Pnucleus Inc.). Functioning of MFCs were controlled by custom written LabVIEW scripts, which allowed the experimenter to control the onset of airflow and its rate from each MFC. When the trial began, the odour bottle got air input from mini MFCs. Simultaneously, the main (MFC) output was bifurcated to 10 channels through an array of solenoid valves, with one solenoid valve corresponding to one odour channel. The output air from the valve-controlled

channel was mixed with the odorized air from the odour bottle before entering the glass nozzle linked to a ventilator mask (Figure 5-1A).

The ventilator mask is customised to include a thermocouple-based air sensor (AWM2000, Honeywell Inc.) with an extended tube from the sensor opening in front of the nostril of the subjects. The signal from the breathing sensor is relayed to high frequency oscilloscopes (TBS 1052C, Tektronix) in real time. The signals were recorded as alternating current (AC) and direct current (DC) with a time resolution of 30 milliseconds. The raw DC traces were subjected to a threshold function, which converted all of the data to binary form. Both AC and DC data were used in order to quantify different parameters associated with the breathing behaviour (representative traces Figure 5-2A, B, and C). The AC and DC oscilloscopes were triggered and synced with help of a tone that served as a notification for the commencement of each trial.

5.2.3. Experimental Paradigms

Each session of the experiment lasted approximately 20 minutes. The experiment was intended to assess sampling strategies associated with olfactory detection and olfactory matching tasks. Both groups (healthy as well as post-COVID-19 subjects) were subjected to abovementioned tasks. Furthermore, respiratory responses were recorded while healthy volunteers completed an odour-detection test with varying concentrations of odorants.

5.2.3.1. Olfactory detection task

The participants (healthy as well as post-COVID-19 subjects) were instructed to perform an odour detection task. The detection task consisted of ten trials. Each trial started with a tone of 200 ms, and after 1000 ms, the odour was delivered, that lasted for 4000 ms (Figure 5-1B). The odour detection task comprised nine odours and a blank stimulus. The odours were obtained from Sigma Aldrich and had ~99% purity. All the odours used were monomolecular odorants and were diluted to 1% in mineral oil. Subjects were exposed to the stimulus in a pseudorandomized manner. The individuals were only required to press a response button if they detected the odour. Response window overlapped with that of the Inter trial interval (ITI). ITI of 13 seconds was provided between two consecutive trials. During the detection task, breathing responses were concurrently recorded. Following stimuli were used

for detection task: 1. Hexanol, 2. Benzaldehyde, 3. Octanal, 4. Iso Amyl Acetate (IAA), 5. Hexanal, 6. Octanol, 7. Geraniol, 8. Eugenol, 9. Ethyl Butyrate, and 10. Blank

5.2.3.2. Olfactory matching task

The healthy participants were instructed to perform an olfactory matching task. The odour matching task consisted of 20 trials. In this task, the odours recognised by the individuals in the detection test were presented as pairs. Each trial started with a tone of 200 ms, and after 1000 ms, Odour1 was delivered for 4000 ms. This was followed by an inter-stimulus interval (ISI). The individuals were assigned an ISI at random from 2.5s, 5s, 7.5s, or 10s. The ISI was followed by the administration of a second odour stimulus (Odour2) that also lasted for 4000ms. Following that, the individuals were given a 5-second window in which they had to evaluate whether stimulus 1 and stimulus 2 were same or different (Figure 5-1A and Figure 5-1C). The subjects were provided with a response console wherein they had to press the button corresponding to their decision i.e. same or different. The response window began with the commencement of the second stimulus, and individuals were able to register their responses during that time period as well. Hence, individuals had to make a judgement within 9 seconds after the start of the second odour, and failing to do so resulted in an incorrect trial. The trials in the olfactory matching tasks (odour 1 and odour 2: same or different trials) were presented in a pseudorandomized manner. While subjects were engaged in olfactory matching task, their respiratory responses were simultaneously recorded.

5.2.3.3. Olfactory detection task with varying concentrations

Breathing responses of healthy subjects performing a concentration-dependent odour detection task were also recorded. This task comprised 20 trials with five distinct odorants at varying concentrations presented in a pseudorandomized manner. The ITI between two consecutive trials was kept constant at 13 s. Five distinct odours (odours used: Benzaldehyde, Iso Amyl Acetate (IAA), Octanol, Eugenol, and Ethyl Butyrate) were used in this task, each with 4 different concentrations achieved by air dilution. (concentrations used: 50%, 30%, 16.75%, and 7.14%, v/v). For each concentration, the detection index was calculated as the fraction of correct trials.

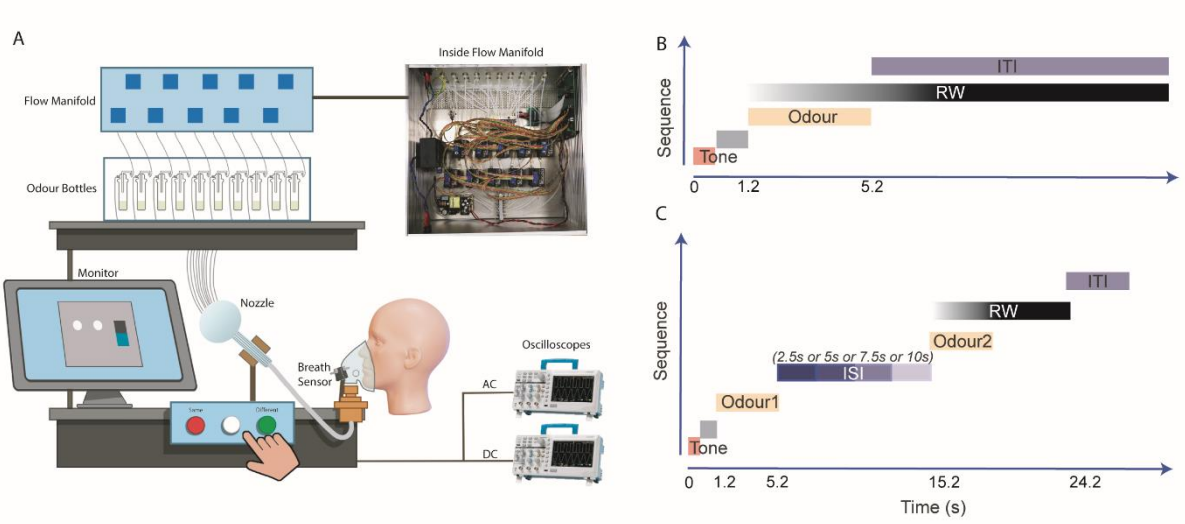

Figure 5-1 – Olfactory action meter and paradigm for olfactory detection and matching

A) A diagram depicting the various components of an olfactory action meter.

B) Illustration depicting the sequence of events in a single trial of an olfactory detection task over time. Each trial began with a tone of 200 ms, and after 1000 ms, the odour was delivered for 4000 ms. Individuals pressed a response button when they detected the odour. The response window and the inter trial interval overlapped (ITI). ITI of 13 seconds was provided between two consecutive trials. Breathing patterns were recorded concurrently with the detection task.

C) Illustration depicting the sequence of events in a single trial of an olfactory matching task over time. Each trial began with a tone of 200 ms, and after 1000 ms, Odour1 was delivered for 4000 ms. This was followed by an inter-stimulus interval (ISI). Individuals were assigned an ISI at random from 2.5s, 5s, 7.5s, or 10s. Following the ISI, a second odour stimulus (Odour2) was administered for 4000ms. Following that, the participants were given a 5-second window in which they had to determine whether stimulus 1 and stimulus 2 were the same or different and respond accordingly on the response console.

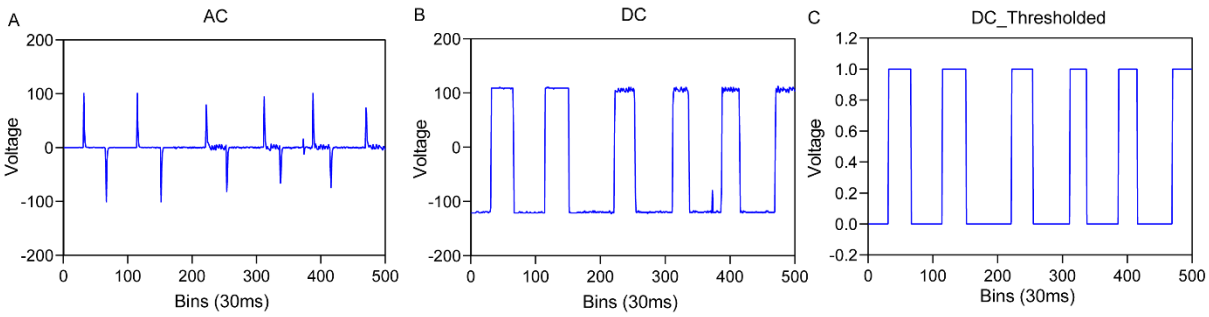

Figure 5-2 – Representative breathing traces

A) Representative breathing trace acquired from oscilloscope recording raw AC voltages for a single trial during odour detection task. The AC traces were used to quantify the inhalation and exhalation amplitudes.

B) Representative breathing trace acquired from oscilloscope recording raw DC voltages for a single trial during odour detection task. These traces were used for thresholding to obtain DC traces in panel C.

C) Representative breathing trace after thresholding of DC trace shown in panel B. These traces were used to quantify the sniffing frequencies and time spent for inhalation and exhalation.

5.2.4. Statistical analysis

GraphPad Prism 9, Microsoft Excel, and Python were used for all statistical analyses in this chapter. To determine p-values and test for statistical significance, we used the student's t-test, one-way and two-way ANOVA, and associated post-hoc tests.

5.3. Results

5.3.1. Sampling strategies of healthy subjects during odour detection

As the subjects (n = 71) performed an odour detection task, their breathing patterns were recorded. All odorants were detected by the individuals with greater than 85% accuracy. Subjects showed an enhanced sniffing during the odour presentation irrespective of the odorant used (Figure 5-3A and B, see Figure 5-4 for the quantification of different sniffing parameters). Additionally, the findings indicated that during the time when decisions were being made, the inhalation remained high, reached a peak, and then gradually decreased (Figure 5-3B). No increase in inhalation was noticed after the decision-making period. The robustness of the breathing strategy that participants use for smell detection was evidenced by similar sniffing behaviour even when the blank stimulus without any odour (1 blank stimulus in 10 trials presented in a random fashion) was presented to the subjects (Figure 5-3C).

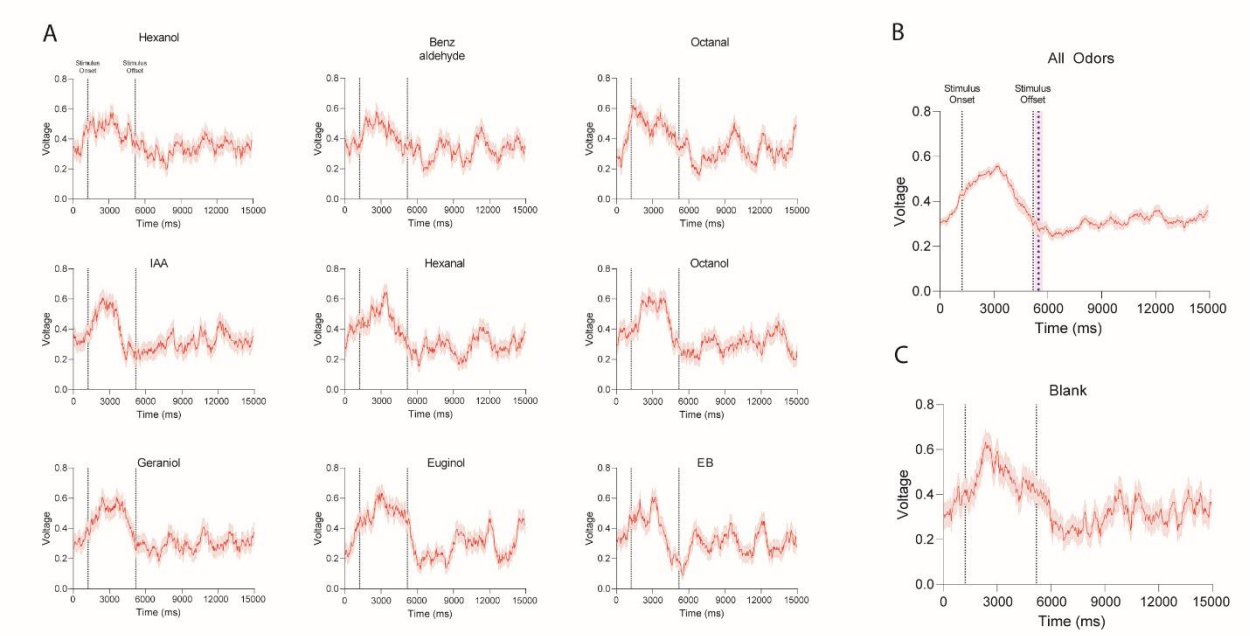

Figure 5-3 – Sniffing behaviour of healthy human subjects during odour detection task

A) Average of breathing traces of all the subjects for different odorants. The red line indicates the mean of the breathing traces of all subjects for a particular odour. The shaded region indicates the SEM. The two black dotted vertical lines represents the onset and offset of the stimulus (n = 71).

B) Average of breathing traces of normal human subjects across different odorants. The dotted magenta line represents the average of detection time, whereas the shaded area represents the SEM of detection time.

C) Average of breathing traces of all subjects for a blank stimulus.

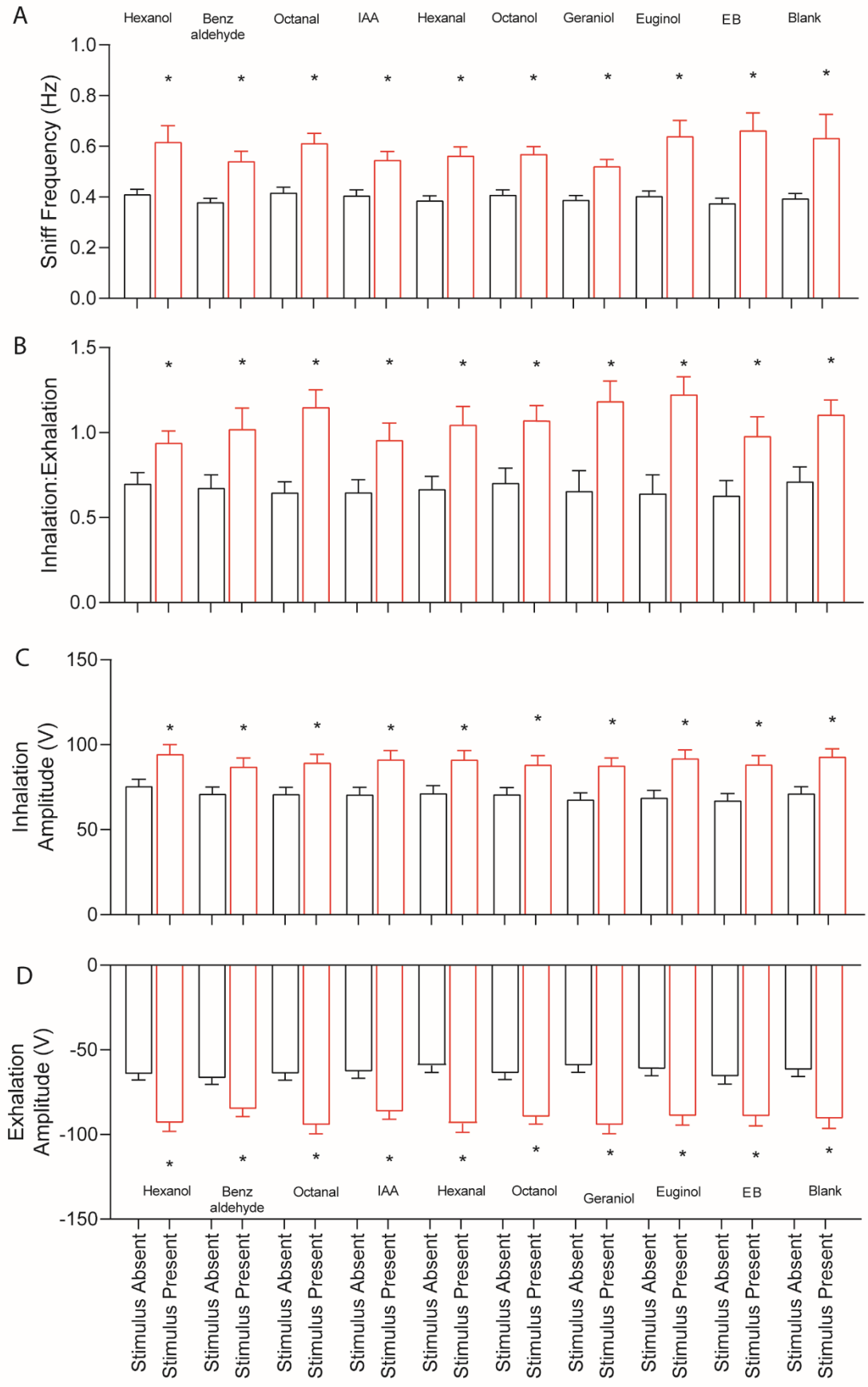
A
Hexanol
Benz aldehyde
Octanal
IAA
Hexanal
Octanol
Geraniol
Euginol
EB
Blank
Sniff Frequency (Hz)
1.0
0.8
0.6
0.4
0.2
0.0
B
Inhalation:Exhalation
1.5
1.0
0.5
0.0
C
Inhalation Amplitude (V)
150
100
50
0
D
Exhalation Amplitude (V)
0
-50
-100
-150
Hexanol
Benz aldehyde
Octanal
IAA
Hexanal
Octanol
Geraniol
Euginol
EB
Blank
Stimulus Absent
Stimulus Present

Figure 5-4 – Breathing parameters of healthy human subjects during odour detection task

A) Bar graph representing the average of sniffing frequencies of all subjects for different odorants in absence and in presence of stimulus. Sniffing frequencies for all odorants were significantly higher during the stimulus period. (paired t-test for all odorants, *indicates $p<0.05$, n = 71).
B) Bar graph representing the average of ratio of time spent in inhalation phase to that of time spent in exhalation phase for all subjects. The data is plotted for different odorants in absence and in presence of stimulus. The Inhalation: Exhalation ratio for all the odorants were significantly higher during the stimulus period. (paired t-test for all odorants, *indicates $p<0.05$, n = 71).
C) Bar graph representing the average of inhalation amplitudes of all subjects for different odorants in absence and in presence of stimulus. The inhalation amplitudes for all odorants were significantly higher during the stimulus period. (paired t-test for all odorants, *indicates $p<0.05$, n = 71).
D) Bar graph representing the average of exhalation amplitudes of all subjects for different odorants in absence and in presence of stimulus. The exhalation amplitudes for all odorants were significantly higher during the stimulus period. (paired t-test for all odorants, *indicates $p<0.05$, n = 71).

We further quantified different breathing parameters to better comprehend the breathing dynamics during the detection task. These metrics included the frequency of sniffing (the number of breaths taken in a second), the ratio of inhalation to exhalation time (Inhalation: Exhalation), and inhalation & exhalation amplitudes. The frequency of sniffing for all odorants increased significantly when the stimulus was presented compared to the absence of stimulus (Figure 5-4A: paired t-test for all odorants in absence and presence of stimulus, *indicates $p<0.05$). As sniffing frequency was seen to increase and since a sniff cycle comprises of inhalation and exhalation phases, we wanted to investigate how it influenced the dynamics of inhalation and exhalation. In order to do this, we computed the proportion of time spent by participants in the inhalation phase to that of the exhalation phase in the presence and absence of odour stimuli. A considerable increase in the ratio of inhalation to exhalation was seen during stimulus period regardless of the odour stimulus. We also measured the amplitudes of the inhalation and exhalation to assess the strength of the sniffing (Figure 5-4B: paired t-test for all odorants in absence and presence of stimulus, *indicates $p<0.05$). In addition, both the inhalation and exhalation amplitudes were considerably larger during the stimulus presentation for all odorants (Figure 5-4C and D: paired t-test for all odorants in absence and presence of stimuli, *indicates $p<0.05$). For the blank stimulus as well, similar sniffing parameters to those identified for odorants were observed (Figure 5-4). Participants behaved similarly to how they

did for the odours because they were unaware of the intermittent blank stimulus. These results highlight the reliability and robustness of the breathing strategies humans employ for olfactory sampling. Together, these findings show that individuals increase their sniffing frequency and inhalation amplitudes possibly to collect maximum odour molecules for executing an odour detection task successfully, and this was even evident in longer inhalations taken by the subjects while sampling the odorants.

5.3.2. Sniffing behaviour shown by healthy subjects during olfactory matching task

Following an odour detection task, subjects were asked to perform an olfactory matching (OM) task. In the olfactory matching task, participants are exposed to one odour, followed by an interstimulus interval (ISI), and then another odour (Figure 5-1C). The subjects were instructed to sample both odours and decide whether the two stimuli were the same or different. The odours used for the OM task only included the ones that participants had successfully detected during the detection test. OM tasks are more challenging as it included different processes such as detection, discrimination and olfactory working memory. We therefore wanted to study how humans' sample during an OM task and how varying durations of ISI affects sampling strategies. This was achieved by varying the ISI (2.5s, 5s, 7.5s, and 10s) across sessions and by recording the subjects' breathing patterns as they engaged in an OM task.

The individuals performed with a similar level of accuracy for various ISIs (Figure 5-5A1, Average accuracy: 2.5s – 55.67 ± 3.480, 5s – 49.20 ± 2.192, 7.5s – 51.43 ± 3.030, 10s – 53 ± 4.546, one-way ANOVA, $F = 0.9144$, $p = 0.4395$). The average accuracies of individuals for all ISIs were above the chance level (25.35%). The olfactory matching times (OMTs) of the subjects for the various ISIs was also unaltered, suggesting that the participants' capacity for olfactory matching is unaffected by the range of ISIs we have used (Figure 5-5A2, Average OMT: 2.5s – 5249 ± 136, 5s – 5361 ± 158, 7.5s – 5231 ± 225.5, 10s – 5929 ± 330.5, one-way ANOVA, $F = 1.529$, $p = 0.2128$). Additionally, the human sampling dynamics for the various ISIs remained consistent. For all ISIs, it was observed that the inhalation increased and peaked at the presentation of the first stimulus, then steadily decreased throughout the ISI before increasing once again afterwards during the presentation of second odour. The OMT for all ISIs were observed to be after the inhalation peak seen during the second odour, indicating that

olfactory matching decisions are followed by adequate sampling of second odour (Figure 5-5B).

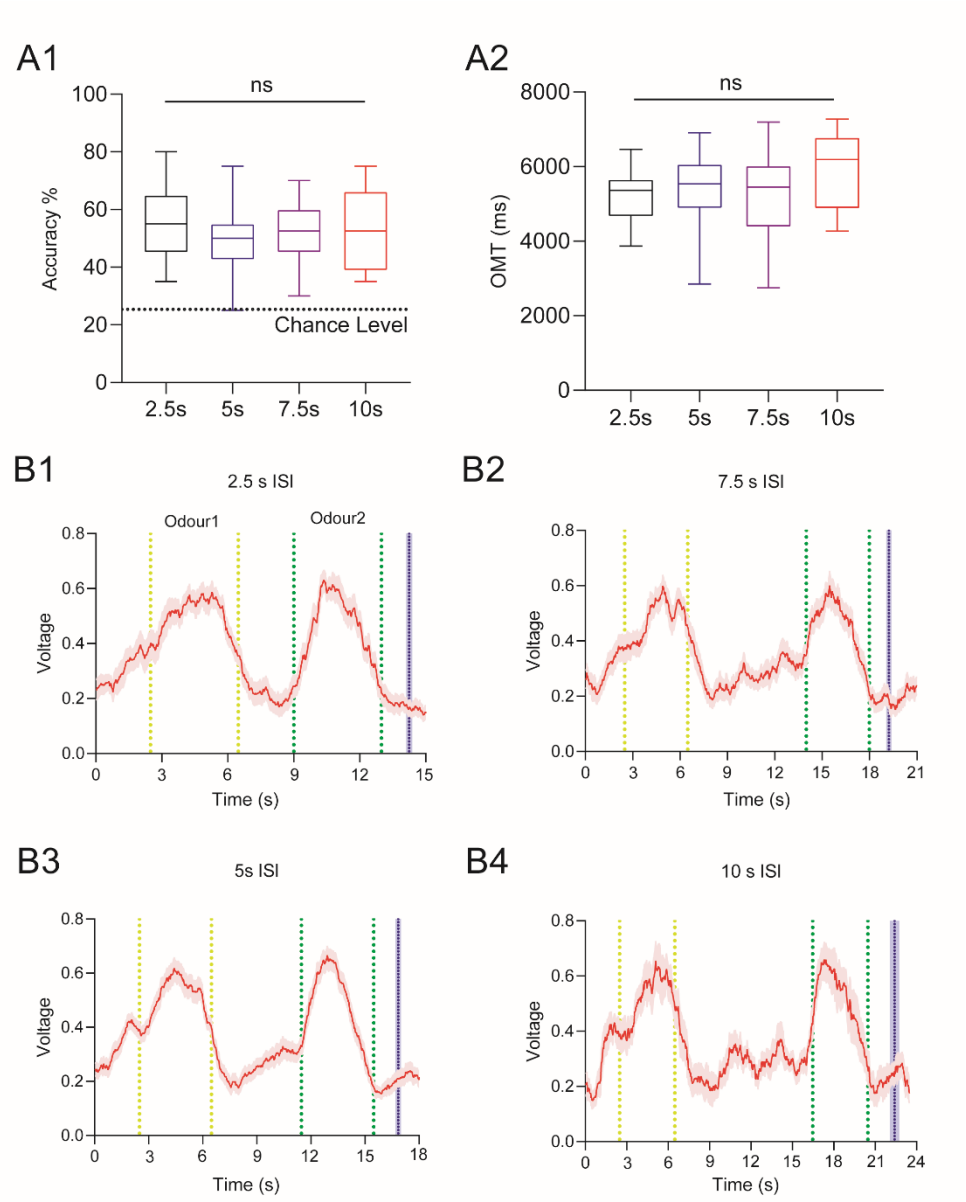

Figure 5-5 – Performance and breathing behaviour of healthy human subjects during olfactory matching task for different ISIs

A) A1) Box plots representing average accuracies of subjects for different ISIs. The average accuracies of subjects for different ISIs were similar. The chance level was 25.35%, based on the distribution of the "same" and "different" trials within a session. (one-way ANOVA, F = 0.9144, p = 0.4395, n_{total} = 71, total number of sessions for all ISIs = 89)

A2) Box plots representing average OMTs of subjects for different ISIs. The average OMTs of subjects for different ISIs were similar. (one-way ANOVA, F = 1.529, p = 0.2128, n_{total} = 71, total number of sessions for all ISIs = 89)

B) B1) Average of breathing traces of all the subjects for 2.5s ISI. The red line indicates the mean of the breathing traces of all subjects. The shaded region indicates the SEM. The yellow dotted vertical lines near 3-6s represents the onset and offset of the first stimulus. The green dotted vertical lines followed by ISI represents the onset and offset of the second stimulus. The vertical magenta line after the offset of second stimulus represents the average of OMT. The shaded area represents the SEM. ($n_{2.5s}$ = 24).

B2) Average of breathing traces of all the subjects for 7.5s ISI. ($n_{7.5s}$ = 24).

B3) Average of breathing traces of all the subjects for 5s ISI. (n_{5s} = 33).

B4) Average of breathing traces of all the subjects for 10s ISI. (n_{10s} = 10).

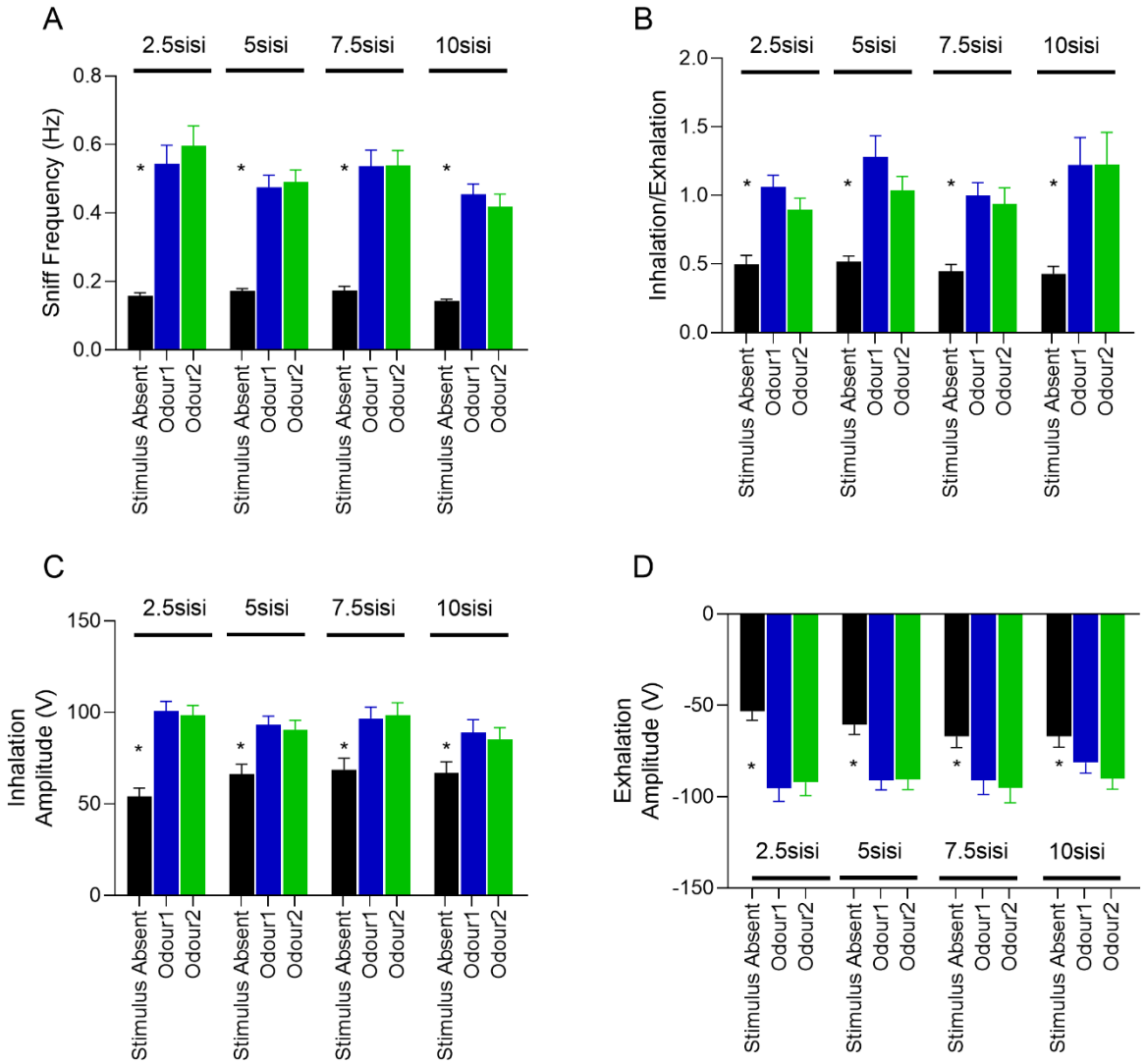

Figure 5-6 – For an olfactory matching task, all breathing parameters were significantly higher in presence of stimulus (odour1 and odour2) than in its absence

A) Average sniff frequencies of subjects for different ISIs under different stimulus conditions. For all ISIs sniff frequency in the absence of stimulus was significantly lower than that of observed for odour1 and odour2. (one-way ANOVA with Tukey's multiple comparison, *indicates $p<0.05$).
B) Average inhalation to exhalation ratio of subjects for different ISIs under different stimulus conditions. For all ISIs, the inhalation to exhalation ratio in the absence of stimulus was significantly lower than that of observed for odour1 and odour2. (one-way ANOVA with Tukey's multiple comparison, *indicates $p<0.05$).
C) Average inhalation amplitude of subjects for different ISIs under different stimulus conditions. For all ISIs the inhalation amplitude in the absence of stimulus was significantly lower than that of observed for odour1 and odour2. (one-way ANOVA with Tukey's multiple comparison, *indicates $p<0.05$).
D) Average exhalation amplitude of subjects for different ISIs under different stimulus conditions. For all ISIs the exhalation amplitude in the absence of stimulus was significantly lower than that of observed for odour1 and odour2. (one-way ANOVA with Tukey's multiple comparison, *indicates $p<0.05$).

In order to probe the sampling strategies used during the OM task, we compared several parameters. For all the ISIs, the sniff frequency, inhalation/exhalation ratio, and inhalation and exhalation amplitudes were computed during the absence of stimulus (average of before odour1, ISI, and after odour2), odour1, and odour2 periods. Similar to what was seen in detection, all of the parameters significantly increased during the stimulus period (odour1 and odour2) compared to the no-stimulus period for all ISIs. Moreover, no significant differences were found in any of the parameters when compared between odour1 and odour2 (Sniff Frequency: Figure 5-6A, Inhalation: Exhalation: Figure 5-6B, Inhalation Amplitude: Figure 5-6C, and Exhalation Amplitude: Figure 5-6D, one-way ANOVA with Tukey's multiple comparison test for all ISIs, *indicates $p<0.05$). All breathing parameters for different ISIs remained consistent, as no significant difference was observed between them (For all parameters across different ISIs, one-way ANOVA, Stimulus absent: $p>0.05$, odour1: $p>0.05$, odour2: $p>0.05$). Taken together our results demonstrate that sniffing behaviour is independent of ISIs employed.

5.3.3. Sniffing behaviour remained similar across different concentrations of odours

Since we noticed an increase in respiratory characteristics for a blank stimulus during the detection task, we decided to further explore the concentration-dependent impacts on the sampling strategies. To achieve this, we conducted a detection task using five odorants, presenting the subjects with each odorant in a range of concentrations: 50%, 30%, 16.75%, and 7.14% (diluted with air, volume/volume). 30 healthy volunteers were used in this study, and each session had 20 trials, one for each concentration of each odorant. The participants responded by pressing a response button after detecting a stimulus. The detection accuracy measured by detection indices for different concentrations were found to rise with concentration (Figure 5-7A, Average index: 7.14% - 0.30 ± 0.0477; 16.75% - 0.366 ± 0.0470; 30% - 0.513 ± 0.0391; 50% - 0.726 ± 0.0338, One-way Repeated Measure ANOVA, $F = 26.60$, $p < 0.0001$). When the dynamics of inhalation and exhalation were plotted against time, a rise in respiration was visible for all concentrations during the stimulus presentation window, but there were no differences in the traces across different concentrations (Figure 5-7B).

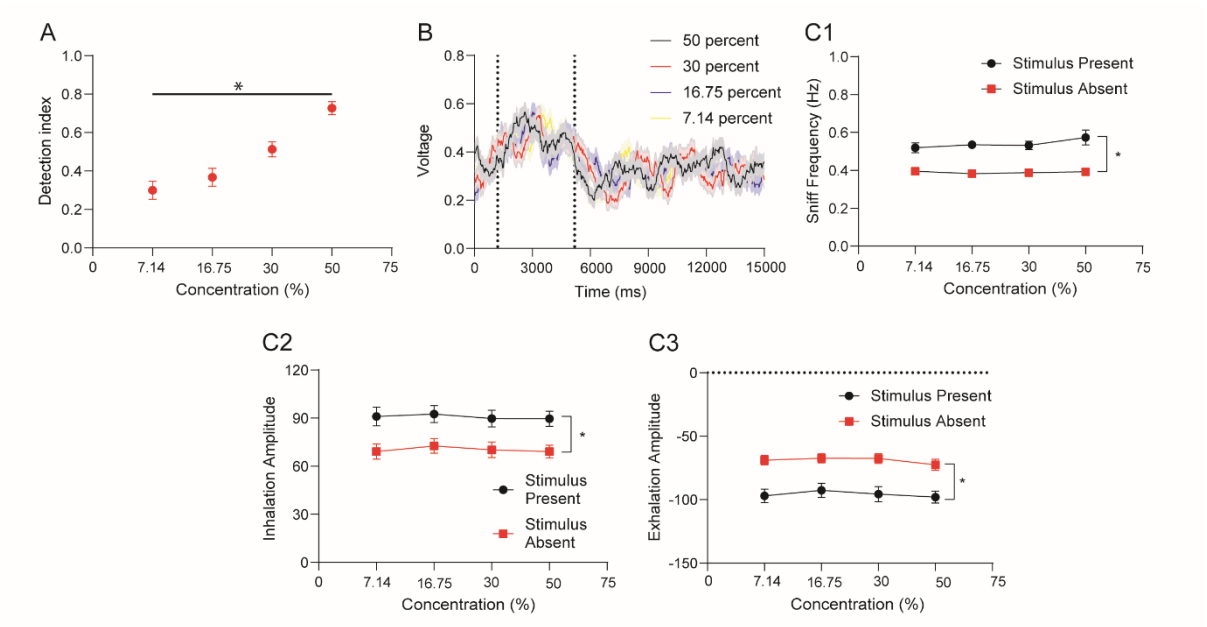

Figure 5-7 – Breathing parameters of healthy human subjects during the absence and presence of stimuli for different concentration of odorants

A) Average detection accuracy of all subjects for different concentrations of odorants. The average accuracies increased with increase in concentration. (One-way Repeated Measure ANOVA, $F = 26.60$, $p < 0.0001$).

B) Average of breathing traces of all subjects for different concentrations. The solid lines indicate the mean of the breathing traces of all subjects for different concentrations. The shaded region indicates the SEM.

C) C1) Graphs representing average sniff frequency of subjects in presence (black dots and line) and absence (red dots and line) of odours for different concentrations. (Two-way Repeated Measure ANOVA, *indicates $p<0.05$).

C2) Graphs representing average inhalation amplitude of subjects in presence (black dots and line) and absence (red dots and line) of odours for different concentrations. (Two-way Repeated Measure ANOVA, *indicates $p<0.05$).

C3) Graphs representing average exhalation amplitude of subjects in presence (black dots and line) and absence (red dots and line) of odours for different concentrations. (Two-way Repeated Measure ANOVA, *indicates $p<0.05$).

The sniff parameters were also measured and compared at various concentrations. In comparison to the window when stimulus was absent, sniffing frequency for all concentrations shown a substantial increase during the stimulus period (Figure 5-7C1, Two-way Repeated Measure ANOVA, * indicates $p<0.05$). However, sniffing frequency throughout the stimulus time was consistent across all concentrations (one-way ANOVA, $F = 0.097$, $p = 0.9430$). For other parameters, primarily the inhalation and exhalation amplitude, similar results were obtained (Figure 5-7C2 and C3: Two-way Repeated Measure ANOVA, between stimulus present and absent, *indicates $p<0.05$, one-way ANOVA across stimulus present period; Inhalation amplitude: $F = 0.4210$, $p = 0.7040$, Exhalation amplitude: $F = 1.012$, $p = 0.3879$). These findings indicate concentration-independent sniffing behaviour for the odour detections. However, more studies are needed to determine the neural mechanisms underlying these observations.

5.3.4. Sampling strategies of Post-COVID 19 subjects during odour detection task

Various neurological impairments including olfactory dysfunctions and respiratory problems are reported in long COVID (54,56,294). As this paradigm had been used to probe the breathing patterns while human subjects are engaged in olfaction-based cognitive tasks, we wanted to extend this paradigm to investigate the breathing dynamics in individuals recovered from COVID-19. Olfactory detection task was conducted, and results were compared to those of healthy human subjects.

As our primary objective was to compare the breathing patterns, we probed their detection efficiencies for the highest concentration (50%, v/v). Although the statistics showed a difference between two groups (number of subjects in two groups were different), both groups showed above 80% accuracy in detecting different odours (Figure 5-8A, Controls – 0.88 ± 0.013, Post COVID-19 – 0.82 ± 0.197, two-tailed unpaired t-test, p = 0.0307). When respiratory dynamics were examined, the Post COVID-19 individuals showed an increase in breathing throughout the odour presentation and decision-making phase, which was followed by a decrease in breathing to the basal level (Figure 5-8B). This pattern resembled what was seen in the controls during an odour detection task.

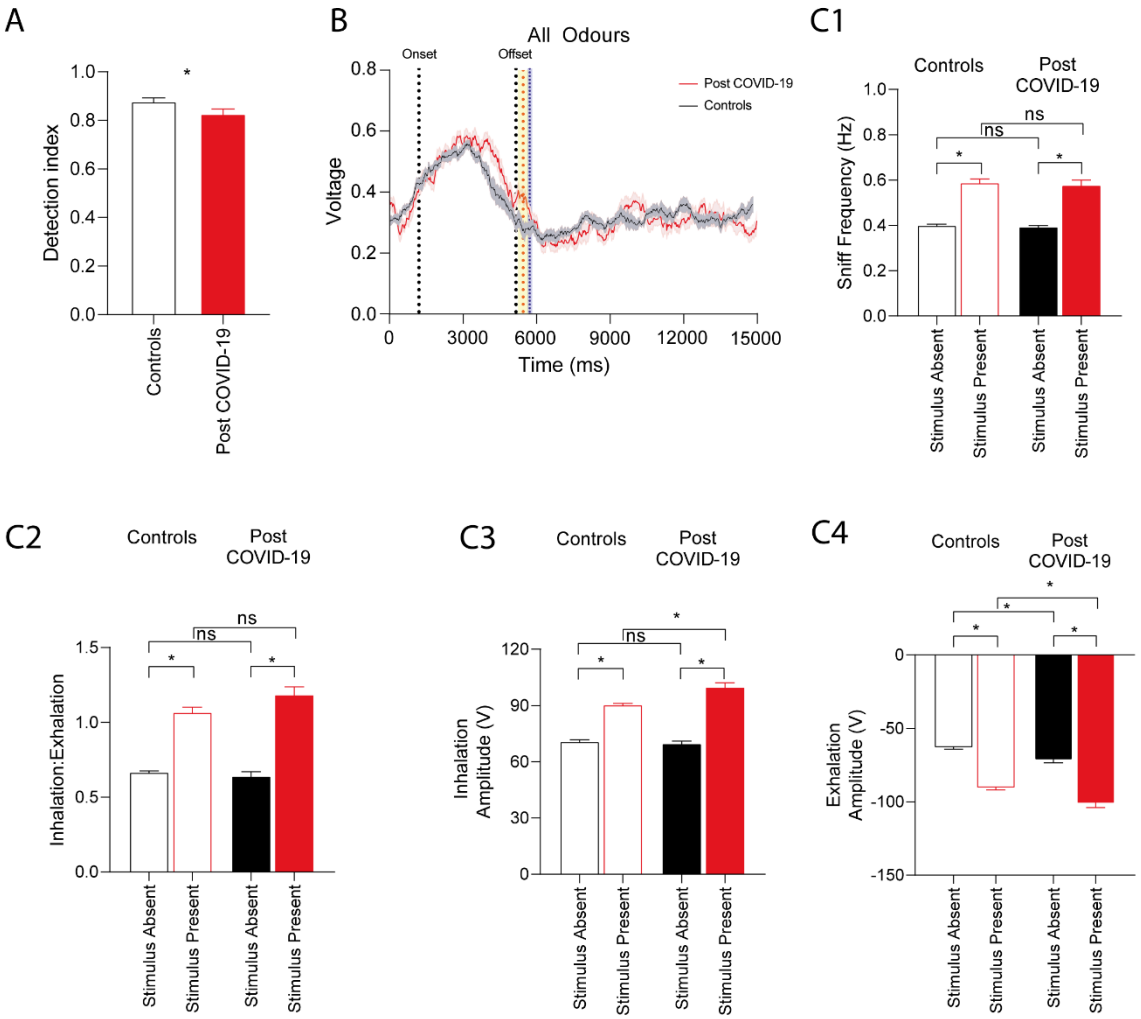

Figure 5-8 – Comparison of performance and breathing parameters of healthy human subjects with those of Post COVID-19 subjects during an odour detection task

A) Bar graphs representing average detection index of controls and Post COVID-19 subjects. Controls showed higher detection abilities as compare to post COVID-19 subjects. (two-tailed unpaired t-test, $p = 0.0307$, $n_{control} = 71$, $n_{Post\ COVID\text{-}19} = 33$).

B) Average of breathing traces of Post COVID-19 and control subjects across different odorants. The dotted black lines represent the onset and offset of the stimulus. The red and black solid lines represent breathing traces for Post COVID-19 and control subjects, respectively, whereas shaded area represents SEM. The dotted magenta and red line represent the average of detection time for Post COVID-19 and control subjects, respectively, whereas the shaded area (magenta and yellow – controls and Post COVID-19, respectively) represents the SEM of detection time. The breathing traces for control were same as in Figure 5-3B.

C) C1) Bar graphs representing average sniff frequencies (SFs) of controls and Post COVID-19 subjects in the absence and presence of stimulus. The SFs of controls and Post COVID-19 subjects during stimulus period were similar (*indicates $p<0.05$).

C2) Bar graphs representing average inhalation to exhalation ratios of controls and Post COVID-19 subjects in the absence and presence of stimulus. The ratios of controls and Post COVID-19 subjects during stimulus period were similar (*indicates $p<0.05$).

C3) Bar graphs representing average inhalation amplitudes of controls and Post COVID-19 subjects in the absence and presence of stimulus. The inhalation amplitudes of Post COVID-19 subjects were significantly higher than controls during stimulus period (*indicates $p<0.05$).

C4) Bar graphs representing average exhalation amplitudes of controls and Post COVID-19 subjects in the absence and presence of stimulus. The exhalation amplitudes of Post COVID-19 subjects were significantly higher than controls during stimulus period. (*indicates $p<0.05$).

We observed that for Post COVID-19 individuals, the sniff frequency, inhalation to exhalation ratio, and inhalation & exhalation amplitudes were higher when evaluated in the presence of the stimulus compared to the absence of the stimulus (Breathing parameters compared for Post COVID-19 subjects in absence and presence of stimulus: Figure 5-8C1, C2, C3, and C4, paired t-test, *indicates $p<0.05$). Additionally, the various respiratory parameters were compared to the values of the controls. Our findings show that the sniff frequency for both groups was comparable during both the periods when the stimulus was present and absent (Figure 5-8C1, Stimulus present: controls – 0.5883 ± 0.0162, Post COVID-19 – 0.5776 ± 0.0225, two-tailed unpaired t-test, $p = 0.7053$; Stimulus absent: controls – 0.3998 ± 0.0049, Post COVID-19 – 0.0056 ± 0.0225, two-tailed unpaired t-test, $p = 0.4104$). Similar results were also found for the ratio of inhalation to exhalation, wherein no significant difference was observed between controls and Post COVID-19 subjects for both in presence and absence of

stimulus (Figure 5-8C2, Stimulus present: controls – 1.067 ± 0.0342, Post COVID-19 – 1.184 ± 0.0524, two-tailed unpaired t-test, $p = 0.0798$; Stimulus absent: controls – 0.666 ± 0.0084, Post COVID-19 – 0.640 ± 0.0298, two-tailed unpaired t-test, $p = 0.4149$). However, compared to controls, the inhalation and exhalation amplitudes of Post COVID-19 individuals were greater in the presence of stimuli (Figure 5-8C3 and C4, Inhalation amplitudes: controls – 90.33 ± 0.8094, Post COVID-19 – 99.89 ± 2.258, two-tailed unpaired t-test, $p = 0.0011$; Exhalation amplitudes: controls – -90.75 ± 1.170, Post COVID-19 – -101.4 ± 2.531, two-tailed unpaired t-test, $p = 0.0015$). In the absence of stimulus, the inhalation amplitudes between both groups were similar (Figure 5-8C3, controls – 70.82 ± 0.8283, Post COVID-19 – 69.66 ± 1.364, two-tailed unpaired t-test, $p = 0.4769$), however, exhalation amplitude for Post COVID-19 subjects were relatively higher (Figure 5-8C4, controls – -63.21 ± 0.8989, Post COVID-19 – -73.04 ± 1.641, two-tailed unpaired t-test, $p < 0.0001$), suggesting that Post COVID-19 subjects exhaled more intensely than the controls even in the absence of stimulus.

5.4. Discussion

Olfactory dysfunctions are known to be associated with a number of disease conditions (43,44,53–56,45–52). For the purpose of evaluating human olfactory abilities, our lab has previously developed a cutting-edge "Olfactory-Action Meter" (295). In addition to investigation of olfactory fitness, this equipment has served as a diagnostic tool as well as a means of identifying asymptomatic COVID-19 carriers (49). Since breathing is the initial action that permits the sampling of odorant molecules for olfactory perception (57), and the information linking sniff strategies with olfactory perception still remains elusive, we intended to determine how individuals sample olfactory stimuli under normal and disease conditions. Therefore, the major goal of this chapter was to create a novel approach for the sensitive evaluation of breathing characteristics during olfaction-based cognitive tasks. To do this, we integrated our existing Olfactory Action Meter (OAM) with a thermocouple-based pressure sensor, which could transmit signals directly to oscilloscopes synchronized with the setup. With this approach, we could monitor the breathing patterns of participants as they engaged in olfaction-based tasks with a resolution as high as 30 ms.

The sniffing behaviour of subjects for either during the olfactory detection or the more complex olfactory matching task displayed similar results. In comparison to when there was no stimulus, it was observed that total respiration increased and reached a maximum value in the presence of stimuli. After the rise in respiration reached its peak, it began to drop, and the completion of the decay occurred at the same time as the decision-making period for both tests (Figure 5-3A-C and Figure 5-5B1-B4). Additionally, it was observed that breathing parameters such as sniff frequency, the ratio of time spent inhaling to exhaling, and inhalation and exhalation amplitudes were all higher in presence of a stimulus compared to the absence of stimulus (Figure 5-4A-D and Figure 5-6A-D). Previously, an increase in respiratory volume was noticed when odours were present compared to the baseline (66), which was consistent and with our findings on the inhalation to exhalation ratio. The sniff volume rises as individuals spend more time in the inhaling phase as compared to exhalation. Contrary to the previous reports of, no-difference in the sniff frequency and breathing amplitudes (66), we detected an increase in these parameters in the presence of odours as compared to their absence. Our study employed a 4 second stimulus followed by a 13 second baseline (ITI), whereas the previously published study used a 16 second stimulus followed by a 32 second baseline. These differences might be due to the long stimulus duration (16 seconds) they employed compared to the duration we have used (4 seconds). Further, the decisions related to detections are taken within

5-6 seconds. Our findings suggest that when exposed to odours, participants breathe rapidly, with intense prolonged inhalations and intense short exhalations.

Further, we looked into how odorant concentrations affect breathing patterns of healthy human subjects. Our findings showed that sniff frequency and breathing amplitudes were higher during the stimulus period as compared to no-stimulus period, but there were no changes in sniffing frequency and breathing amplitudes across varying concentrations. Mice have also been found to exhibit similar sniff invariant odour coding when trained at various odour concentrations (235). Few reports show that sniff volume varies with odour concentration (66,292,296). However, more studies are needed to correlate sniff volume with various breathing parameters.

This novel approach was also employed to investigate odour-associated sampling in people recovered with COVID-19, since these individuals have been reported to have persistent olfactory impairments (56,294,297–299). We found that the sampling behaviour of Post COVID-19 individuals was different from that of the controls because they exhibited higher breathing amplitudes; the neural mechanisms underlying this behaviour needs to be investigated further.

Breathing, in addition to facilitating olfactory perception, also has multiple physiological roles. It keeps life going by supplying the oxygen required for metabolism and eliminating the by-product of these reactions, carbon dioxide. Breathing has the ability to influence homeostatic activities in other systems such as the autonomic nervous system, the circulatory system, chemical regulation, and metabolism (58–60). Changes in respiratory responses are well known to affect brain activity, hence altering cognitive functions. e.g. olfactory imagery, attention, memory, sleep disorders (61–66). As a result, this approach not only allows us to quantify breathing during olfactory sensation and perception, but also enables us to investigate breathing parameters in the context of cognitive functions and accompanying deficits.

5.5. Future Directions

Using the novel Olfactory-Action Meter integrated with thermocouple-based pressure sensor, we successfully examined the sampling behaviour of people engaged in olfaction-based tasks. We also want to employ this paradigm, that is now well established, to investigate the sampling behaviour in higher olfactory cognition and olfactory dysfunctions associated with neurodegenerative diseases. As a first step, we have already started looking at how healthy and post-COVID-19 participants sample when doing more complex olfactory tasks, such as the olfactory matching learning. This paradigm will thereafter be used to assess the sampling behaviours of people who suffer from cognitive impairments associated with neurodegenerative diseases like Parkinson's and Alzheimer's.

Publications

1. Rajdeep Bhowmik*, Meenakshi Pardasani*, **Sarang Mahajan***, Anindya S. Bhattacharjee, Sasank Konakamchi, Shambhavi Phadnis, Thasneem Musthafa, Eleanor McGowan, Priyadarshini Srikanth, Shruti D. Marathe, Nixon M. Abraham. Uncertainty revealed by delayed responses during olfactory matching (*Equal contribution). Under Review, *bioRxiv:* https://doi.org/10.1101/2022.09.11.507462 (2022).

Manuscripts under submission:

1. **Sarang Mahajan**, Deepshikha Sen, Anantu Sunil, Priyadharshini Srikanth, Shruti D Marathe, Karishma Shaw, Mahesh Sahare, Sanjeev Galande, and Nixon M. Abraham. Knockout of ACE2 receptors lead to morphological aberrations in rodent olfactory centers and dysfunctions associated with sense of smell.

Manuscripts under preparation:

1. **Sarang Mahajan**, Suhel Tamboli, Anindya S. Bhattacharjee, Priyadarshini Srikanth, Meenakshi Pardasani, Nixon M. Abraham. Mouse olfactory system acts as anemo-detector and -discriminator.
2. **Sarang Mahajan**, Ganesh A. Nair, Meenakshi Pardasani, Nixon M. Abraham. Enhanced sniffing shown by human subjects during olfactory-driven cognitive task.

Other Publications:

1. Rajdeep Bhowmik, Meenakshi Pardasani, **Sarang Mahajan**, Rahul Magar, Sameer V. Joshi, Ganesh Ashish Nair, Anindya S. Bhattacharjee, Nixon M. Abraham. Persistent olfactory learning deficits during and post-COVID-19 infection. Curr Res Neurobiol. 2023 Mar 5:100081. doi: 10.1016/j.crneur.2023.100081. Epub ahead of print. PMCID: PMC9985517.
2. Meenakshi Pardasani, Anantha Ramakrishnan, **Sarang Mahajan**, Meher Kantroo, Eleanor McGowan, Susobhan Das, Priyadharshini Srikant, Sanyukta Pandey, Nixon M. Abraham. Perceptual learning deficits mediated by somatostatin releasing inhibitory interneurons of olfactory bulb in an early life stress mouse model. Research Square: 10.21203/rs.3.rs-2559042/v1 (2023).

References

1. Bretman A, Westmancoat JD, Gage MJG, Chapman T. Males use multiple, redundant cues to detect mating rivals. Curr Biol. 2011 Apr;21(7):617–22.

2. Brown GE, Magnavacca G. Predator inspection behaviour in a characin fish: an interaction between chemical and visual information? Ethology. 2003;109(9):739–50.

3. Candolin U. The use of multiple cues in mate choice. Biol Rev Camb Philos Soc. 2003 Nov;78(4):575–95.

4. Gomes DGE, Halfwerk W, Taylor RC, Ryan MJ, Page RA. Multimodal weighting differences by bats and their prey: probing natural selection pressures on sexually selected traits. Anim Behav [Internet]. 2017;134:99–102. Available from: https://www.sciencedirect.com/science/article/pii/S0003347217303378

5. Graham P, Philippides A, Baddeley B. Animal Cognition: Multi-modal Interactions in Ant Learning. Curr Biol [Internet]. 2010;20(15):R639–40. Available from: https://www.sciencedirect.com/science/article/pii/S0960982210007633

6. Munoz NE, Blumstein DT. Multisensory perception in uncertain environments. Behav Ecol [Internet]. 2012 May 1;23(3):457–62. Available from: https://doi.org/10.1093/beheco/arr220

7. Thompson JT, Bissell AN, Martins EP. Inhibitory interactions between multimodal behavioural responses may influence the evolution of complex signals. Anim Behav [Internet]. 2008;76(1):113–21. Available from: https://www.sciencedirect.com/science/article/pii/S000334720800122X

8. Wierucka K, Pitcher BJ, Harcourt R, Charrier I. Multimodal mother–offspring recognition: the relative importance of sensory cues in a colonial mammal. Anim Behav [Internet]. 2018;146:135–42. Available from: https://www.sciencedirect.com/science/article/pii/S0003347218303208

9. Munoz NE, Blumstein DT. Optimal multisensory integration. Behav Ecol [Internet]. 2020 Jan 31;31(1):184–93. Available from: https://doi.org/10.1093/beheco/arz175

10. Lankarany M, Al-basha D, Ratté S, Prescott SA. Differentially synchronized spiking

enables multiplexed neural coding. 2019;116(20).

11. Park IM, Meister MLR, Huk AC, Pillow JW. Encoding and decoding in parietal cortex during sensorimotor decision-making. Nat Neurosci [Internet]. 2014;17(August):1395–403. Available from: http://dx.doi.org/10.1038/nn.3800%5Cnhttp://www.ncbi.nlm.nih.gov/pubmed/25174005

12. Grosmaitre X, Santarelli LC, Tan J, Luo M, Ma M. Dual functions of mammalian olfactory sensory neurons as odor detectors and mechanical sensors. 2007;10(3):348–54.

13. Connelly T, Yu Y, Grosmaitre X, Wang J, Santarelli LC, Savigner A, et al. G protein-coupled odorant receptors underlie mechanosensitivity in mammalian olfactory sensory neurons. Proc Natl Acad Sci U S A [Internet]. 2014;1–6. Available from: http://www.ncbi.nlm.nih.gov/pubmed/25550517

14. Iwata R, Kiyonari H, Imai T. Mechanosensory-Based Phase Coding of Odor Identity in the Olfactory Bulb Article Mechanosensory-Based Phase Coding of Odor Identity in the Olfactory Bulb. Neuron [Internet]. 2017;96(5):1139-1152.e7. Available from: https://doi.org/10.1016/j.neuron.2017.11.008

15. Wu XR, Liu Y, Wang L, Li B, Xu F. Activity Patterns Elicited by Airflow in the Olfactory Bulb and Their Possible Functions. 2017;37(44):10700–11.

16. Adrian BYED. OLFACTORY REACTIONS IN THE BRAIN OF THE HEDGEHOG. 1941;459–73.

17. Ressler KJ, Sullivan SL, Buck LB. Information coding in the olfactory system: evidence for a stereotyped and highly organized epitope map in the olfactory bulb. Cell. 1994 Dec;79(7):1245–55.

18. Buck L, Axel R. A novel multigene family may encode odorant receptors: a molecular basis for odor recognition. Cell. 1991;65(1):175–87.

19. Murlis J, Elkinton JS, Carde RT. Odor plumes and how insects use them. Annu Rev Entomol Vol 37. 1992;(86):505–32.

20. Duistermars BJ, Frye M a. Multisensory integration for odor tracking by flying Drosophila. Behavior, circuits and speculation. Commun Integr Biol.

2010;3(February):1–5.

21. Zimmer-Faust RK, Finelli CM, Pentcheff ND, Wethey DS. Odor plumes and animal navigation in turbulent water flow: A field study. Biol Bull. 1995;188(2):111–6.

22. Vickers NJ. Mechanisms of animal navigation in odor plumes. Biol Bull. 2000 Apr;198(2):203–12.

23. Koehl MAR. The fluid mechanics of arthropod sniffing in turbulent odor plumes. Chem Senses. 2006 Feb;31(2):93–105.

24. Baker TC, Kuenen LPS. Pheromone source location by flying moths: A supplementary non-anemotactic mechanism. Science (80-). 1982;216(4544):424–7.

25. Van Breugel F, Dickinson MH. Plume-tracking behavior of flying drosophila emerges from a set of distinct sensory-motor reflexes. Curr Biol [Internet]. 2014;24(3):274–86. Available from: http://dx.doi.org/10.1016/j.cub.2013.12.023

26. Wachowiak M. All in a Sniff: Olfaction as a Model for Active Sensing. Neuron. 2011;71(6):962–73.

27. Ressler KJ, Sullivan SL, Buck LB. A zonal organization of odorant receptor gene expression in the olfactory epithelium. Cell. 1993;73(3):597–609.

28. Spehr M, Munger SD. Olfactory receptors: G protein-coupled receptors and beyond. J Neurochem [Internet]. 2009;109(6):1570–83. Available from: http://doi.wiley.com/10.1111/j.1471-4159.2009.06085.x

29. Buck LB. Information coding in the vertebrate olfactory system. Annu Rev Neurosci. 1996;19:517–44.

30. Potter SM, Zheng C, Koos DS, Feinstein P, Fraser SE, Mombaerts P. Structure and emergence of specific olfactory glomeruli in the mouse. J Neurosci. 2001;21(24):9713–23.

31. Nakamura T. Cellular and molecular contituents of olfactory sensation in vertebrates. Comp Biochem Physiol. 2000;126:17–32.

32. Kosaka T, Kosaka K. “Interneurons” in the olfactory bulb revisited. Neurosci Res [Internet]. 2011;69(2):93–9. Available from: https://www.sciencedirect.com/science/article/pii/S0168010210028142

33. Shipley MT, Ennis M. Functional organization of olfactory system. J Neurobiol. 1996 May;30(1):123–76.

34. Kiyokage E, Pan Y-Z, Shao Z, Kobayashi K, Szabo G, Yanagawa Y, et al. Molecular identity of periglomerular and short axon cells. J Neurosci Off J Soc Neurosci. 2010 Jan;30(3):1185–96.

35. Wachowiak M, Shipley MT. Coding and synaptic processing of sensory information in the glomerular layer of the olfactory bulb. Semin Cell Dev Biol. 2006 Aug;17(4):411–23.

36. W. MT, Bert S, N. UN. Action potential propagation in mitral cell lateral dendrites is decremental and controls recurrent and lateral inhibition in the mammalian olfactory bulb. Proc Natl Acad Sci [Internet]. 2001 Jan 2;98(1):319–24. Available from: https://doi.org/10.1073/pnas.98.1.319

37. Urban NN. Lateral inhibition in the olfactory bulb and in olfaction. Physiol Behav. 2002 Dec;77(4–5):607–12.

38. Shepherd GM. Perspectives on olfactory processing, conscious perception, and orbitofrontal cortex. Ann N Y Acad Sci. 2007;1121:87–101.

39. Price JL. An autoradiographic study of complementary laminar patterns of termination of afferent fibers to the olfactory cortex. J Comp Neurol. 1973;150(1):87–108.

40. Yu YSW, Graff MM, Hartmann MJZ. Mechanical responses of rat vibrissae to airflow. 2016;937–48.

41. Yu YSW, Graff MM, Bresee CS, Man YB, Hartmann MJZ. Whiskers aid anemotaxis in rats. 2016;(August):1–8.

42. Parrish-Aungst S, Shipley MT, Erdelyi F, Szabo G, Puche AC. Quantitative analysis of neuronal diversity in the mouse olfactory bulb. J Comp Neurol. 2007 Apr;501(6):825–36.

43. Marin C, Vilas D, Langdon C, Alobid I, López-Chacón M, Haehner A, et al. Olfactory Dysfunction in Neurodegenerative Diseases. Curr Allergy Asthma Rep. 2018 Jun;18(8):42.

44. Barresi M, Ciurleo R, Giacoppo S, Foti Cuzzola V, Celi D, Bramanti P, et al.

Evaluation of olfactory dysfunction in neurodegenerative diseases. J Neurol Sci. 2012 Dec;323(1–2):16–24.

45. Holbrook EH, Leopold DA. An updated review of clinical olfaction. Curr Opin Otolaryngol Head Neck Surg. 2006 Feb;14(1):23–8.

46. Li K, Liu F-F, He C-X, Huang H-Z, Xie A-J, Hu F, et al. Olfactory Deprivation Hastens Alzheimer-Like Pathologies in a Human Tau-Overexpressed Mouse Model via Activation of cdk5. Mol Neurobiol. 2016 Jan;53(1):391–401.

47. Aguilar Martínez N, Aguado Carrillo G, Saucedo Alvarado PE, Mendoza García CA, Velasco Monroy AL, Velasco Campos F. Clinical importance of olfactory function in neurodegenerative diseases. Rev Médica del Hosp Gen México [Internet]. 2018;81(4):268–75. Available from: https://www.sciencedirect.com/science/article/pii/S0185106317300501

48. Welge-Lüssen A, Wolfensberger M. Olfactory disorders following upper respiratory tract infections. Adv Otorhinolaryngol. 2006;63:125–32.

49. Bhattacharjee AS, Joshi S V, Naik S, Sangle S, Abraham NM. Quantitative assessment of olfactory dysfunction accurately detects asymptomatic COVID-19 carriers. EClinicalMedicine. 2020 Nov;28:100575.

50. Lechien JR, Cabaraux P, Chiesa-Estomba CM, Khalife M, Hans S, Calvo-Henriquez C, et al. Objective olfactory evaluation of self-reported loss of smell in a case series of 86 COVID-19 patients. Head Neck. 2020 Jul;42(7):1583–90.

51. Moein ST, Hashemian SM, Mansourafshar B, Khorram-Tousi A, Tabarsi P, Doty RL. Smell dysfunction: a biomarker for COVID-19. Int Forum Allergy Rhinol. 2020 Aug;10(8):944–50.

52. Giacomelli A, Pezzati L, Conti F, Bernacchia D, Siano M, Oreni L, et al. Self-reported Olfactory and Taste Disorders in Patients With Severe Acute Respiratory Coronavirus 2 Infection: A Cross-sectional Study. Vol. 71, Clinical infectious diseases : an official publication of the Infectious Diseases Society of America. 2020. p. 889–90.

53. Yus M, Matias-Guiu JA, Gil-Martínez L, Gómez-Ruiz N, Polidura C, Jorquera M, et al. Persistent olfactory dysfunction after COVID-19 is associated with reduced perfusion in the frontal lobe. Acta Neurol Scand. 2022 Aug;146(2):194–8.

54. Nguyen NN, Hoang VT, Lagier J-C, Raoult D, Gautret P. Long-term persistence of olfactory and gustatory disorders in COVID-19 patients. Vol. 27, Clinical microbiology and infection : the official publication of the European Society of Clinical Microbiology and Infectious Diseases. 2021. p. 931–2.

55. Nguyen NN, Hoang VT, Dao TL, Meddeb L, Cortaredona S, Lagier J-C, et al. Long-Term Persistence of Olfactory and Gustatory Disorders in COVID-19 Patients. Front Med. 2022;9:794550.

56. Bhowmik R, Pardasani M, Mahajan S, Magar R, Joshi S V, Nair GA, et al. Persistent Olfactory Learning Deficits during and Post-COVID-19 Infection. SSRN Electron J. 2022;

57. Mainland J, Sobel N. The Sniff Is Part of the Olfactory Percept. Chem Senses [Internet]. 2005;31(2):181–96. Available from: https://doi.org/10.1093/chemse/bjj012

58. Berger RD, Saul JP, Cohen RJ. Assessment of autonomic response by broad-band respiration. IEEE Trans Biomed Eng. 1989;36(11):1061–5.

59. Wirkner CS, Richter S, Watling L, Thiel L, others. Circulatory system and respiration. Nat Hist Crustac. 2013;1:376–412.

60. Clancy J, McVicar A. The respiratory system and homeostasis. Br J Theatr Nurs NATNews Off J Natl Assoc Theatr Nurses. 1996 Nov;6(8):16-20,22.

61. Nakamura NH, Fukunaga M, Oku Y. Respiratory modulation of cognitive performance during the retrieval process. PLoS One. 2018;13(9):e0204021.

62. Grassmann M, Vlemincx E, von Leupoldt A, Mittelstädt JM, Van den Bergh O. Respiratory Changes in Response to Cognitive Load: A Systematic Review. Neural Plast. 2016;2016:8146809.

63. Boyadzhieva A, Kayhan E. Keeping the Breath in Mind: Respiration, Neural Oscillations, and the Free Energy Principle. Front Neurosci. 2021;15:647579.

64. Homma I, Masaoka Y. Breathing rhythms and emotions. Exp Physiol [Internet]. 2008 Sep 1;93(9):1011–21. Available from: https://doi.org/10.1113/expphysiol.2008.042424

65. Pang B, Yee KK, Lischka FW, Rawson NE, Haskins ME, Wysocki CJ, et al. The influence of nasal airflow on respiratory and olfactory epithelial distribution in felids. J

Exp Biol [Internet]. 2016;(April):1866–74. Available from: http://jeb.biologists.org/cgi/doi/10.1242/jeb.131482

66. Kleemann AM, Kopietz R, Albrecht J, Schöpf V, Pollatos O, Schreder T, et al. Investigation of Breathing Parameters during Odor Perception and Olfactory Imagery. Chem Senses [Internet]. 2008;34(1):1–9. Available from: https://doi.org/10.1093/chemse/bjn042

67. Taniguchi K, Taniguchi K. Phylogenic Studies on the Olfactory System in Vertebrates. 2014;

68. Adibi M. Whisker-Mediated Touch System in Rodents: From Neuron to Behavior. Front Syst Neurosci. 2019;13(August):1–24.

69. Toida K, Takami S. Structure and function of the olfactory system: Overview. Anat Sci Int. 2008;83(4):183–5.

70. Arabzadeh E, Panzeri S, Diamond ME. Whisker Vibration Information Carried by Rat Barrel Cortex Neurons. J Neurosci. 2004;24(26):6011–20.

71. Arabzadeh E, Petersen RS, Diamond ME. Encoding of Whisker Vibration by Rat Barrel Cortex Neurons : Implications for Texture Discrimination. J Neurosci. 2003;23(27):9146–54.

72. Deschênes M, Moore J, Kleinfeld D. Sniffing and whisking in rodents. Curr Opin Neurobiol. 2012;22(2):243–50.

73. Kleinfeld D, Deschênes M, Wang F, Moore JD. More than a rhythm of life: breathing as a binder of orofacial sensation. Nat Neurosci [Internet]. 2014;17(5):647–51. Available from: http://www.nature.com/doifinder/10.1038/nn.3693

74. Moore JD, Deschênes M, Furuta T, Huber D, Smear MC, Demers M, et al. Hierarchy of orofacial rhythms revealed through whisking and breathing. Nature. 2013;497(7448):205–10.

75. Vickers NJ. Mechanisms of animal navigation in odor plumes. Biol Bull. 2000;198(2):203–12.

76. Koehl MAR. The fluid mechanics of arthropod sniffing in turbulent odor plumes. Chem Senses. 2006;31(2):93–105.

77. Wu R, Liu Y, Wang L, Li B, Xu F. Activity patterns elicited by airflow in the olfactory bulb and their possible functions. J Neurosci. 2017;37(44):10700–11.

78. Wadhams GH, Armitage JP. Making sense of it all: Bacterial chemotaxis. Nat Rev Mol Cell Biol. 2004;5(12):1024–37.

79. Hussain A. The Olfactory Nervous System Of Terrestrial And Aquatic Vertebrates. Nat Preced [Internet]. 2011; Available from: https://doi.org/10.1038/npre.2011.6642.1

80. Graziadei PP, Graziadei G a. Neurogenesis and neuron regeneration in the olfactory system of mammals. I. Morphological aspects of differentiation and structural organization of the olfactory sensory neurons. J Neurocytol [Internet]. 1979;8(1):1–18. Available from: http://www.ncbi.nlm.nih.gov/pubmed/438867

81. Moran DT, Rowley 3rd JC, Jafek BW. Electron microscopy of human olfactory epithelium reveals a new cell type: the microvillar cell. Brain Res. 1982;253(1–2):39–46.

82. Buck L, Axel R. A novel multigene family may encode odorant receptors: A molecular basis for odor recognition. Cell [Internet]. 1991;65(1):175–87. Available from: http://www.ncbi.nlm.nih.gov/pubmed/1840504%5Cnhttp://linkinghub.elsevier.com/retrieve/pii/009286749190418X

83. Levy NS, Bakalyar HA, Reed RR. SIGNAL TRANSDUCTION IN OLFACTORY NEURONS. J Steroid Biochem Mol Biol. 1991;39(4):633–7.

84. Ressler KJ, Sullivan SL, Buck LB. Information coding in the olfactory system: evidence for a stereotyped and higly organized epitopc map in the olfactory bulb. Cell. 1994;79:1245–55.

85. Firestein BYS, Picco C, Meninit A, Nazionale C. THE RELATION BETWEEN STIMULUS AND RESPONSE IN OLFACTORY RECEPTOR CELLS OF THE TIGER SALAMANDER. J Gen Physiol. 1993;1–10.

86. Restrepo D, Boekhoff I, Breer H. Rapid kinetic measurements of second messenger formation in olfactory cilia from channel catfish. Am J Physiol. 1993 Apr;264(4 Pt 1):C906-11.

87. Lo YH, Bellis SL, Cheng LJ, Pang J, Bradley TM, Rhoads DE. Signal transduction for taurocholic acid in the olfactory system of Atlantic salmon. Chem Senses. 1994

Oct;19(5):371–80.

88. Lo YH, Bradley TM, Rhoads DE. Stimulation of Ca(2+)-regulated olfactory phospholipase C by amino acids. Biochemistry. 1993 Nov;32(46):12358–62.

89. Nakamura T. Cellular and molecular constituents of olfactory sensation in vertebrates. Comp Biochem Physiol A Mol Integr Physiol [Internet]. 2000;126(1):17–32. Available from: http://www.ncbi.nlm.nih.gov/pubmed/10908849

90. Mombaerts P. THEHUMAN REPERTOIRE OFODORANT RECEPTOR GENES AND PSEUDOGENES. 2001;493–510.

91. Greer PL, Bear DM, Lassance JM, Bloom ML, Tsukahara T, Pashkovski SL, et al. A Family of non-GPCR Chemosensors Defines an Alternative Logic for Mammalian Olfaction. Cell [Internet]. 2016;165(7):1734–48. Available from: http://dx.doi.org/10.1016/j.cell.2016.05.001

92. Pacifico R, Dewan A, Cawley D, Guo C, Bozza T. An olfactory subsystem that mediates high-sensitivity detection of volatile amines. Cell Rep. 2012 Jul;2(1):76–88.

93. Weihong L, Robert M, Gerald D, W. HS, Diego R. Olfactory neurons expressing transient receptor potential channel M5 (TRPM5) are involved in sensing semiochemicals. Proc Natl Acad Sci [Internet]. 2007 Feb 13;104(7):2471–6. Available from: https://doi.org/10.1073/pnas.0610201104

94. Strotmann J, Wanner I, Krieger J, Raming K, Breer H. Expression of odorant receptors in spatially restricted subsets of chemosensory neurones. [Internet]. Vol. 3, Neuroreport. 1992. p. 1053–6. Available from: http://www.ncbi.nlm.nih.gov/pubmed/1493216

95. Wyatt TD. Pheromones and animal behavior: chemical signals and signatures. Cambridge University Press; 2014.

96. Matsunami H, Buck LB. A Multigene Family Encoding a Diverse Array of Putative Pheromone Receptors in Mammals. Cell [Internet]. 1997;90(4):775–84. Available from: https://www.sciencedirect.com/science/article/pii/S0092867400805371

97. Ryba NJP, Tirindelli R. A New Multigene Family of Putative Pheromone Receptors. Neuron [Internet]. 1997;19(2):371–9. Available from: https://www.sciencedirect.com/science/article/pii/S0896627300809460

98. Herrada G, Dulac C. A Novel Family of Putative Pheromone Receptors in Mammals with a Topographically Organized and Sexually Dimorphic Distribution. Cell [Internet]. 1997;90(4):763–73. Available from: https://www.sciencedirect.com/science/article/pii/S009286740080536X

99. Dulac C, Axel R. A novel family of genes encoding putative pheromone receptors in mammals. Cell [Internet]. 1995;83(2):195–206. Available from: https://www.sciencedirect.com/science/article/pii/0092867495901612

100. Jia C, Halpern M. Subclasses of vomeronasal receptor neurons: differential expression of G proteins (Giα2 and Goα) and segregated projections to the accessory olfactory bulb. Brain Res [Internet]. 1996;719(1):117–28. Available from: https://www.sciencedirect.com/science/article/pii/0006899396001102

101. Chamero P, Leinders-Zufall T, Zufall F. From genes to social communication: molecular sensing by the vomeronasal organ. Trends Neurosci [Internet]. 2012;35(10):597–606. Available from: https://www.sciencedirect.com/science/article/pii/S0166223612000732

102. Bufe B, Schumann T, Zufall F. Formyl Peptide Receptors from Immune and Vomeronasal System Exhibit Distinct Agonist Properties*. J Biol Chem [Internet]. 2012;287(40):33644–55. Available from: https://www.sciencedirect.com/science/article/pii/S0021925820628654

103. Rivière S, Challet L, Fluegge D, Spehr M, Rodriguez I. Formyl peptide receptor-like proteins are a novel family of vomeronasal chemosensors. Nature [Internet]. 2009;459(7246):574–7. Available from: https://doi.org/10.1038/nature08029

104. D. LS, F. HL, Donghui K, J. CJ, L. WK, Jessica S-L, et al. Formyl peptide receptors are candidate chemosensory receptors in the vomeronasal organ. Proc Natl Acad Sci [Internet]. 2009 Jun 16;106(24):9842–7. Available from: https://doi.org/10.1073/pnas.0904464106

105. Loconto J, Papes F, Chang E, Stowers L, Jones EP, Takada T, et al. Functional Expression of Murine V2R Pheromone Receptors Involves Selective Association with the M10 and M1 Families of MHC Class Ib Molecules. Cell [Internet]. 2003;112(5):607–18. Available from: https://www.sciencedirect.com/science/article/pii/S0092867403001533

106. Ishii T, Hirota J, Mombaerts P. Combinatorial Coexpression of Neural and Immune Multigene Families in Mouse Vomeronasal Sensory Neurons. Curr Biol [Internet]. 2003;13(5):394–400. Available from: https://www.sciencedirect.com/science/article/pii/S0960982203000927

107. Berghard A, Buck LB. Sensory transduction in vomeronasal neurons: evidence for G alpha o, G alpha i2, and adenylyl cyclase II as major components of a pheromone signaling cascade. J Neurosci. 1996;16(3):909–18.

108. Ishii T, Mombaerts P. Coordinated coexpression of two vomeronasal receptor V2R genes per neuron in the mouse. Mol Cell Neurosci [Internet]. 2011;46(2):397–408. Available from: https://www.sciencedirect.com/science/article/pii/S1044743110002538

109. Adams DR, McFarland LZ. Septal olfactory organ in Peromyscus. Comp Biochem Physiol A Comp Physiol. 1971 Dec;40(4):971–4.

110. Kratzing JE. The structure and distribution of nasal glands in four marsupial species. J Anat. 1984 Oct;139 (Pt 3(Pt 3):553–64.

111. Kratzing JE. The anatomy and histology of the nasal cavity of the koala (Phascolarctos cinereus). J Anat [Internet]. 1984 Jan;138 (Pt 1(Pt 1):55–65. Available from: https://pubmed.ncbi.nlm.nih.gov/6706839

112. Kaluza JF, Gussing F, Bohm S, Breer H, Strotmann J. Olfactory receptors in the mouse septal organ. J Neurosci Res. 2004 May;76(4):442–52.

113. Taniguchi K, Arai T, Ogawa K. Fine structure of the septal olfactory organ of Masera and its associated gland in the golden hamster. J Vet Med Sci. 1993 Feb;55(1):107–16.

114. Tsanov M, Chah E, Reilly R, Mara SMO. Respiratory cycle entrainment of septal neurons mediates the fast coupling of sniffing rate and hippocampal theta rhythm. 2014;39(August 2013):957–74.

115. Weiler E, Farbman AI. The septal organ of the rat during postnatal development. Chem Senses. 2003 Sep;28(7):581–93.

116. Ma M, Grosmaitre X, Iwema CL, Baker H, Greer CA, Shepherd GM. Olfactory signal transduction in the mouse septal organ. J Neurosci Off J Soc Neurosci. 2003

Jan;23(1):317–24.

117. Tian H, Ma M. Molecular organization of the olfactory septal organ. J Neurosci Off J Soc Neurosci. 2004 Sep;24(38):8383–90.

118. Astic L, Saucier D. Topographical projection of the septal organ to the main olfactory bulb in rats: ontogenetic study. Brain Res. 1988 Aug;470(2):297–303.

119. Grosmaitre X, Santarelli LC, Tan J, Luo M, Ma M. Dual functions of mammalian olfactory sensory neurons as odor detectors and mechanical sensors. Nat Neurosci [Internet]. 2007;10(3):348–54. Available from: http://www.nature.com/doifinder/10.1038/nn1856

120. Grüneberg H. A ganglion probably belonging to the N. terminalis system in the nasal mucosa of the mouse. Z Anat Entwicklungsgesch [Internet]. 1973;140(1):39–52. Available from: https://doi.org/10.1007/BF00520716

121. Bumbalo R, Lieber M, Schroeder L, Polat Y, Breer H, Fleischer J. Grueneberg Glomeruli in the Olfactory Bulb are Activated by Odorants and Cool Temperature. Cell Mol Neurobiol. 2016;1–14.

122. Mamasuew K, Breer H, Fleischer J. Grueneberg ganglion neurons respond to cool ambient temperatures. Eur J Neurosci [Internet]. 2008;28(9):1775–85. Available from: http://doi.wiley.com/10.1111/j.1460-9568.2008.06465.x

123. Schmid A, Pyrski M, Biel M, Leinders-zufall T, Zufall F. Grueneberg Ganglion Neurons Are Finely Tuned Cold Sensors. 2010;30(22):7563–8.

124. Fuss SH, Omura M, Mombaerts P. The Grueneberg ganglion of the mouse projects axons to glomeruli in the olfactory bulb. Eur J Neurosci [Internet]. 2005 Nov 1;22(10):2649–54. Available from: https://doi.org/10.1111/j.1460-9568.2005.04468.x

125. Fleischer J, Schwarzenbacher K, Besser S, Hass N, Breer H. Olfactory receptors and signalling elements in the Grueneberg ganglion. J Neurochem. 2006 Jul;98(2):543–54.

126. Fleischer J, Mamasuew K, Breer H. Expression of cGMP signaling elements in the Grueneberg ganglion. Histochem Cell Biol. 2009 Jan;131(1):75–88.

127. Liu CY, Fraser SE, Koos DS. Grueneberg ganglion olfactory subsystem employs a cGMP signaling pathway. J Comp Neurol [Internet]. 2009 Sep 1;516(1):36–48.

Available from: https://doi.org/10.1002/cne.22096

128. Mombaerts P, Wang F, Dulac C, Chao SK, Nemes A, Mendelsohn M, et al. Visualizing an olfactory sensory map. Cell. 1996;87(4):675–86.

129. Lodovichi C. Topographic organization in the olfactory bulb. Cell Tissue Res [Internet]. 2021;383(1):457–72. Available from: https://doi.org/10.1007/s00441-020-03348-w

130. Yu CR, Power J, Barnea G, O'Donnell S, Brown HE V, Osborne J, et al. Spontaneous neural activity is required for the establishment and maintenance of the olfactory sensory map. Neuron. 2004 May;42(4):553–66.

131. Albeanu DF, Provost AC, Agarwal P, Soucy ER, Zak JD, Murthy VN. Olfactory marker protein (OMP) regulates formation and refinement of the olfactory glomerular map. Nat Commun [Internet]. 2018;9(1):5073. Available from: https://doi.org/10.1038/s41467-018-07544-9

132. Nakashima A, Ihara N, Shigeta M, Kiyonari H, Ikegaya Y, Takeuchi H. Structured spike series specify gene expression patterns for olfactory circuit formation. Science. 2019 Jul;365(6448).

133. Lorenzon P, Redolfi N, Podolsky MJ, Zamparo I, Franchi SA, Pietra G, et al. Circuit formation and function in the olfactory bulb of mice with reduced spontaneous afferent activity. J Neurosci Off J Soc Neurosci. 2015 Jan;35(1):146–60.

134. Nagayama S, Takahashi YK, Yoshihara Y, Mori K. Mitral and tufted cells differ in the decoding manner of odor maps in the rat olfactory bulb. J Neurophysiol. 2004;91(6):2532–40.

135. Igarashi KM, Ieki N, An M, Yamaguchi Y, Nagayama S, Kobayakawa K, et al. Parallel Mitral and Tufted Cell Pathways Route Distinct Odor Information to Different Targets in the Olfactory Cortex. J Neurosci. 2012;32(23):7970–85.

136. Fukunaga I, Berning M, Kollo M, Schmaltz A, Schaefer AT. Two Distinct Channels of Olfactory Bulb Output. Neuron. 2012;75(2):320–9.

137. Scott JW. The olfactory bulb and central pathways. Experientia. 1986;42(3):223–32.

138. Kauer JS, Cinelli a R. Are there structural and functional modules in the vertebrate

olfactory bulb? MicroscRes Tech [Internet]. 1993;24(1059-910X (Print) LA-eng PT-Journal Article RN-0 (Fluorescent Dyes) RN-0 (Pyridinium Compounds) RN-116946-58-8 (RH 414) RN-154-17-6 (Deoxyglucose) SB-IM):157–67. Available from: pm:8457727

139. Scott JW, Wellis DP, Riggott MJ, Buonviso N. Functional organization of the main olfactory bulb. Microsc Res Tech [Internet]. 1993;24(2):142–56. Available from: http://www.ncbi.nlm.nih.gov/entrez/query.fcgi?cmd=Retrieve&db=PubMed&dopt=Citation&list_uids=8457726

140. Trombley PQ, Shepherd GM. Synaptic transmission and modulation in the olfactory bulb. Curr Opin Neurobiol. 1993;3(4):540–7.

141. Boyd AM, Sturgill JF, Poo C, Isaacson JS. Cortical feedback control of olfactory bulb circuits. Neuron. 2012 Dec;76(6):1161–74.

142. Stettler DD, Axel R. Representations of odor in the piriform cortex. Neuron. 2009 Sep;63(6):854–64.

143. Isaacson JS. Odor representations in mammalian cortical circuits. Curr Opin Neurobiol. 2010 Jun;20(3):328–31.

144. Apicella A, Yuan Q, Scanziani M, Isaacson JS. Pyramidal cells in piriform cortex receive convergent input from distinct olfactory bulb glomeruli. J Neurosci Off J Soc Neurosci. 2010 Oct;30(42):14255–60.

145. Luskin MB, Price JL. The topographic organization of associational fibers of the olfactory system in the rat, including centrifugal fibers to the olfactory bulb. J Comp Neurol. 1983 May;216(3):264–91.

146. Haberly LB. Parallel-distributed processing in olfactory cortex: new insights from morphological and physiological analysis of neuronal circuitry. Chem Senses. 2001 Jun;26(5):551–76.

147. Sakamoto M, Kageyama R, Imayoshi I. The functional significance of newly born neurons integrated into olfactory bulb circuits. Front Neurosci. 2014;8(8 MAY):1–9.

148. Mori K, Manabe H, Narikiyo K, Onisawa N. Olfactory consciousness and gamma oscillation couplings across the olfactory bulb, olfactory cortex, and orbitofrontal cortex. Front Psychol. 2013;4:743.

149. Yan Z, Tan J, Qin C, Lu Y, Ding C, Luo M. Precise Circuitry Links Bilaterally Symmetric Olfactory Maps. Neuron [Internet]. 2008;58(4):613–24. Available from: https://www.sciencedirect.com/science/article/pii/S0896627308002584

150. Imai T, Sakano H. Interhemispheric Olfactory Circuit and the Memory Beyond. Neuron [Internet]. 2008;58(4):465–7. Available from: https://www.sciencedirect.com/science/article/pii/S0896627308004133

151. Izquierdo A. Functional Heterogeneity within Rat Orbitofrontal Cortex in Reward Learning and Decision Making. J Neurosci Off J Soc Neurosci. 2017 Nov;37(44):10529–40.

152. Ramus SJ, Eichenbaum H. Neural correlates of olfactory recognition memory in the rat orbitofrontal cortex. J Neurosci Off J Soc Neurosci. 2000 Nov;20(21):8199–208.

153. FitzGerald B, Richardson K, Wesson D. Olfactory tubercle stimulation alters odor preference behavior and recruits forebrain reward and motivational centers. Front Behav Neurosci [Internet]. 2014;8. Available from: https://www.frontiersin.org/article/10.3389/fnbeh.2014.00081

154. Wesson DW, Wilson DA. Sniffing out the contributions of the olfactory tubercle to the sense of smell: hedonics, sensory integration, and more? Neurosci Biobehav Rev. 2011 Jan;35(3):655–68.

155. Ikemoto S. Dopamine reward circuitry: two projection systems from the ventral midbrain to the nucleus accumbens-olfactory tubercle complex. Brain Res Rev. 2007 Nov;56(1):27–78.

156. Otazu GH, Chae H, Davis MB, Albeanu DF. Cortical Feedback Decorrelates Olfactory Bulb Output in Awake Mice. Neuron. 2015 Jun;86(6):1461–77.

157. Matsutani S. Trajectory and terminal distribution of single centrifugal axons from olfactory cortical areas in the rat olfactory bulb. Neuroscience. 2010 Aug;169(1):436–48.

158. Woolsey TA, Van der Loos H. The structural organization of layer IV in the somatosensory region (S I) of mouse cerebral cortex. The description of a cortical field composed of discrete cytoarchitectonic units. Brain Res. 1970;17(2):205–42.

159. Voges D, Carl K, Klauer GJ, Uhlig R, Schilling C, Behn C, et al. Structural

characterization of the whisker system of the rat. IEEE Sens J. 2012;12(2):332–9.

160. Dörfl J. The musculature of the mystacial vibrissae of the white mouse. J Anat [Internet]. 1982;135(Pt 1):147–54. Available from: http://www.ncbi.nlm.nih.gov/pubmed/7130049%0Ahttp://www.pubmedcentral.nih.gov/articlerender.fcgi?artid=PMC1168137

161. Wineski LE. Facial morphology and vibrissal movement in the golden hamster. J Morphol [Internet]. 1985 Feb 1;183(2):199–217. Available from: https://doi.org/10.1002/jmor.1051830208

162. Brecht M, Preilowski B, Merzenich MM. Functional architecture of the mystacial vibrissae. Behav Brain Res. 1997 Mar;84(1–2):81–97.

163. Vincent SB. The tactile hair of the white rat. J Comp Neurol [Internet]. 1913 Feb 1;23(1):1–34. Available from: https://doi.org/10.1002/cne.900230101

164. Maravall M, Diamond ME. Algorithms of whisker-mediated touch perception. Curr Opin Neurobiol [Internet]. 2014;25:176–86. Available from: https://www.sciencedirect.com/science/article/pii/S0959438814000294

165. Ebara S, Kumamoto K, Matsuura T, Mazurkiewicz JE, Rice FL. Similarities and Differences in the Innervation of Mystacial Vibrissal Follicle – Sinus Complexes in the Rat and Cat : A Confocal Microscopic Study. J Comp Neurol. 2002;119(April):103–19.

166. Rice FL, Mance A, Munger BL. A Comparative Light Microscopic Analysis of the Sensory Innervation of the Mystacial Pad . I . Innervation of Vibrissal Follicle- Sinus Complexes. J Comp Neurol. 1986;174(252):154–74.

167. Maravall M, Diamond ME. ScienceDirect Algorithms of whisker-mediated touch perception. Curr Opin Neurobiol [Internet]. 2014;25:176–86. Available from: http://dx.doi.org/10.1016/j.conb.2014.01.014

168. Zuo Y, Perkon I, Diamond ME. Whisking and whisker kinematics during a texture classification task. Philos Trans R Soc L B Biol Sci [Internet]. 2011;366(1581):3058–69. Available from: http://dx.doi.org/10.1098/rstb.2011.0161

169. Yu YSW, Graff MM, Hartmann MJZ. Mechanical responses of rat vibrissae to airflow. J Exp Biol. 2016;219(7):937–48.

170. Ma PM, Woolsey TA. Cytoarchitectonic correlates of the vibrissae in the medullary trigeminal complex of the mouse. Brain Res. 1984 Jul;306(1–2):374–9.

171. W.B C, Bowsher D. Terminal Distribution of Primary Afferent Fibers in the Rat Trigeminal. Exp Neurol. 1962;(6):372–83.

172. Dorfl J. The innervation of the mystacial region of the white mouse. A topographical study. J Anat. 1985;173–84.

173. Gibson JM, Welker WI. Quantitative studies of stimulus coding in first-order vibrissa afferents of rats. 1. Receptive field properties and threshold distributions. Somatosens Res. 1983;1(1):51–67.

174. Gibson JM, Welker WI. Quantitative studies of stimulus coding in first-order vibrissa afferents of rats. 2. Adaptation and coding of stimulus parameters. Somatosens Res. 1983;1(2):95–117.

175. Lichtenstein SH, Carvell GE, Simons DJ. Responses of rat trigeminal ganglion neurons to movements of vibrissae in different directions. Somatosens Mot Res. 1990;7(1):47–65.

176. Zucker E, Welker WI. Coding of somatic sensory input by vibrissae neurons in the rat's trigeminal ganglion. Brain Res. 1969 Jan;12(1):138–56.

177. Jacquin MF, Rhoades RW. Cell structure and response properties in the trigeminal subnucleus oralis. Somatosens Mot Res. 1990;7(3):265–88.

178. Jacquin MF, Renehan WE, Rhoades RW, Panneton WM. Morphology and topography of identified primary afferents in trigeminal subnuclei principalis and oralis. J Neurophysiol. 1993 Nov;70(5):1911–36.

179. Ma PM. The barrelettes--architectonic vibrissal representations in the brainstem trigeminal complex of the mouse. I. Normal structural organization. J Comp Neurol. 1991 Jul;309(2):161–99.

180. Durham D, Woolsey TA. Effects of neonatal whisker lesions on mouse central trigeminal pathways. J Comp Neurol. 1984 Mar;223(3):424–47.

181. Jacquin MF, Mooney RD, Rhoades RW. Morphology, response properties, and collateral projections of trigeminothalamic neurons in brainstem subnucleus

interpolaris of rat. Exp Brain Res [Internet]. 1986;61(3):457–68. Available from: https://doi.org/10.1007/BF00237571

182. Furuta T, Timofeeva E, Nakamura K, Okamoto-Furuta K, Togo M, Kaneko T, et al. Inhibitory Gating of Vibrissal Inputs in the Brainstem. J Neurosci [Internet]. 2008;28(8):1789–97. Available from: https://www.jneurosci.org/content/28/8/1789

183. Nguyen Q-T, Kleinfeld D. Positive feedback in a brainstem tactile sensorimotor loop. Neuron. 2005 Feb;45(3):447–57.

184. Diamond ME. Somatosensory Thalamus of the Rat BT - The Barrel Cortex of Rodents. In: Jones EG, Diamond IT, editors. Boston, MA: Springer US; 1995. p. 189–219. Available from: https://doi.org/10.1007/978-1-4757-9616-2_4

185. Williams MN, Zahm DS, Jacquin MF. Differential foci and synaptic organization of the principal and spinal trigeminal projections to the thalamus in the rat. Eur J Neurosci. 1994 Mar;6(3):429–53.

186. Veinante P, Deschênes M. Single- and multi-whisker channels in the ascending projections from the principal trigeminal nucleus in the rat. J Neurosci Off J Soc Neurosci. 1999 Jun;19(12):5085–95.

187. Van Der Loos H. Barreloids in mouse somatosensory thalamus. Neurosci Lett. 1976 Mar;2(1):1–6.

188. Haidarliu S, Ahissar E. Size gradients of barreloids in the rat thalamus. J Comp Neurol [Internet]. 2001 Jan 15;429(3):372–87. Available from: https://doi.org/10.1002/1096-9861(20010115)429:3%3C372::AID-CNE2%3E3.0.CO

189. Killackey HP, Sherman SM. Corticothalamic projections from the rat primary somatosensory cortex. J Neurosci [Internet]. 2003 Aug 13;23(19):7381–4. Available from: https://pubmed.ncbi.nlm.nih.gov/12917373

190. Meyer HS, Wimmer VC, Hemberger M, Bruno RM, de Kock CPJ, Frick A, et al. Cell type-specific thalamic innervation in a column of rat vibrissal cortex. Cereb Cortex [Internet]. 2010/06/09. 2010 Oct;20(10):2287–303. Available from: https://pubmed.ncbi.nlm.nih.gov/20534783

191. Killackey HP. The somatosensory cortex of the rodent. Trends Neurosci [Internet]. 1983;6:425–9. Available from:

https://www.sciencedirect.com/science/article/pii/0166223683901935

192. Chmielowska J, Carvell GE, Simons DJ. Spatial organization of thalamocortical and corticothalamic projection systems in the rat SmI barrel cortex. J Comp Neurol. 1989 Jul;285(3):325–38.

193. Diamond ME, Armstrong-James M, Ebner FF. Somatic sensory responses in the rostral sector of the posterior group (POm) and in the ventral posterior medial nucleus (VPM) of the rat thalamus. J Comp Neurol. 1992 Apr;318(4):462–76.

194. Pinault D. The thalamic reticular nucleus: structure, function and concept. Brain Res Brain Res Rev. 2004 Aug;46(1):1–31.

195. Pinault D, Bourassa J, Deschênes M. The axonal arborization of single thalamic reticular neurons in the somatosensory thalamus of the rat. Eur J Neurosci. 1995 Jan;7(1):31–40.

196. Woolsey TA, Van der Loos H. The structural organization of layer IV in the somatosensory region (SI) of mouse cerebral cortex. The description of a cortical field composed of discrete cytoarchitectonic units. Brain Res. 1970 Jan;17(2):205–42.

197. Ramaswamy S, Markram H. Anatomy and physiology of the thick-tufted layer 5 pyramidal neuron. Front Cell Neurosci [Internet]. 2015;9. Available from: https://www.frontiersin.org/article/10.3389/fncel.2015.00233

198. Petersen RS, Diamond ME. Spatial-temporal distribution of whisker-evoked activity in rat somatosensory cortex and the coding of stimulus location. J Neurosci Off J Soc Neurosci. 2000 Aug;20(16):6135–43.

199. Pinto DJ, Brumberg JC, Simons DJ. Circuit dynamics and coding strategies in rodent somatosensory cortex. J Neurophysiol. 2000 Mar;83(3):1158–66.

200. Pierret T, Lavallée P, Deschênes M. Parallel streams for the relay of vibrissal information through thalamic barreloids. J Neurosci Off J Soc Neurosci. 2000 Oct;20(19):7455–62.

201. Diamond ME, Arabzadeh E. Progress in Neurobiology Whisker sensory system – From receptor to decision. Prog Neurobiol [Internet]. 2013;103:28–40. Available from: http://dx.doi.org/10.1016/j.pneurobio.2012.05.013

202. Moore JD, Deschênes M, Furuta T, Huber D, Smear MC, Demers M, et al. Hierarchy of orofacial rhythms revealed through whisking and breathing. Nature [Internet]. 2013;497(7448):205–10. Available from: http://dx.doi.org/10.1038/nature12076

203. Arabzadeh E, Zorzin E, Diamond ME. Neuronal Encoding of Texture in the Whisker Sensory Pathway. Plos Biol. 2005;3(1):155–65.

204. von Heimendahl M, Itskov PM, Arabzadeh E, Diamond ME. Neuronal Activity in Rat Barrel Cortex Underlying Texture Discrimination. PLOS Biol [Internet]. 2007 Nov 13;5(11):e305. Available from: https://doi.org/10.1371/journal.pbio.0050305

205. Wu HPP, Ioffe JC, Iverson MM, Boon JM, Dyck RH. Novel, whisker-dependent texture discrimination task for mice. Behav Brain Res [Internet]. 2013;237(1):238–42. Available from: http://dx.doi.org/10.1016/j.bbr.2012.09.044

206. Adibi M, Arabzadeh E. A Comparison of Neuronal and Behavioral Detection and Discrimination Performances in Rat Whisker System. J Neurophysiol [Internet]. 2010 Nov 10;105(1):356–65. Available from: https://doi.org/10.1152/jn.00794.2010

207. Bodyak N, Slotnick B. Performance of mice in an automated olfactometer: odor detection, discrimination and odor memory. Chem Senses. 1999 Dec;24(6):637–45.

208. Abraham NM, Spors H, Carleton A, Margrie TW, Kuner T, Schaefer AT. Maintaining accuracy at the expense of speed: Stimulus similarity defines odor discrimination time in mice. Neuron. 2004;44(5):865–76.

209. Bhattacharjee AS, Konakamchi S, Turaev D, Vincis R, Nunes D, Dingankar AA, et al. Similarity and Strength of Glomerular Odor Representations Define a Neural Metric of Sniff-Invariant Discrimination Time. Cell Rep. 2019;28(11):2966-2978.e5.

210. Abraham NM, Guerin D, Bhaukaurally K, Carleton A. Similar Odor Discrimination Behavior in Head-Restrained and Freely Moving Mice. PLoS One. 2012;7(12):1–9.

211. Adrian ED. Olfactory reactions in the brain of the hedgehog. J Physiol. 1942;100(4):459–73.

212. Philpot BD, Foster TC, Brunjes PC. Mitral/tufted cell activity is attenuated and becomes uncoupled from respiration following naris closure. J Neurobiol. 1997;33(4):374–86.

213. MACRIDES F, CHOROVER SL. Olfactory Bulb Units. Science (80-). 1971;(August).

214. Fontanini A, Spano PF, Bower JM. Ketamine-xylazine-induced slow (<1.5 Hz) oscillations in the rat piriform (olfactory) cortex are functionally correlated with respiration. J Neurosci. 2003;23(22):7993–8001.

215. Onoda N, Mori K. Depth distribution of temporal firing patterns in olfactory bulb related to air-intake cycles. J Neurophysiol. 1980;44(1):29–39.

216. Grosmaitre X, Santarelli LC, Tan J, Luo M, Ma M. Dual functions of mammalian olfactory sensory neurons as odor detectors and mechanical sensors. Nat Neurosci [Internet]. 2007;10(3):348–54. Available from: http://www.pubmedcentral.nih.gov/articlerender.fcgi?artid=2227320&tool=pmcentrez&rendertype=abstract

217. Connelly T, Yu Y, Grosmaitre X, Wang J, Santarelli LC, Savigner A, et al. G protein-coupled odorant receptors underlie mechanosensitivity in mammalian olfactory sensory neurons. 2014;1–6.

218. Jadhav SP, Feldman DE. Texture coding in the whisker system. Curr Opin Neurobiol. 2010;20(3):313–8.

219. Deschênes M, Moore J, Kleinfeld D. Sniffing and whisking in rodents. Curr Opin Neurobiol. 2012;22(2):243–50.

220. Kepecs A, Uchida N, Mainen ZF. Rapid and precise control of sniffing during olfactory discrimination in rats. J Neurophysiol. 2007;98(1):205–13.

221. Glover P, Slotnick B. Does intranasal application of zinc sulfate produce anosmia in the rat ? Behav Neurosci. 2000;(September).

222. Alberts JR, Galef BG. Acute anosmia in the rat: A behavioral test of a peripherally-induced olfactory deficit. Physiol Behav. 1971;6(5):619–21.

223. Grosmaitre X, Santarelli LC, Tan J, Luo M, Ma M. Dual functions of mammalian olfactory sensory neurons as odor detectors and mechanical sensors.

224. McBride RL. A JND-scale/category-scale convergence in taste. Percept Psychophys [Internet]. 1983;34(1):77–83. Available from: https://doi.org/10.3758/BF03205899

225. Gamble EAM. The Applicability of Weber's Law to Smell... Cornell university.; 1898.

226. Schroder AC, Viemeister NF, Nelson DA. Intensity Discrimination In Normal-Hearing And Hearing-Impaired Listeners. J Acoust Soc Am. 1994;96(5):2683–93.

227. Shen J. On the foundations of vision modeling: I. Weber's law and Weberized TV restoration. Phys D Nonlinear Phenom [Internet]. 2003;175(3):241–51. Available from: https://www.sciencedirect.com/science/article/pii/S0167278902007340

228. Zanker JM. Does Motion Perception Follow Weber's Law? Perception [Internet]. 1995 Apr 1;24(4):363–72. Available from: https://doi.org/10.1068/p240363

229. Ekman Gös. Weber's Law and Related Functions. J Psychol [Internet]. 1959;47(2):343–52. Available from: https://doi.org/10.1080/00223980.1959.9916336

230. Bhattacharjee AS, Konakamchi S, Turaev D, Vincis R, Nunes D, Dingankar AA, et al. Similarity and Strength of Glomerular Odor Representations Define a Neural Metric of Sniff-Invariant Discrimination Time. Cell Rep. 2019;28(11):2966-2978.e5.

231. Slotnick B. Odor-Sampling Time of Mice under Different Conditions. Chem Senses [Internet]. 2007;32(5):445–54. Available from: https://doi.org/10.1093/chemse/bjm013

232. Linster C, Johnson BA, Morse A, Yue E, Leon M. Spontaneous versus reinforced olfactory discriminations. J Neurosci. 2002;22(16):6842–5.

233. Friedrich RW. Mechanisms of odor discrimination: neurophysiological and behavioral approaches. Trends Neurosci. 2006;29(1):40–7.

234. Wesson DW, Donahou TN, Johnson MO, Wachowiak M. Sniffing behavior of mice during performance in odor-guided tasks. Chem Senses. 2008 Sep;33(7):581–96.

235. Shusterman R, Sirotin YB, Smear MC, Ahmadian Y, Rinberg D. Sniff Invariant Odor Coding. eNeuro. 2018;5(6).

236. Díaz-Quesada M, Youngstrom IA, Tsuno Y, Hansen KR, Economo MN, Wachowiak M. Inhalation Frequency Controls Reformatting of Mitral/Tufted Cell Odor Representations in the Olfactory Bulb. J Neurosci Off J Soc Neurosci. 2018 Feb;38(9):2189–206.

237. Carey RM, Wachowiak M. Effect of sniffing on the temporal structure of mitral/tufted cell output from the olfactory bulb. J Neurosci Off J Soc Neurosci. 2011

Jul;31(29):10615–26.

238. Wu Z, Litwin-Kumar A, Shamash P, Taylor A, Axel R, Shadlen MN. Context-Dependent Decision Making in a Premotor Circuit. Neuron [Internet]. 2020;106(2):316-328.e6. Available from: https://doi.org/10.1016/j.neuron.2020.01.034

239. Berger T, Borgdorff A, Crochet S, Neubauer FB, Lefort S, Fauvet B, et al. Combined Voltage and Calcium Epifluorescence Imaging In Vitro and In Vivo Reveals Subthreshold and Suprathreshold Dynamics of Mouse Barrel Cortex. J Neurophysiol [Internet]. 2007;97(5):3751–62. Available from: http://jn.physiology.org/cgi/doi/10.1152/jn.01178.2006

240. Chen Q, Deister CA, Gao X, Guo B, Lynn-Jones T, Chen N, et al. Dysfunction of cortical GABAergic neurons leads to sensory hyper-reactivity in a Shank3 mouse model of ASD. Nat Neurosci. 2020;23(4):520–32.

241. Ronnett G V, Moon C. G proteins and olfactory signal transduction. Annu Rev Physiol. 2002;64(5):189–222.

242. Shipley MT, Ennis M. Functional organization of olfactory system. J Neurobiol. 1996;30(1):123–76.

243. Murphy GJ, Darcy DP, Isaacson JS. Intraglomerular inhibition: signaling mechanisms of an olfactory microcircuit. Nat Neurosci. 2005 Mar;8(3):354–64.

244. Hayar A, Karnup S, Ennis M, Shipley MT. External tufted cells: a major excitatory element that coordinates glomerular activity. J Neurosci Off J Soc Neurosci. 2004 Jul;24(30):6676–85.

245. De Saint Jan D, Hirnet D, Westbrook GL, Charpak S. External tufted cells drive the output of olfactory bulb glomeruli. J Neurosci Off J Soc Neurosci. 2009 Feb;29(7):2043–52.

246. Aungst JL, Heyward PM, Puche AC, Karnup S V, Hayar A, Szabo G, et al. Centre-surround inhibition among olfactory bulb glomeruli. Nature. 2003 Dec;426(6967):623–9.

247. Liu S, Plachez C, Shao Z, Puche A, Shipley MT. Olfactory bulb short axon cell release of GABA and dopamine produces a temporally biphasic inhibition-excitation response in external tufted cells. J Neurosci Off J Soc Neurosci. 2013 Feb;33(7):2916–26.

248. Egger V, Svoboda K, Mainen ZF. Dendrodendritic synaptic signals in olfactory bulb granule cells: local spine boost and global low-threshold spike. J Neurosci Off J Soc Neurosci. 2005 Apr;25(14):3521–30.

249. Chen WR, Xiong W, Shepherd GM. Analysis of relations between NMDA receptors and GABA release at olfactory bulb reciprocal synapses. Neuron. 2000 Mar;25(3):625–33.

250. Halabisky B, Friedman D, Radojicic M, Strowbridge BW. Calcium Influx through NMDA Receptors Directly Evokes GABA Release in Olfactory Bulb Granule Cells. J Neurosci [Internet]. 2000;20(13):5124–34. Available from: http://www.jneurosci.org/content/20/13/5124.abstract

251. Isaacson JS, Strowbridge BW. Olfactory reciprocal synapses: Dendritic signaling in the CNS. Neuron. 1998;20:749–61.

252. Mori K, Nagao H, Yoshihara Y. The olfactory bulb: coding and processing of odor molecule information. Science. 1999 Oct;286(5440):711–5.

253. Leon M, Johnson BA. Olfactory coding in the mammalian olfactory bulb. Brain Res Brain Res Rev. 2003 Apr;42(1):23–32.

254. Abraham NM, Egger V, Shimshek DR, Renden R, Fukunaga I, Sprengel R, et al. Synaptic Inhibition in the Olfactory Bulb Accelerates Odor Discrimination in Mice. Neuron [Internet]. 2010;65(3):399–411. Available from: http://dx.doi.org/10.1016/j.neuron.2010.01.009

255. Kapoor V, Urban NN. Glomerulus-Specific, Long-Latency Activity in the Olfactory Bulb Granule Cell Network. J Neurosci. 2006;26(45):11709–19.

256. Giridhar S, Doiron B, Urban NN. Timescale-dependent shaping of correlation by olfactory bulb lateral inhibition. Proc Natl Acad Sci U S A. 2011;108(14):5843–8.

257. Gschwend O, Abraham NM, Lagier S, Begnaud F, Rodriguez I, Carleton A. Neuronal pattern separation in the olfactory bulb improves odor discrimination learning. Nat Neurosci. 2015;18(10):1474–1482.

258. Bhattacharjee AS, Konakamchi S, Turaev D, Vincis R, Nunes D, Dingankar AA, et al. Similarity and Strength of Glomerular Odor Representations Define a Neural Metric of Sniff-Invariant Discrimination Time. Cell Rep [Internet]. 2019;28(11):2966-2978.e5.

Available from: https://doi.org/10.1016/j.celrep.2019.08.015

259. Sheikh SN, Martin SB, Martin DL. Regional distribution and relative amounts of glutamate decarboxylase isoforms in rat and mouse brain. Neurochem Int [Internet]. 1999;35(1):73–80. Available from: https://www.sciencedirect.com/science/article/pii/S0197018699000637

260. Kato HK, Chu MW, Isaacson JS, Komiyama T. Dynamic sensory representations in the olfactory bulb: modulation by wakefulness and experience. Neuron. 2012 Dec;76(5):962–75.

261. Yamada Y, Bhaukaurally K, Madarász TJ, Pouget A, Rodriguez I, Carleton A. Context- and Output Layer-Dependent Long-Term Ensemble Plasticity in a Sensory Circuit. Neuron. 2017 Mar;93(5):1198-1212.e5.

262. Chow BY, Han X, Dobry AS, Qian X, Chuong AS, Li M, et al. High-performance genetically targetable optical neural silencing by light-driven proton pumps. Nature. 2010 Jan;463(7277):98–102.

263. Lin JY, Lin MZ, Steinbach P, Tsien RY. Characterization of engineered channelrhodopsin variants with improved properties and kinetics. Biophys J. 2009 Mar;96(5):1803–14.

264. Nagel G, Szellas T, Huhn W, Kateriya S, Adeishvili N, Berthold P, et al. Channelrhodopsin-2, a directly light-gated cation-selective membrane channel. Proc Natl Acad Sci U S A. 2003 Nov;100(24):13940–5.

265. Boyden ES, Zhang F, Bamberg E, Nagel G, Deisseroth K. Millisecond-timescale, genetically targeted optical control of neural activity. Nat Neurosci. 2005 Sep;8(9):1263–8.

266. Nunes D, Kuner T. Disinhibition of olfactory bulb granule cells accelerates odour discrimination in mice. Nat Commun [Internet]. 2015;6:8950. Available from: http://www.nature.com/doifinder/10.1038/ncomms9950

267. Siemann JK, Muller CL, Bamberger G, Allison JD, Veenstra-VanderWeele J, Wallace MT. A novel behavioral paradigm to assess multisensory processing in mice. Front Behav Neurosci [Internet]. 2015;8(January):456. Available from: http://journal.frontiersin.org/article/10.3389/fnbeh.2014.00456/abstract%5Cnpapers3://

publication/doi/10.3389/fnbeh.2014.00456

268. Raposo D, Kaufman MT, Churchland AK. A category-free neural population supports evolving demands during decision-making. Nat Neurosci [Internet]. 2014;17(12):1784–92. Available from: http://www.pubmedcentral.nih.gov/articlerender.fcgi?artid=4294797&tool=pmcentrez&rendertype=abstract

269. Raposo D, Sheppard JP, Schrater PR, Churchland AK. Multisensory decision-making in rats and humans. J Neurosci. 2012;32(11):3726–35.

270. Shi Z, Müller HJ. Multisensory perception and action: Development, decision-making, and neural mechanisms. Front Integr Neurosci. 2013;7(NOV):7–9.

271. Kulahci IG, Dornhaus A, Papaj DR. Multimodal signals enhance decision making in foraging bumble-bees. Proc R Soc B Biol Sci. 2008;275(1636):797–802.

272. Ghosh DD, Nitabach MN, Zhang Y, Harris G. Multisensory integration in C. elegans. Curr Opin Neurobiol [Internet]. 2017;43:110–8. Available from: http://dx.doi.org/10.1016/j.conb.2017.01.005

273. Foxe JJ, Wylie GR, Martinez A, Schroeder CE, Javitt DC, Guilfoyle D, et al. Auditory-somatosensory multisensory processing in auditory association cortex: An fMRI study. J Neurophysiol. 2002;88(1):540–3.

274. Wallace MT, Meredith MA, Stein BE. Converging influences from visual, auditory, and somatosensory cortices onto output neurons of the superior colliculus. J Neurophysiol. 1993;69(6):1797–809.

275. Teder-Sälejärvi W a, Di Russo F, McDonald JJ, Hillyard S a. Effects of spatial congruity on audio-visual multimodal integration. J Cogn Neurosci. 2005;17(9):1396–409.

276. Stein BE, Meredith MA. The merging of the senses. The MIT press; 1993.

277. Stein BE, London N, Wilkinson LK, Price DD. Enhancement of perceived visual intensity by auditory stimuli: a psychophysical analysis. J Cogn Neurosci. 1996;8(6):497–506.

278. Siemann JK, Muller CL, Bamberger G, Allison JD, Veenstra-VanderWeele J, Wallace

MT. A novel behavioral paradigm to assess multisensory processing in mice. Front Behav Neurosci. 2015;8(JAN):1–10.

279. Sakata S, Yamamori T, Sakurai Y. Behavioral studies of auditory-visual spatial recognition and integration in rats. Exp Brain Res. 2004;159(4):409–17.

280. Sekuler R, Sekuler AB, Lau R. Sound alters visual motion perception [6]. Vol. 385, Nature. 1997. p. 308.

281. Reig R, Silberberg G. Multisensory Integration in the Mouse Striatum. Neuron [Internet]. 2014;83(5):1200–12. Available from: http://dx.doi.org/10.1016/j.neuron.2014.07.033

282. Courtiol E, Amat C, Thévenet M, Messaoudi B, Garcia S, Buonviso N. Reshaping of bulbar odor response by nasal flow rate in the rat. PLoS One. 2011 Jan;6(1):e16445.

283. Manabe H, Mori K. Sniff rhythm-paced fast and slow gamma-oscillations in the olfactory bulb: relation to tufted and mitral cells and behavioral states. J Neurophysiol. 2013 Oct;110(7):1593–9.

284. Rojas-Líbano D, Frederick DE, Egaña JI, Kay LM. The olfactory bulb theta rhythm follows all frequencies of diaphragmatic respiration in the freely behaving rat. Front Behav Neurosci. 2014;8:214.

285. Gerkin RC, Tripathy SJ, Urban NN. Origins of correlated spiking in the mammalian olfactory bulb. Proc Natl Acad Sci U S A. 2013 Oct;110(42):17083–8.

286. Zelano C, Jiang H, Zhou G, Arora N, Schuele S, Rosenow J, et al. Nasal Respiration Entrains Human Limbic Oscillations and Modulates Cognitive Function. J Neurosci Off J Soc Neurosci. 2016 Dec;36(49):12448–67.

287. Heck DH, Kozma R, Kay LM. The rhythm of memory: how breathing shapes memory function. J Neurophysiol. 2019 Aug;122(2):563–71.

288. Kepecs A, Uchida N, Mainen ZF. The sniff as a unit of olfactory processing. Chem Senses. 2006;31(2):167–79.

289. Keyhani K, Scherer PW, Mozell MM. A numerical model of nasal odorant transport for the analysis of human olfaction. J Theor Biol. 1997;186(3):279–301.

290. Tong J, Mannea E, Aimé P, Pfluger PT, Yi C-X, Castaneda TR, et al. Ghrelin

enhances olfactory sensitivity and exploratory sniffing in rodents and humans. J Neurosci Off J Soc Neurosci. 2011 Apr;31(15):5841–6.

291. Bensafi M, Porter J, Pouliot S, Mainland J, Johnson B, Zelano C, et al. Olfactomotor activity during imagery mimics that during perception. Nat Neurosci. 2003 Nov;6(11):1142–4.

292. Laing DG. Natural sniffing gives optimum odour perception for humans. Perception. 1983;12(2):99–117.

293. Sobel N, Prabhakaran V, Hartley CA, Desmond JE, Zhao Z, Glover GH, et al. Odorant-induced and sniff-induced activation in the cerebellum of the human. J Neurosci Off J Soc Neurosci. 1998 Nov;18(21):8990–9001.

294. Vandersteen C, Payne M, Dumas L-É, Cancian É, Plonka A, D'Andréa G, et al. Olfactory Training in Post-COVID-19 Persistent Olfactory Disorders: Value Normalization for Threshold but Not Identification. J Clin Med. 2022 Jun;11(12).

295. Bhowmik R, Pardasani M, Mahajan S, Bhattacharjee AS, Konakamchi S, Phadnis S, et al. Uncertainty revealed by delayed responses during olfactory matching. bioRxiv [Internet]. 2022; Available from: https://www.biorxiv.org/content/early/2022/09/13/2022.09.11.507462

296. Sobel N, Thomason ME, Stappen I, Tanner CM, Tetrud JW, Bower JM, et al. An impairment in sniffing contributes to the olfactory impairment in Parkinson's disease. Proc Natl Acad Sci U S A. 2001 Mar;98(7):4154–9.

297. Ludwig S, Schell A, Berkemann M, Jungbauer F, Zaubitzer L, Huber L, et al. Post-COVID-19 Impairment of the Senses of Smell, Taste, Hearing, and Balance. Viruses. 2022 Apr;14(5).

298. Doty RL. Olfactory dysfunction in COVID-19: pathology and long-term implications for brain health. Trends Mol Med [Internet]. 2022;28(9):781–94. Available from: https://www.sciencedirect.com/science/article/pii/S1471491422001605

299. Hintschich CA, Fischer R, Hummel T, Wenzel JJ, Bohr C, Vielsmeier V. Persisting olfactory dysfunction in post-COVID-19 is associated with gustatory impairment: Results from chemosensitive testing eight months after the acute infection. PLoS One. 2022;17(3):e0265686.